ECO–FRIENDLY DYNAMIC POSITIONING ALGORITHM DEVELOPMENT

A Dissertation

by

SE WON KIM

Submitted to the Office of Graduate and Professional Studies of
Texas A&M University
in partial fulfillment of the requirements for the degree of

DOCTOR OF PHILOSOPHY

Chair of Committee,	Moo-Hyun Kim
Committee Members,	Jeffrey Falzarano
	Richard Mercier
	Achim Stössel
Head of Department,	Sharath Girimaji

December 2016

Major Subject: Ocean Engineering

ABSTRACT

This research used the penalty method to develop a dynamic positioning control algorithm object for the purpose of minimizing the fuel consumption and CO_2 gas emissions of an offshore platform. The performance of the penalty method was evaluated by comparing it with other conventional methods such as pseudo-inverse, quadratic programming, and genetic algorithm methods. The optimal performance of the penalty method in minimizing fuel consumption and CO_2 emissions in both Gulf of Mexico (GOM) 100-year and one-year storm conditions was compared to pseudo-inverse and quadratic-programming methods.

A feed-forward control using second-order wave force direct integration was newly applied in this research. The feed-forward control improved both the position maintenance performance and fuel consumption in Gulf of Mexico 100-year and one-year storm conditions.

Global motion performance was compared after placing turrets in two locations (mid-ship and bow) and by using a hull-mooring-riser, fully coupled simulation. The results indicated that the mid-turret design reduces heave motion, even though its horizontal motion is unstable. In addition, the dynamic positioning control enhanced the horizontal motion of the mid-ship turret design.

To reduce fish-tailing motion in a tandem offloading operation, the dynamic positioning control was employed. Separated Matrix Method based simulations were conducted on a fully coupled hull, mooring, riser, hawser, and thrusters.

DEDICATION

To my parents, Jhong-Hyun Kim and Hye-Ran Lim, and my son, Dong Min,

with Love

ACKNOWLEDGEMENTS

I would like to express special thanks to my advisor, Dr. Moo-Hyun Kim, for his encouragement and kind advice throughout my research. His teaching, daily life, expertise, and personality deserve great praise.

Special thanks are extended to Dr. Richard Mercier, Dr. Jeffrey Falzarano, and Dr. Achim Stössel for their excellent service as my dissertation committee advisors.

I also express my great appreciation to my company and colleagues who sponsored me over three years.

I would also like to thank Hakun Jang, Hyung-Chul Kim, Chung-kuk Jin, Theano Kampani, and Duoduo Ding'16 for their tremendous friendship and support.

Finally, I would like to express my]appreciation to my parents, Jong-Hyun Kim and Hye-Ran Lim; my sister, Hye-Won Kim; and my lovely son, Dong Min Kim; for their love and encouragement.

NOMENCLATURE

B	Breadth
CO_2	Carbon Dioxide
D	Depth
DP	Dynamic Positioning
e	Error Matrix
F	Fuel Consumption
J	Object Function for LQR (Linear Quadratic Regulator)
K	Gain Matrix
L	Length
M	Mass
P	Power
Q	Weight Matrix
$R(t-\tau)$	Retardation Function
T	Thrust of Thruster
t	Thruster Command Matrix
u	Input Matrix
x	State Matrix
$\hat{x}$	State Estimation Matrix
x_{target}	Target State Matrix
y	Measurement Matrix of Kalman Filter
α	Azimuth Angle of Thruster

TABLE OF CONTENTS

Page

LIST OF FIGURES

LIST OF TABLES

TABLE Page

CHAPTER I

INTRODUCTION

1.1 General

While fossil fuel has been a major energy resource worldwide beginning in the 20th century, its supply is limited. Furthermore, oil supply and demand are driven by global economic and geopolitical strategy, so fuel prices are highly volatile and fluctuate greatly. Accordingly, fuel consumption control is always a key issue across the industry. The same trend is true in the offshore sector because fuel consumption is the major driver of operating cost expenditures (OPEX).

A major, 10-year review found that the offshore oil market has expanded since 1960. There is significant price variability in oil when using a one-year scale, and this is expected to grow until 2020 under a 10-year scenario. Figure 1.1 shows the same trend for offshore oil production. This tendency suggests that offshore oil exploration will increase continuously across the 10-year period.

The offshore oil exploration boom that started in 1960 has accelerated most significantly in the area of the deep-water exploration (i.e., deeper than 4,000 feet). This deep-water exploration necessitated the development of position-keeping devices to counteract negative environmental forces. Position loss resulting from device failure could be disastrous. One representative example of such position failure is the Gryphon DP floating production storage offloading (FPSO) drift-off incident.

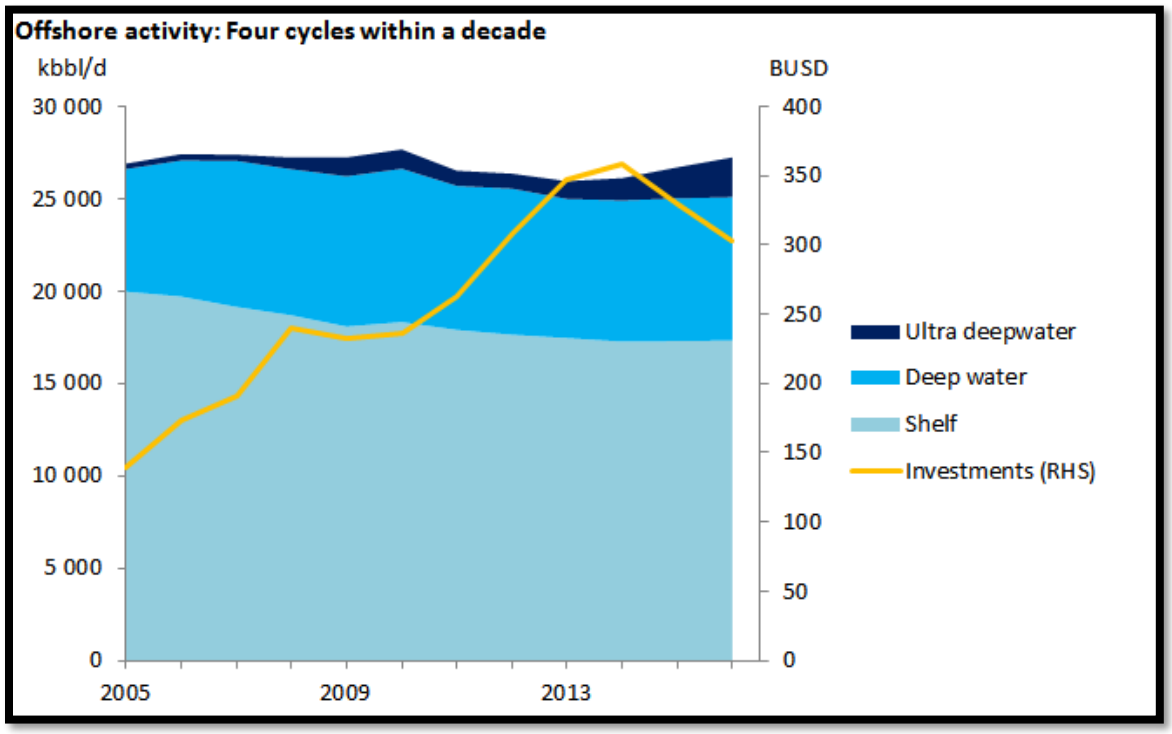

Figure 1.1 Offshore Oil Production

Table 1.1 Gryphon Alpha FPSO Principal Dimensions

Owner	Maersk
Location	Gryphon, UK
L,B,D (m)	260,41,23
Oil Production	60,000 B/day
Mooring	DP assisted turret mooring

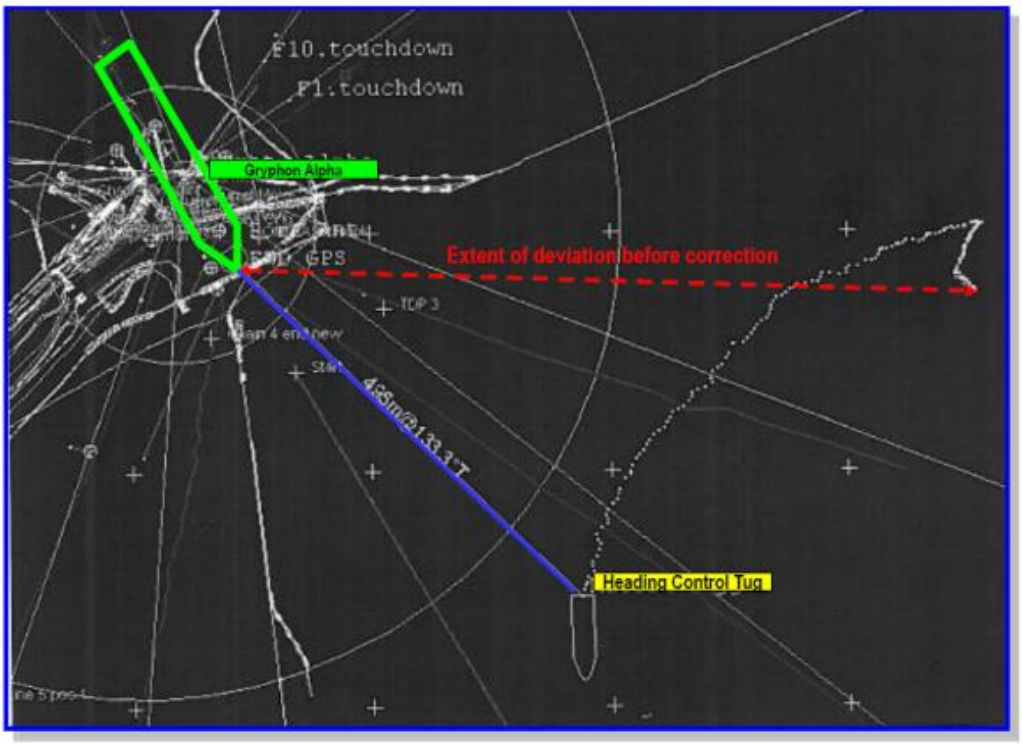

Figure 1.2 Gryphon Drift Incident

To summarize, the Gryphon drift-off incident began with heading angle control loss, which led to a 30-second blackout and FPSO drift-off for 10 minutes with a distance of 180m. This occurred under harsh environmental conditions, with wind speeds of 60knots and wave heights about 12m. The red dotted line in Figure 1.2 indicates the Gryphon's drift trajectory from the original position of the green outlined vessel, also shown in Figure 1.2. The results were catastrophic. Not only were four anchor-chains and subsea structures broken, but oil production was halted for 27 months, and restoration of the Gryphon DPS took two years. Losses to the ship owner, Maersk, totaled about $50 billion.

This incident underscores the importance of position-keeping devices and their performance analysis. Only the most precise and realistic position-keeping performance analysis could prevent future, serious disasters.

Mooring and dynamic positioning systems (DPSs) are representative positioning devices used by deep-water, offshore platforms below 4,000 feet. A mooring system can supply sufficient bearing force against environmental forces; on the other hand, the cost to install and remove moorings is much greater than for DPSs. Installation and removal operations are critical because the process may take several days following a hurricane or other storm. In contrast, dynamic positioning (DP) has relatively large, initial installment costs (including thrusters and big generators), but provides greater mobility under emergency conditions.

The DPS consists of controller, sensors, generator, operating station, and actuators, and can automatically control the position of an offshore platform through control actuators. Figure 1.3 shows the conventional structure of the DPS.

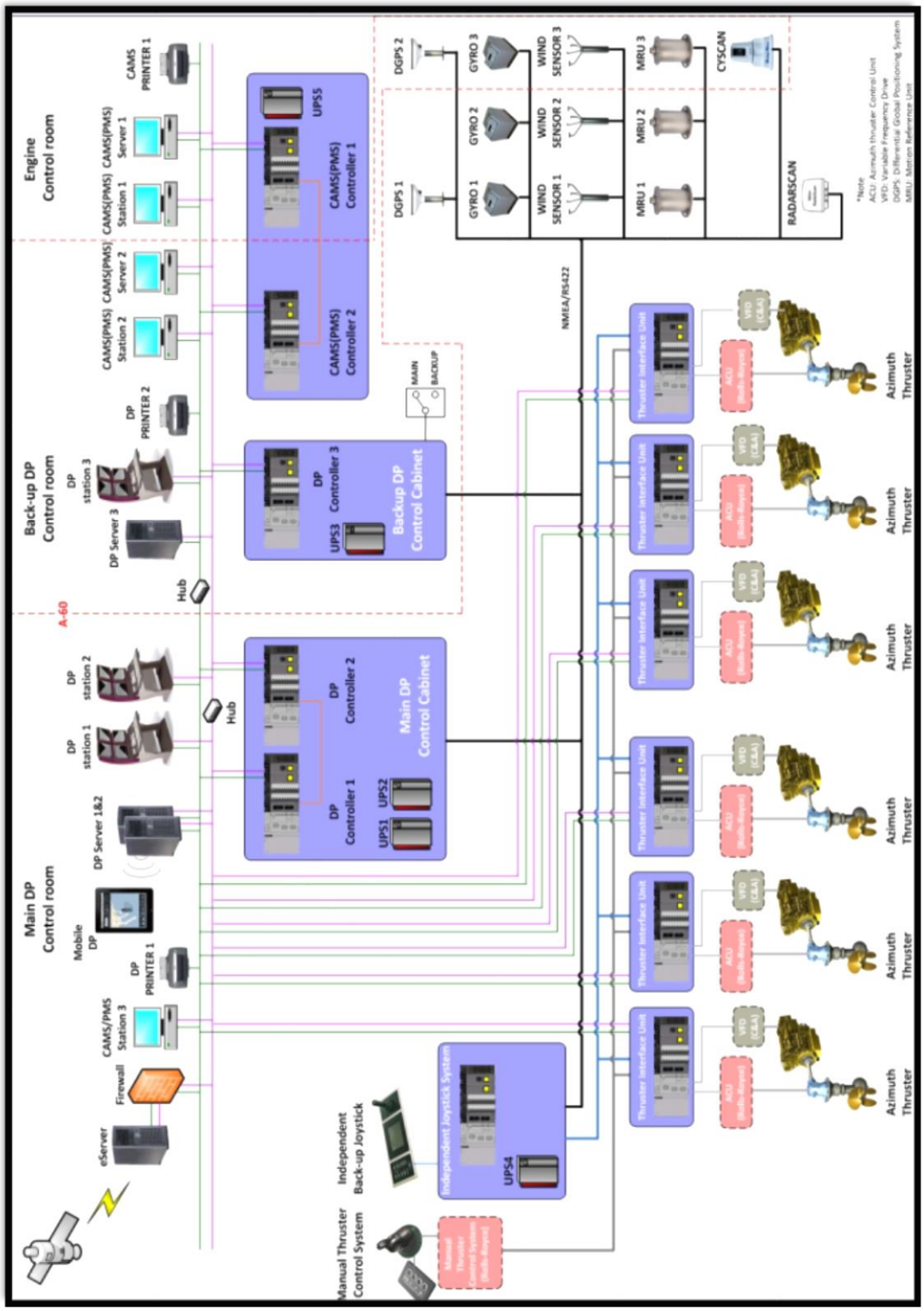

Figure 1.3 Conventional Structure of a Dynamic Positioning System

DP has been in use since 1960. Currently, DPS is installed across the vessels and oil platforms in the offshore oil value chain. Figure 1.4 shows the types of fields, vessels, and offshore platforms equipped with DPS.

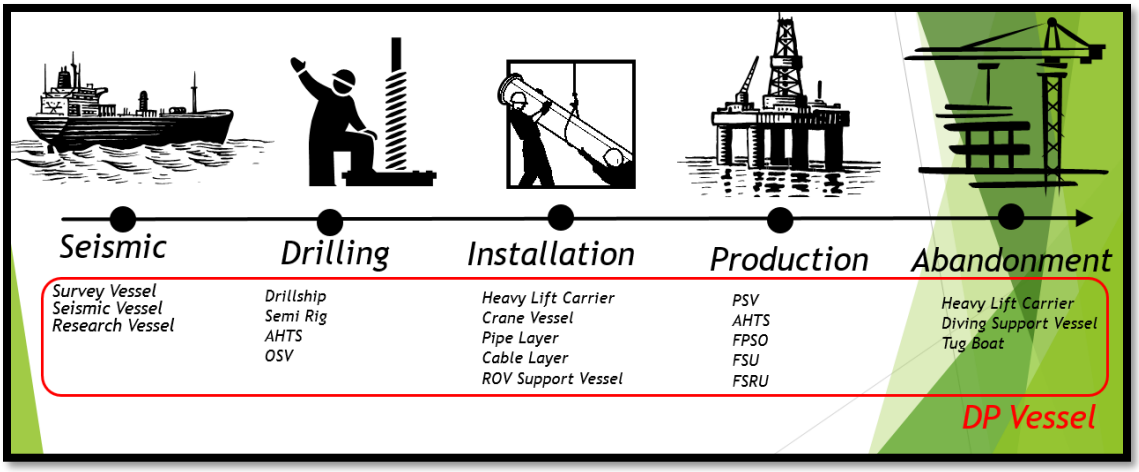

Figure 1.4 DPS Applications in the Oil Value Chain

The DPS sales market was U.S. $1.6 billion per year in 2015 and is expected to grow 5% annually, as noted in the Clarkson yearbook reference in Figure 1.5. These statistics indicate that the foreseeable demand for DPS is continuous and growing.

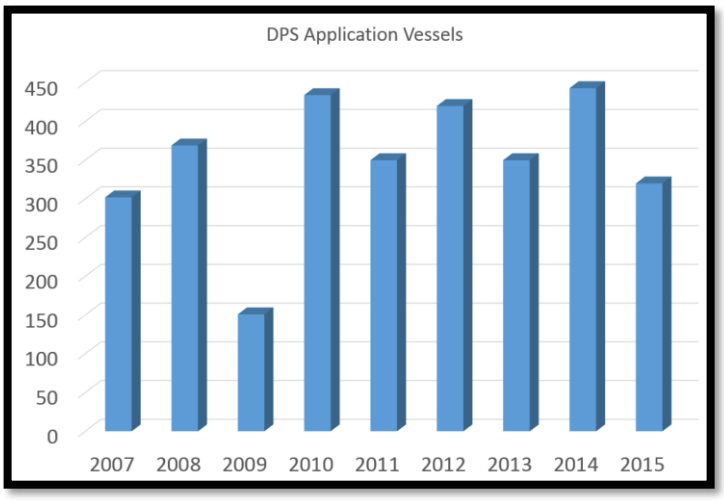

Figure 1.5 DP Application Vessels

The dynamic positioning system accounts for the highest portion of total expenditures in the offshore platform market because it is the heaviest fuel consumer and the second-most-expensive system in offshore platform capital expenditures (CAPEX) after fuel consumption (Table 1.2).

Table 1.2 Offshore Platform Total Expenditures

	CAPEX	OPEX without Fuel	Fuel Consumption
Total Expenditure	20%	18%	62%

The dynamic positioning system also is the heaviest fuel consumer among offshore platform equipment, as seen in Table 1.3 (C.-h. Kim, Kim, Jung, Ryu, & Yoon, 2012)

Table 1.3 Fuel Consumption of Major Equipment for Offshore Platforms

System	Fuel Consumption
Dynamic Positioning System	62%
Service System	26%
Drilling Unit	12%

Thus, if a researcher wants to make the offshore platform more fuel efficient, then reducing DPS fuel consumption would be an important goal. The DPS is the largest gas polluter among offshore platform equipment. According to the Jayaram (2010), DPS generates 48% of total gas emissions.

Table 1.4 Gas Emissions of Major Offshore Platform Systems

System	Gas Emissions
Dynamic Positioning System	48%
Service System	31%
Drilling Unit	21%

Furthermore, environmental regulations have become much more restrictive in recent years. Developed countries agreed to limit greenhouse gases, including carbon dioxide (CO_2), under the 1997 Kyoto Protocol, the international treaty that extended the 1992 United Nations Framework Convention on Climate Change. The International Maritime Organization (IMO) imposed a mandatory rule that forces the reduction of

greenhouse gas (GHG) under MARPOL Annex VI. In case of SOx, the limitation was 4.50% m/m in 2012, but this will be gradually increased to 0.50%m/m in 2020. (At the time of this research in 2016, it was 3.50% m/m.) Furthermore, the United Nations has increased taxes on carbon emissions. For example, Norway has a tax of $23/tonne CO_2. This trend is projected to continue, with further reinforcements in the future.

In this regard, DPS could significantly advance efficiencies in fuel consumption and gas emissions. Steven.N (2007) conducted a simple economic analysis, finding that the offshore platform DPS consumes $7.3 million in fuel per year and $146.5 million fuel during a platform's lifetime, and generates 800,000 tons of CO_2. If dynamic positioning systems can improve fuel consumption performance, then they could simultaneously also reduce gas emissions of offshore platforms, because fuel consumption, CO_2, and NO_x, have a proportional relationship (Jayarm, 2010). Thus, a 5% fuel consumption improvement under a dynamic positioning system could achieve a $9 million economic expectancy during the lifetime of an offshore platform. This expectation could increase over time as environmental regulations are tightened. Therefore, the goals of reducing fuel consumption and gas emissions are vitally important.

The DP control algorithm has three main units: an estimator, controller, and thruster allocation. The estimator predicts velocity, position, angle, and angular velocity of offshore platforms. The controller generates control forces and moments to maintain their position. The thrust allocation distributes the control forces to the actuators (see Figure 1.6).

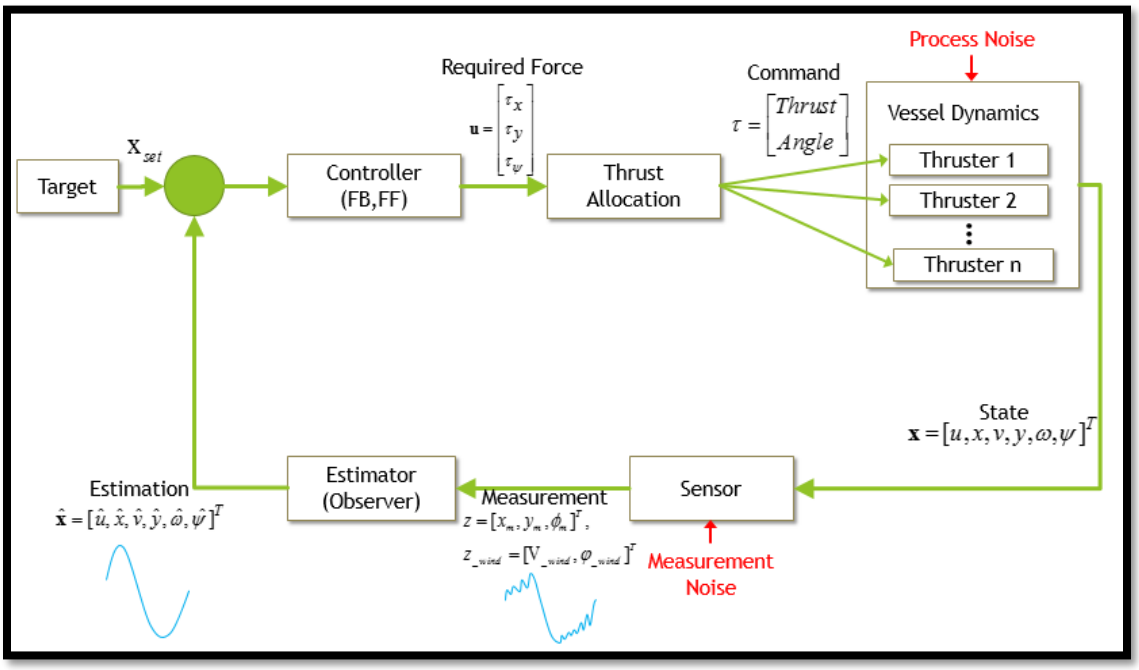

Figure 1.6 DP Control Algorithm Diagram

The offshore exploration boom created growth and research in dynamic positioning technology. There have been three primary areas of research on this technology since the 1960s: controllers, thrust allocation, and coupled analysis. Controller research started in the 1970s for the single-input and single-out (SISO) controller and simple observer. In 1980, advanced output control methods based on multi-input and multi-output (MIMO) optimal control, and Kalman filter theory, were proposed and extended by Jessen Balchen, Jenssen, Mathisen, and Sælid (1980). From the 1990s through the 2010s, nonlinear control had been proposed.

In the offshore industry, MIMO optimal control and the Kalman filter became a popular combination for the commercial DP control algorithm. As this technology matured, DP researchers have focused on improved performance (i.e., developing a larger

operational window and more robustness during unexpected disturbances) by vessel type and mission by including operational requirements.

Thrust allocation is another mainstay of DP control research. Thrust minimum objected thrust allocation studies have been conducted since 1960. Tor A Johansen and Fossen (2013) reviewed and summarized state-of-the-art thrust allocation, including linear and nonlinear, constrained and unconstrained, quadratic programming, and other optimization applications for the marine industry. Generally, dynamic positioning vessels have the indefinite problem of over-actuated control systems. Thus, thrust allocation can be addressed using optimization methods. The pseudo-inverse method, which aims to minimize total thrust square, has been widely used in the offshore industry (Tor A Johansen & Fossen, 2013). The pseudo-inverse method can find thruster commands by multiplying the pseudo-inverse of the thruster configuration and control forces matrix(Ryu, 2005) ,as seen in the following:

$$u = \mathrm{B}t$$

$$Cu = B^T (BB^T)^{-1} t \tag{1.1}$$

Where, *B* is a thruster configuration matrix, *C* is a pseudo-inverse matrix of configuration matrix and u is the required forces and moments; t is the thruster command matrix.

The pseudo-inverse approach has been a major solution in the industrial dynamic positioning field because the computation burden is light, making it suitable for the application of on-board computation. The pseudo-inverse method also has disadvantages, however. It cannot give elaborate thruster allocation values when the required force exceeds the thrusters' physical limitations, such as thruster capacity and rate constraints.

To solve the thrust allocation problem, alternative thrust allocation quadratic programming, which has a quadratic form object function and linear constraints, was proposed as the proper optimization strategy. Quadratic programming thrust allocation was modeled and applied to the dynamic positioning control algorithm (Tor Arne Johansen, Fossen, & Berge, 2004). De Wit (2009) compared the pseudo-inverse method and the quadratic programming method and found that the quadratic programming provided a more elaborate solution than the pseudo-inverse method when the thruster was saturated and failed. Rindarøy and Johansen (2013) used the quadratic programming method for the thrust allocation to minimize total thrust, power, and fuel consumption.

In Zhao and Roh (2015), the hybrid optimization method that combines the genetic algorithm and sequential quadratic programming was adopted to solve the thrust allocation problem for the semi-submersible drilling rig. This research modeled the interaction between thrusters, because thrusters are close enough to interrupt their mutual flow pattern in semi-rig DP control. The suggested thrust allocation method achieved 2% power reduction compared to the pseudo-inverse method. Genetic algorithm offers the advantage of finding a global optimum against local optimization methods (the quadratic programming and the pseudo-inverse methods). In addition, it does not have the limitations of formulation constraints and object functions. However, the computational burden of genetic algorithms is heavy because the algorithm generates random parent groups and creates mutations for making a large number of optimization candidates. Considering these drawbacks, an alternative optimization scheme can be the penalty method, which can deal with any type of constraints and objection functions that optimization problems might have.

Meanwhile, the computational amount of the penalty method is smaller. Until this dissertation, no research to date has attempted the use of the penalty method for designing fuel-optimal thrust allocation.

Ryu (2005) was the first to develop fully coupled dynamics among the hull, mooring, riser, and dynamic positioning system for FPSO. That research was quite challenging, because the calculation was complex and time consuming – complications that that remains today. Ryu found that the application of thrusters made a 10% watch circle reduction compared to DP FPSO without the dynamic positioning system under GOM 100-year storm conditions. However, this research did not include heading control and thrust allocation. A simulation of fully coupled dynamics among hull, mooring, riser, and DPS with fuel and gas optimal thrust allocation time domain has not yet been conducted. This is a niche topic of DP research that will be filled in the present research.

Rindarøy and Johansen (2013) evaluated the increase of fuel consumption resulting from thrust allocation methods that object to minimize fuel consumption, power minimization, and load fluctuation. The fuel consumption optimization quadratic programming thrust allocation method showed the best performance in the reduction of fuel consumption. This method achieved 2% fuel reduction compare to the thrust-minimized quadratic optimization method. However, that research did not analyze the time-accumulation effect caused by the combination of the dynamic positioning, on-time controller and thrust allocation in the real-time domain. This effect can be crucial when applying a thrust allocation algorithm to the real-time industrial DP controller, because the thrust allocation optimization should be calculated and delivered to the DP under control

in the calculation limitation. If the thrust allocation takes longer than one simulation period, then an optimization solution is not feasible due to the time lag for the control, which degrades DP performance.

1.2 Objectives

This dissertation seeks to propose a new dynamic positioning control algorithm that could reduce both fuel consumption and gas emissions simultaneously. The proposed control algorithm will be compared to the conventional pseudo-inverse method, the quadratic method, and the genetic algorithm in the position-keeping performance, fuel consumption reduction performance, and gas emissions reduction effect. This work will apply the penalty-method-based optimization solving scheme to the problem of fuel optimal DP thrust allocation. It also will formulate and solve the mathematical problem of the fuel consumption and gas emissions optimal thrust allocation algorithm that fits in the optimization frame. Additionally, this research will determine the optimization strategy that is the most feasible and superior in terms of performance. This research also will implement the developed thrust allocation module into the real-time dynamic positioning control frame, and will conduct the 6DOF, fully coupled dynamics among hull, mooring, riser, and fuel optimal dynamic positioning control for FPSO. For precise control, the feed-forward control will be modeled and simulated in this work. The direct integration method for wave second order load feed-forward will be implemented in the simulation. Furthermore, the developed DP algorithm will be applied to the mid-ship turret design, and its global motion response will be compared to the bow turret design. Finally, the

developed work will be applied to a tandem, offloading case by using SMM (Separated Matrix Method).

1.3 Research Procedure Summary

The development of an eco-friendly DP control algorithm will be achieved using the following research procedure:

a. Optimization variable design
b. Mathematical modeling
c. Validation by static simulation
d. Performance evaluation according to optimization strategies by time domain simulation
    - Environmental conditions effect
    - Thruster configuration effect
e. Feed-forward control
f. Turret location effect analysis
g. Multi-body time domain simulation

During the first step, optimization parameters will be set for use as variables for object function and constraint for the thrust allocation problem. Fuel consumption, gas emissions, and thruster physical characteristics will be interpreted mathematically. Parameters will be set up based on the literature review. Parameter modeling is important because optimization variables will be used as elements of mathematical formulation and

performance evaluation. In other words, if parameter modeling is sufficiently precise, then the solution to the problem could be credible.

A mathematical procedure for finding a mathematical solution to controller and thrust allocation will be performed in the second stage. The theoretical background of controller and optimization methodology of thrust allocation will be reviewed, and the procedure that finds a mathematical solution for controller and thruster allocation will be derived. The problem of fuel consumption and gas emissions optimal controller and thrust allocation will be mathematically solved, and the solution will be implemented in the DP time domain simulation code. The DP time domain simulation code calculates the coupled simulation with the motion analysis program CHARM 3D. The developed DP code then will be validated by Rindarøy and Johansen (2013). The pseudo-inverse method, quadratic programming, penalty method, and genetic algorithm will be tested to determine the best candidate for thrust allocation in fuel optimization in Chapter II.

To enhance the performance of DP control, the feed-forward control will be implemented in the DP controller. The key factor for the performance of feed-forward control is precise environmental loads modeling. The direct integration method for the wave load estimation will be modeled and implemented. For the performance evaluation, the hull-mooring-riser fully coupled time domain simulation will be performed using CHARM 3D described in Chapter III.

A time domain simulation will be conducted to investigate the global motion performance change due to the turret location in the bow and mid-ship. The feasibility of the DP application will be examined in Chapter IV.

Finally, the DP will be implemented in the multi-body simulation. The tandem operation configuration of the moored FPSO and the DP shuttle tanker will be simulated. The fish-tailing motion of the shuttle tanker is the main factor contributing to collisions during the tandem off-loading operation. In this study, the position-keeping performance improvement will be simulated under West African and GOM one-year storm conditions, as detailed in Chapter V.

Up to now, research procedure was briefly summarized. Then detail approach of each research step and results will be presented in each chapters.

CHAPTER II

ECO-FRIENDLY DYNAMIC POSITIONING SYSTEM

2.1 Introduction

Dynamic positioning system (DPS) is the system that automatically maintains the position of an offshore platform by controlling actuators as the platform encounters environmental forces. Currently, dynamic positioning systems are installed on many vessels used in offshore drilling, production, and exploration to directly manage operational safety by preventing unintended drift. Dynamic positioning systems involve important units such as sensors, power management systems, generators, and control actuators. The dynamic positioning systems are usually the heaviest fuel consumer and second-most-expensive system in offshore platform capital expenditures (Kim, 2012). Fuel consumption accounts for 62% of the total expenditures of offshore platforms (DnB Nor, 2012). Dynamic positioning systems consume the largest amount of fuel. Moreover, they produce more gas pollution (48%) among the various offshore operations (Jayaram, 2010).Therefore, to reduce both fuel consumption and gas emissions by offshore platforms, the development of efficient DP systems is essential.

In general, fuel consumption and gas emissions are proportional (Jayaram, 2010). Even a 5% fuel consumption improvement in a dynamic positioning system could save about $9 million over 20 years, even considering the cost of handling carbon dioxide, and these savings are expected to increase as governments around the world tighten environmental regulations.

Thrust allocation research, which seeks to minimize total thrust, has been conducted actively since 1960 (Tor A Johansen & Fossen, 2013). Tor A Johansen and Fossen (2013) reviewed and summarized the state of the art of marine industry thrust allocation: linear and nonlinear, constrained and unconstrained, quadratic programming and other optimization applications. Johansen found that generally, dynamic positioning vessels have over-actuated control systems that have more actuators than the number of degrees of freedom. Therefore, thrust allocation issues could be solved using optimization methods. The pseudo-inverse method has been widely used in the industrial field. The pseudo-inverse method can find allocated thruster commands by multiplying the pseudo-inverse of thruster configuration and control forces. The pseudo-inverse has been widely used in the industrial dynamic positioning field because its computation is simple, making it suitable for onboard computation that should be controlled within about limited control time step. This method, however, does have disadvantages. For example, it cannot give elaborate thruster allocation values when the required force exceeds the thrusters' physical limitations, such as capacity and rate constraint.

To deal with this drawback, quadratic programming was proposed as an alternative optimization strategy for total-thrust-power minimization. Quadratic programming is the suitable optimization strategy when it has a thruster quadratic form object function and linear thruster constraints. Industrial quadratic programing for dynamic positioning system was modeled in Tor Arne Johansen et al. (2004). De Wit (2009) compared the pseudo-inverse method and quadratic programming method and found that the quadratic programming gave more elaborate solutions than the pseudo-inverse method under

thruster saturation and failure conditions. Rindarøy and Johansen (2013), using quadratic programming, modeled and solved thrust allocation problems to minimize fuel consumption and power load.

Zhao and Roh (2015) employed the hybrid method that combines the genetic algorithm with sequential quadratic programming to solve the thrust allocation problem for a semi-submersible drilling rig. The suggested thrust allocation method achieved 2% power reduction compared to the pseudo-inverse method. In the present study, an alternative optimization scheme, called the penalty method, is introduced because it can deal with any type of constraints and objection functions.

The fully coupled dynamic simulation among hull, mooring, riser, and DP system in the time domain is another unique feature of the present study. Using the developed fully coupled time-domain simulation program, the accumulated fuel consumption and CO_2 emissions for any offshore platforms for the given environment and duration could be obtained. This can be crucial when applying a thrust allocation algorithm to a real-time industrial DP controller. If thrust allocation takes longer than the simulation unit time period (about one second) considering the DP controller control period, an optimization solution is not feasible due to time lag for the control.

This research formulated the mathematical modeling of a fuel optimal, thrust allocation algorithm that fits within the penalty method optimization frame. This research also implements the developed thrust allocation module into a dynamic positioning control frame. In addition, the developed algorithm was applied to a turret-moored FPSO with

real-storm conditions to assess its efficiency compared to other existing thruster-allocation methods. To draw more general conclusions, several different scenarios were considered.

2.2 Mathematical Model

A conventional DP control algorithm consists of three modules: estimation, control, and thrust allocation. Generally, a Kalman filter or an extended Kalman filter (EKF) is applied to the estimation module to estimate states from weighted mathematical estimations and sensor measurements. The estimation module produces estimations that are generally a position, velocity, and acceleration of an offshore platform body. In addition, the estimation module regulates a high frequency of motions and environmental forces, because high-frequency motion causes problems of wear and tear on actuators. The control module of dynamic positioning controller calculates the required forces and moments to maintain the offshore platform's position, counteracting environmental forces. Conventional DPS adopts PID controllers that set the relationship between control forces and state errors by applying appropriate gain control. By design, the PID controller sets the gain matrix K in Equation (2.1)

$$\boldsymbol{u} = -\boldsymbol{K}\boldsymbol{e} \tag{2.1}$$

where, error matrix $e = \hat{x} - x_{target}$, u is thruster commands matrix , $\hat{x}$ is a state estimation matrix, and x_{target} is a target state matrix.

Thrust allocation distributes the required forces and moments to control actuators, such as tunnel thrusters, azimuth thrusters, propellers, and rudders. Basically, the control actuator system of an offshore platform is an over-actuated system that is the number of

control actuators that is larger than the number of degrees of freedom for control, so the thruster allocation problem could be modeled as an optimization problem. The thruster allocation problem can be expressed as in Equation (2.2):

$$\tau = \mathrm{B}u \tag{2.2}$$

where, B is the thruster configuration matrix, τ is the 3 degrees of freedom control force in horizontal plane, and u is the input control matrix of the actuator.

Typically, the pseudo-inverse method finds a local optimum for intending total thrust input square minimization based on the Lagrange multiplier optimization theory, as noted in Johansen (2013). The pseudo-inverse matrix is calculated by the pseudo inversed thruster configuration matrix, as in Equation (2.3):

$$C = B^{+} = B^{T}(BB^{T})^{-1} \tag{2.3}$$

where B is the thruster configuration matrix and C is the pseudo-inverse matrix of the configuration matrix. Then the thrust matrix u can be solved as in Equation (2.4):

$$u = C\tau = B^{T}(BB^{T})^{-1}\tau \tag{2.4}$$

The pseudo-inverse matrix method is most advantageous. If a thruster configuration matrix does not have singularity, then it can be calculated by a direct, simple matrix calculation. Thus, the computational burden of the pseudo-inverse method is light. This is why the pseudo-inverse method has been used widely in industrial DP controllers that need to be done in real-time control. This method has two disadvantages, however. The first is that it cannot produce an elaborate solution when environmental forces are higher than thruster capacity. The second is that it cannot consider the constraints of the

thruster, so its performance is degraded when those constraints are reached (Johansen, 2013).

The pseudo-inverse method is used here as a representative, conventional DP thrust allocation algorithm method for comparison with the newly developed thrust allocation algorithm that is the topic of this research. To compensate for the disadvantages of the pseudo-inverse method, Wit (2009) and Rindaroy (2013) proposed quadratic programming as an alternative for the thruster allocation optimization problem. This is appropriate for solving the quadratic form objective and linear constrained optimization problem. Quadratic programming can be applied to the fuel consumption minimization optimization problem, as in Equation (2.5) in Rindaroy (2013). This method is also compared to newly developed method of this research.

Object to

$$minimize\ x^T Qx + u^T Ku - \sum_{i=1}^{n} a_2 P_{i,previous}{}^2 + a_o \tag{2.5}$$

Subject to

$$\tau = Bu,\ u_{\min} < u < u_{\max},\ \dot{u}_{\min} < \dot{u} < \dot{u}_{\max}$$

where, Q and K are weight matrixes, P is the power, u is the thruster command matrix, τ is a required force matrix, and B is a control effectiveness matrix.

2.2.1 Controller Design: PD Controller

The required forces and moments that can maintain the position of an offshore platform can be defined by multiplication PID gain and error matrix. The key function of PID controller design is to define the gain control. PID controller design assumes a system of offshore platform as a linear, time-invariant system. A linear, time-invariant system of equations of motion follows the form (Ryu, 2005), seen in Equation (2.6):

$$\dot{\mathbf{x}} = \mathbf{Ax} + \mathbf{Bu}, \mathbf{y} = \mathbf{Cx} + \mathbf{v} \tag{2.6}$$

where, dot (·) denotes time derivative, and each vector written in lower case can be described by the following set of definitions:

State $\mathbf{x} = [u, x, v, y, \omega, \psi]^T$ Control Input $u = \left[\tau_x, \tau_y, \tau_\phi\right]^T$

Measurement $\mathbf{y} = [x, y, \psi]^T$ Measurement-Noise $\mathbf{v} = [v_X, v_Y, v_\psi]^T$

where, $\mathbf{A} = \mathbf{M}^{-1}\begin{bmatrix} 0 & 0 & 0 & 0 & 0 & 0 \\ 1 & 0 & 0 & 0 & 0 & 0 \\ 0 & 0 & 0 & 0 & 0 & 0 \\ 0 & 0 & 1 & 0 & 0 & 0 \\ 0 & 0 & 0 & 0 & 0 & 0 \\ 0 & 0 & 0 & 0 & 1 & 0 \end{bmatrix}$ $\mathbf{B} = \mathbf{E} = \mathbf{M}^{-1}\begin{bmatrix} 1 & 0 & 0 \\ 0 & 0 & 0 \\ 0 & 1 & 0 \\ 0 & 0 & 0 \\ 0 & 0 & 1 \\ 0 & 0 & 0 \end{bmatrix}$ $\mathbf{C} = \begin{bmatrix} 0 & 1 & 0 & 0 & 0 & 0 \\ 0 & 0 & 0 & 1 & 0 & 0 \\ 0 & 0 & 0 & 0 & 0 & 1 \end{bmatrix}$

$$\mathbf{M} = \begin{bmatrix} M_{11} & 0 & 0 & 0 & 0 & 0 \\ 0 & 1 & 0 & 0 & 0 & 0 \\ 0 & 0 & M_{22} & 0 & M_{26} & 0 \\ 0 & 0 & 0 & 1 & 0 & 0 \\ 0 & 0 & M_{62} & 0 & M_{66} & 0 \\ 0 & 0 & 0 & 0 & 0 & 1 \end{bmatrix}$$

$$M_{11} = m + a_{11}(0), M_{22} = m + a_{22}(0), M_{26} = m + a_{26}(0), M_{62} = m + a_{62}(0), M_{66} = I + a_{66}(0)$$

, m the mass of the floating structure, I is the moment of inertia in z-direction, and $a_{ij}(0)$ added masses in low frequency, and $\hat{x}$ is the state estimation vector.

For calculating PID gains, the linear quadratic regulator (LQR) theory was applied. The LQR is conventionally used for finding optimal control gain matrix K that can minimize state error and thruster usage together, as in Equation (2.7)(Ryu, 2005):

$$J = \int_0^\infty \left\{ \mathbf{e}(t)^T \mathbf{Q}_o \mathbf{e}(t) + \mathbf{u}(t)^T \mathbf{R}_o \mathbf{u}(t) \right\} dt \tag{2.7}$$

where, J is objection function, Q_0 and R_0 are the weight factors for the error and input, e(t) is the state error matrix time series, and u (t)is the input matrix time series.

Prior research (Rindarøy & Johansen, 2013) analyzed only the fuel-optimal thrust allocation in the static domain, but the time-accumulated fuel consumption value is more important than the instantaneous value. Moreover, it cannot evaluate whether the computation speed of the thruster allocation algorithm is feasible for real-time DP control.

2.2.2 Optimization Variable Design

Optimization strategy research has been conducted since 1960. At first, it focused to the linear problem that has linear object functions and constraints. Then, that was expanded into nonlinear problems that have nonlinear object functions or constraints. Currently, various optimization methods are used, and these are categorized according to the form of optimization problem (Rao & Rao, 2009). Table 2.1 shows the categorization of classical optimization strategy.

Table 2.1 Optimization Scheme Categorization

	Linear Object Function	Quadratic Object Function	Nonlinear Object Function
Linear Constraint	Simplex Method Linear Programming	Quadratic Programming Sequential Programming	Nonlinear Programming
Nonlinear Constraint			Genetic Algorithm, Penalty Method

The procedure of optimization consists of three stages: optimization variable design, optimization problem formulation, and a numerical approach. It is necessary to design realistic optimization variables that reflect the gamut of potential real-world problems and make the solution for optimization credible. The optimization problem formulation is the stage that defines object functions and constraints according to the optimization strategy. The numerical approach is the step that implements the optimization mathematical form into the calculation program. The following section describes the parameters that are important in the thruster allocation and how these can be derived in mathematical form.

Fuel Consumption

This research focuses on the thrust allocation optimization algorithm design that can reduce the fuel consumption of offshore platforms. Therefore, fuel consumption is the most important parameter, because it is the primary subject of this study. It is essential to arrive at a relationship between thrust and fuel consumption, because the object function should be parametrized by the design variable of the optimization problem. Fuel

consumption is the function of a power series that can be expressed by thrust.

According to Rindarøy and Johansen (2013), power consumption and thrust have the relationship seen in Equation (2.9).

$$\begin{aligned} T &= T_o n^2 \\ P &= P_o n^3 = |T|^{\frac{3}{2}} \\ F &= a_0 + a_1 P + a_2 P^2 = a_0 + a_1 |T|^{\frac{3}{2}} + a_2 |T|^3 \end{aligned} \tag{2.9}$$

where, F is a fuel consumption, T is a thrust, P is power, T_0 is a maximum thrust, P_0 is a maximum power, n is a normalized revolution per minute, and a_0, a_1, a_2 are fuel consumption coefficients

Gas Emissions (CO_2)

Carbon dioxide (CO_2) is the largest gas emissions produced by the offshore vessel operation. As interest in the so-called greenhouse gases surges, the reduction effort becomes increasingly significant. According to Jayaram (2010), the offshore vessel engine load and the amount of carbon dioxide has a relationship as seen in Equation (2.10). The relation between CO_2 and fuel consumption can be derived as in Equation (2.11) by using Equation (2.9). Also, the relationship of CO_2 and fuel consumption is presented in Figure 2.1. This gas emissions index will be presented and evaluated in the simulation results.

$$CO_2 = 1.29 \times P \tag{2.10}$$

$$F = a_o + a_1 \left(\frac{CO_2}{1.29} \right) + a_2 \left(\frac{CO_2}{1.29} \right)^2 \tag{2.11}$$

where, F is a fuel consumption, T is a thrust, P is power, T_0 is a maximum thrust, P_0 is a maximum power, n is a normalized revolution per minute, and a_0, a_1, a_2 are fuel consumption coefficients

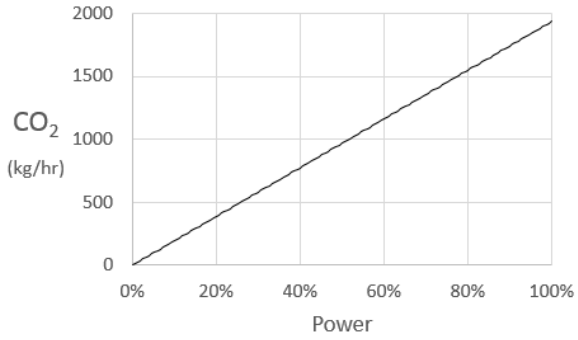

Figure 2.1 Relationship between Carbon Dioxide and Power

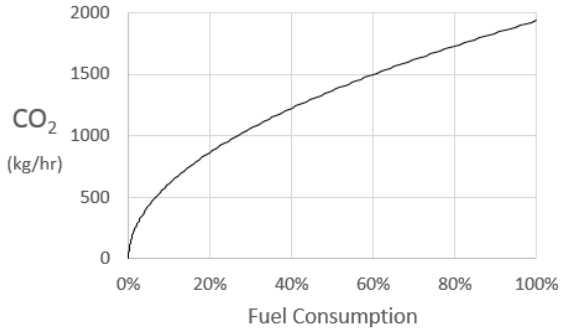

Figure 2.2 Relationship between Carbon Dioxide and Fuel Consumption

Thruster Constraints

Two physical constraint groups of thrusters are considered for the optimal thrust allocation problem of fuel consumption and gas emissions. The first constraint group is the thrust and thruster angle constraint, as in Equation (2.12).

$$T_{\min} < T < T_{\max}, \alpha_{\min} < \alpha < \alpha_{\max} \tag{2.12}$$

where, T is a thrust, α is an azimuth angle, T_{max} *and* T_{min} are maximum and minimum of thruster capacity, and $\alpha_{\max}$ *and* $\alpha_{\min}$ are maximum and minimum angle of thrusters.

Another constraint group is the thrust and thruster angle rate constant, which can consider the movable range of thrust and thrust angle per unit time, as in Equation (2.13).

$$\dot{T}_{\min} < \dot{T} < \dot{T}_{\max}, \dot{\alpha}_{\max} < \dot{\alpha} < \dot{\alpha}_{\max} \tag{2.13}$$

were, $\dot{T}$ is a thrust rate , $\dot{\alpha}$ is an azimuth angle rate, $\dot{T}_{\max}, \dot{T}_{\min}$ are maximum and minimum of thruster capacity change rate, and $\dot{\alpha}_{\max}, \dot{\alpha}_{\min}$ are maximum and minimum angle change rate of thrusters.

Required Forces and Moments Constraints

Thrust allocation produces thruster commands by satisfying the required forces and moment constraints to maintain the position of an offshore platform while counteracting environmental forces. In this research, the target object motion is the horizontal motion. Therefore, three degrees of freedom required force and moment constraints can be formulated as in Equation (2.14).

$$\begin{aligned} X &= T_{x1}\cos\alpha_1 + T_{x2}\cos\alpha_2 + ...T_{xn}\cos\alpha_n \\ Y &= T_{y1}\sin\alpha_1 + T_{y2}\sin\alpha_2 + ...T_{yn}\sin\alpha_n \\ N &= y_1T_{x1}\cos\alpha_1 - x_1T_{y1}\sin\alpha_1 + y_2T_{x2}\cos\alpha_2 \\ &-x_2T_{y2}\sin\alpha_2 + ... + y_nT_{xn}\cos\alpha_n - x_nT_{yn}\sin\alpha_n \end{aligned} \tag{2.14}$$

where, *X, Y, N* are surge and sway force, and yaw moment.

Thrust Allocation Optimization Problem Formulation

Thrust allocation can be formulated as an optimization problem form that uses the optimization design variables modeled in the previous section. That problem has a fuel consumption object function, mechanical constraints, and required force constraints. It can be expressed as in Equation (2.15):

Object to

Minimize Fuel Consumption : $a_0 + a_1 |T|^{\frac{3}{2}} + a_2 |T|^3$ (2.15)

Subject to

1.*Thrust* & *Azimuth Angle Constraint* : $T_{\min} < T < T_{\max}, \alpha_{\min} < \alpha < \alpha_{\max}$

2.*Thrust* & *Azimuth Angle Rate Constraint* : $\dot{T}_{\min} < \dot{T} < \dot{T}_{\max}, \dot{\alpha}_{\max} < \dot{\alpha} < \dot{\alpha}_{\max}$

3.*Required Forces and Moment Constraint* :

$X = T_{x1}\cos\alpha_1 + T_{x2}\cos\alpha_2 + ...T_{xn}\cos\alpha_n$

$Y = T_{y1}\sin\alpha_1 + T_{y2}\sin\alpha_2 + ...T_{yn}\sin\alpha_n$

$N = y_1T_{x1}\cos\alpha_1 - x_1T_{y1}\sin\alpha_1 + y_2T_{x2}\cos\alpha_2 - x_2T_{y2}\sin\alpha_2 + ... + y_nT_{xn}\cos\alpha_n - x_nT_{yn}\sin\alpha_n$

Penalty Method Optimization Problem Formulation

The penalty method is an optimization method that replaces a constrained optimization problem by combination of unconstrained problems whose solution ideally converges on the solution of the original constrained problem. The advantage of the penalty method is that it has no limitation on how to construct the object function and constraint. Therefore, this can be good to apply to fuel-consumption minimization thrust allocation that has nonlinear optimization.

The penalty method can be formulated as in Equation (2.16):

Object to

$$\min\left(\frac{1}{2}x^T Hx+\frac{1}{2}u^T Ku+c\left(\begin{array}{l}\max\{0,\mathrm{u}-\mathrm{u}_{\max}\}^2+\max\{0,u_{\min}-u\}^2\\+\max\{0,\dfrac{u_{previous}-\mathrm{u}_{current}}{dt}-\dot{\mathrm{u}}_{\max}\}^2+\left(\tau-Bu\right)^2\end{array}\right)\right) \tag{2.16}$$

where, $x=(x,y,\phi,u,v,r)^T, u=(T_1\cos\alpha,T_1\sin\alpha,...,T_n\cos\alpha,T_n\sin\alpha)$, H is a state weight matrix, K is the fuel consumption parameter weight matrix, τ is the required force and moment matrix, B is the thrust allocation matrix, u is thruster matrix

The mechanism of the penalty method is that if a solution is located outside of the constraint boundary, then its object function value diverges to infinity so that candidates that violate constraints are excluded (You, Choi, Kim, & Lee, 2014).

2.3 Validation

To validate the developed thrust allocation method, Rindarøy and Johansen (2013) used the quadratic programming method for the cases of power minimization and fuel consumption minimization. Those problems involve distribution of required surge force (100KN) and sway forces (200KN) to the forward tunnel thruster, the forward azimuth thruster, the aft port azimuth thruster, and the aft starboard azimuth thruster. The offshore support vessel bourbon UT 745E was used for the target vessel. The principal dimension of the bourbon UT745E is presented in Table 2.2

Figure 2.3 Bourbon UT 745-Type Offshore Support Vessel

Table 2.2 Principal Dimensions of Bourbon UT 745-Type Offshore Support Vessel

Designation	Symbol	Unit	Quantity
Vessel size		GT	3325t
Length Over All	LoA	m	88.6
Breadth	B	m	78.8
Draft	T	m	18.9

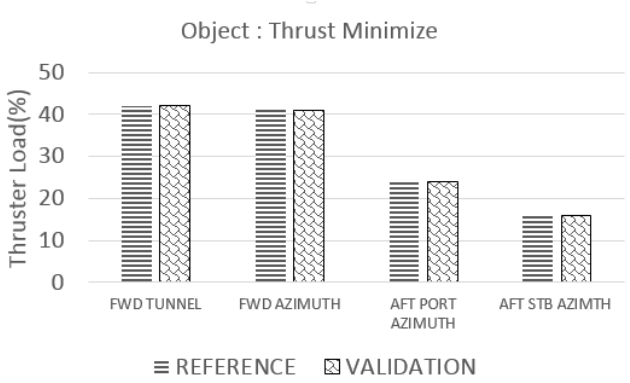

Figure 2.4 Thrust Allocation Validation – Object Function: Thrust Minimization

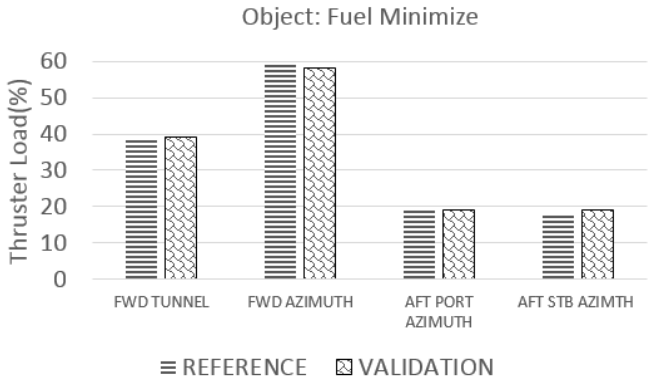

Figure 2.5 Thrust Allocation Validation – Object Function: Fuel Minimization

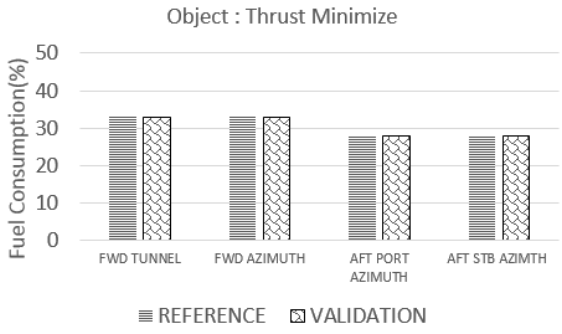

Figure 2.6 Fuel Consumption Validation – Object Function: Thrust Minimization

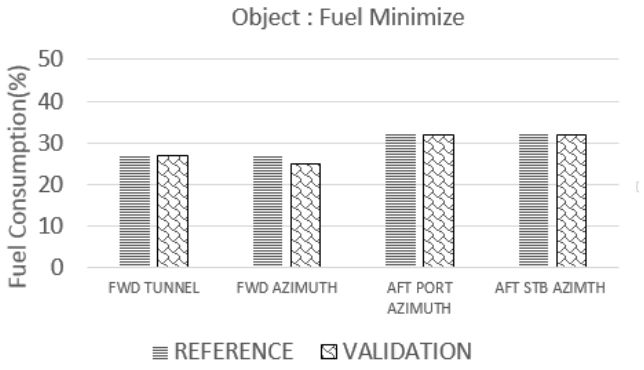

Figure 2.7 Fuel Consumption – Object Function: Fuel Minimization

Figures 2.4,5,6 and 7 depict the thrust allocation validation results. Figure 2.4 and 2.5 show the bar charts developed by Rindarøy and Johansen (2013) and the validation case in the thruster usage (%) according to forward and aft thrusters. The present thrust allocation results based on quadratic programing for thruster minimization and fuel optimization agree well with those of Rindarøy and Johansen (2013). Figure 2.6 and 2.7 similarly compare the results of fuel consumption depending on different optimization object functions. Consistently, the fuel consumption results of the present validation cases demonstrate coherence with the reference cases. Analyzing these figures, it can be determined that thruster usage was larger in the fuel-minimization case than the thrust-minimization case; meanwhile, fuel consumption was smaller in the fuel-optimal case than the thrust optimal case. This discrepancy was due to different object functions in all cases; the present and Rindaroy's results agree very well, within 1% error.

2.4 Simulation Results

Next, simulation in the time domain of six degrees of freedom (6DOF) hull, mooring, and riser coupled dynamic positioning were conducted to evaluate fuel consumption and gas emissions by using fuel optimal thrust allocation algorithms. Those thrust allocation algorithms were optimized by the genetic algorithm, the pseudo-inverse method, quadratic programming, and the penalty method. Accordingly, dynamics of the ship, environmental forces, and the dynamic positioning control frame were simultaneously implemented in the simulation program.

2.4.1 Time Domain Simulation Conditions

Before applying the newly developed thrust allocation algorithm to the dynamic positioning control system, the conventional pseudo-inverse-method-based thrust allocation and PID controller were modeled and checked with the results of Ryu (2005) A Kalman filter and PID controller were implemented in the DP controller. Frequency-domain analysis was performed using frequency diffraction motion analysis tool for hydrodynamic coefficients and wave forces. Subsequently, the time-domain 6DOF motion analysis was performed using CHARM 3D (Ryu, 2005). The DP FPSO has a 200,000-ton tanker moored in 1,829m water depth. The bow turret is located 63.55m from the F.P. The principal dimension of the DP FPSO is presented in Table 2.3.

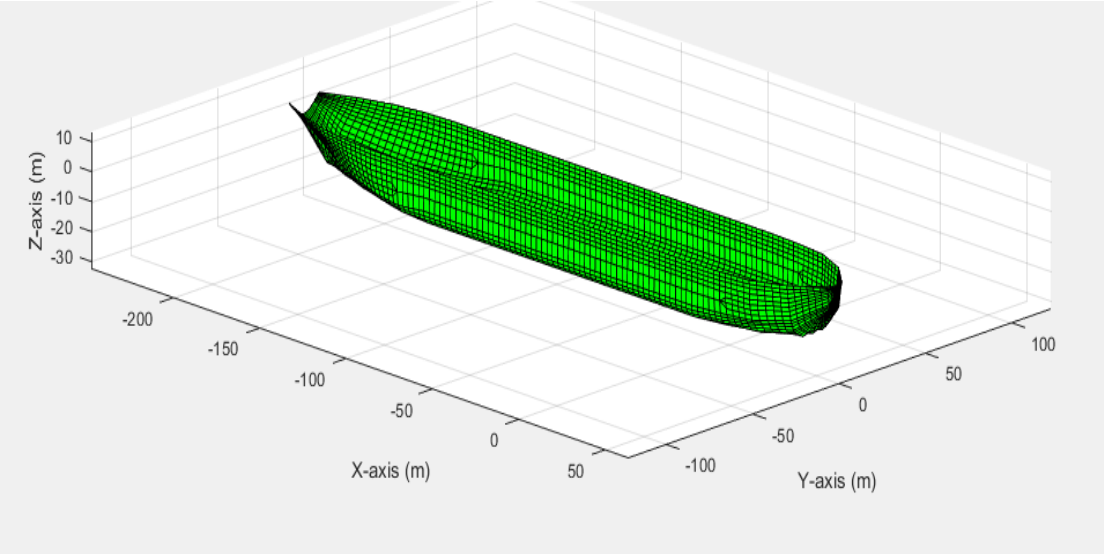

Figure 2.8 DP FPSO Mesh Model

Table 2.3 Principal Dimensions of the FPSO

Designation	Symbol	Unit	Quantity
Production level		bpd	120000
Storage		bbls	1440000
Vessel size		kDWT	200
Length b/w perpendiculars	Lpp	m	310
Breadth	B	m	47.2
Depth	H	m	28.0
Draft	T	m	18.9
Length to beam ratio	L/B		6.57
Beam to draft ratio	B/T		2.5
Displacement	∆	ton	240869
Block coefficient	Cb		0.85
Center of buoyancy (forward section 10)	FB	m	6.6
Water plane area	A	m^2	13400
Water plane coefficient	Cw		0.9164
Center of water plane area forward section 10	FA	m	1.0
Center of gravity above base	KG	m	13.3
Metercentric height transverse	MGt	m	5.8
Metercentric height longitudinal	MGl	m	403.8
Trans. radius of gyration in air	Kxx	m	14.8
Long. radius of gyration in air	Kyy	m	77.5
Yaw radius of gyration	Kzz	m	79.3
Wind area front	Af	m^2	1012
Wind area side	Ab	m^2	3772
Turret in centerline behind Fpp (20.5% Lpp)		m	63.5
Turret elev. below tanker base		m	1.5
Turret diameter		m	15.8

The coordinate system and environmental direction are presented in Figure 2.9.

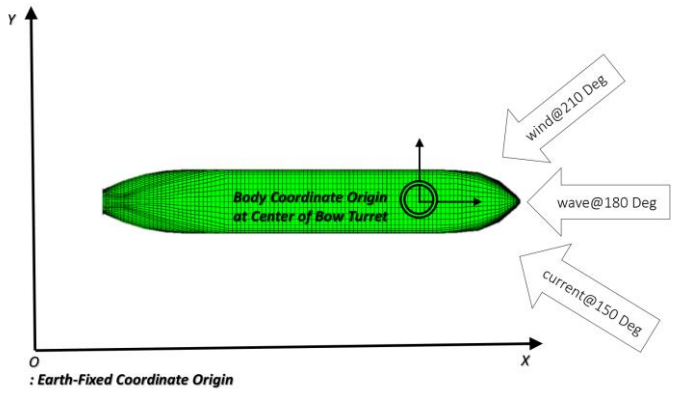

Figure 2.9 Coordinate System and Environmental Load Directions

One-year and 100-year Gulf of Mexico hurricane conditions were used as the environmental conditions in the simulation. A Joint North Sea Wave Project (JONSWAP) spectrum was used for the input sea, as summarized in Table 2.4.

The OCIMF wind and current coefficient data for a cylindrical bow with full loading conditions were selected for the simulation. The storm-induced current flows were from 30 degrees clockwise of the incoming wave direction. The current velocity is assumed to be 0.33 or 1.07 m/sec at the water surface. Regarding the wind spectrum, the America Petroleum Institute (API) wind spectrum was used to generate the dynamic wind forces. The applied wind speed was 14.4 or 41.1m/sec at 10m, and its direction was 30 degrees counterclockwise of the incoming wave direction. The corresponding wind spectrum is shown in Figure 2.10.

Table 2.4 Simulation Conditions: The Environment

		GOM 1-Year Storm	GOM 100-Year Storm
WAVE	Significant Wave Height H_s	4.3m	12.19m
	Peak Period T_p	9sec	14sec
	Overshoot Parameter γ	2	2.5
WIND		14.3m/sec at 10m	41.1m/sec at 10m
CURRENT		0.33m/sec	1.07 m/sec

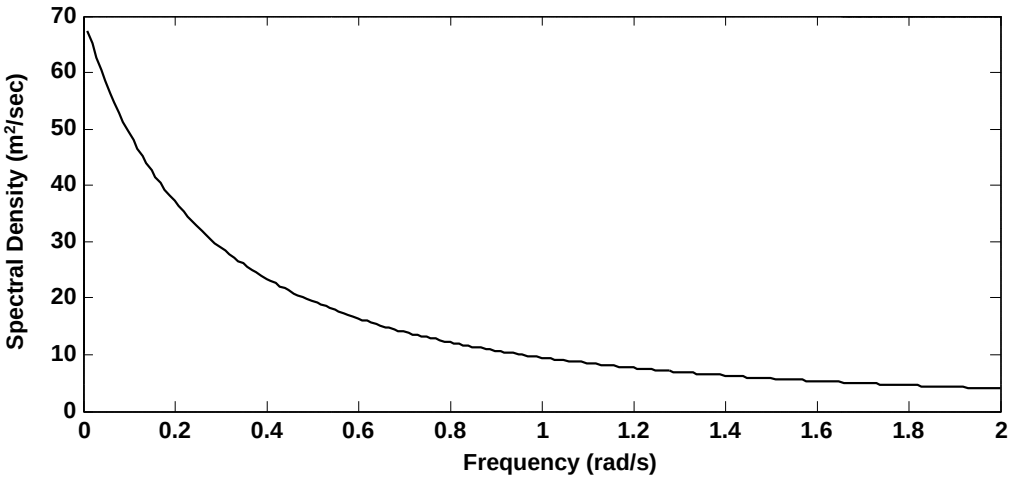

Figure 2.10 API Wind Spectrum

$$S(\omega) = \frac{\sigma^2(z)}{2\pi f_p \left[1 + \frac{1.5}{2\pi f_p}\right]^{\frac{5}{3}}}$$

where, the average factor f_p was derived from measured spectra and the standard deviation of wind speed $\sigma(z)$ at 10m above the mean water level are expressed as

$$f_p = \frac{0.025 V_w(z)}{z},$$

$$\sigma(z) = 0.15\left(\frac{z}{20}\right)^{-0.125} V_w(z)$$

where, $V_w(z)$ is the one hour mean wind speed (m/s) at z m above a mean water level.

The FPSO equips 12 chain-polyester-chain mooring lines and 13 steel catenary risers.

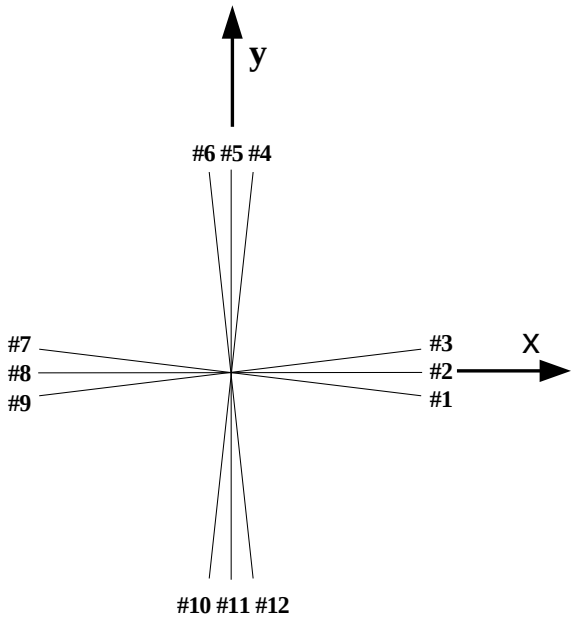

Figure 2.11 FPSO Mooring Lines Arrangement and Numbering (Ryu & Kim, 2005)

Table 2.5 Mooring Line Details

Designation	Unit	Quantity
Water depth	m	1829
Pre-tension	kn	1424
Number of lines		4×3
Degree between the 3 lines	deg.	5
Length of mooring line	m	2652
Radius of location of chain stoppers on turn table	m	7.0
Segment 1: Chain		
Length at anchor point	m	121.9
Diameter	cm	9.52
Dry weight	N/m	1856
Weight in water	N/m	1615

Table 2.5: Continued

Designation	Unit	Quantity
Stiffness AE	kN	912120
Segment 2: Polyester		
Length	m	2438
Diameter	cm	16.0
Dry weight	N/m	168.7
Weight in water	N/m	44.1
Stiffness AE	kN	186800
Segment 3: Chain		
Length at anchor point	m	91.4
Diameter	cm	9.53
Dry weight	N/m	1856
Weight in water	N/m	1615
Stiffness AE	kN	912120

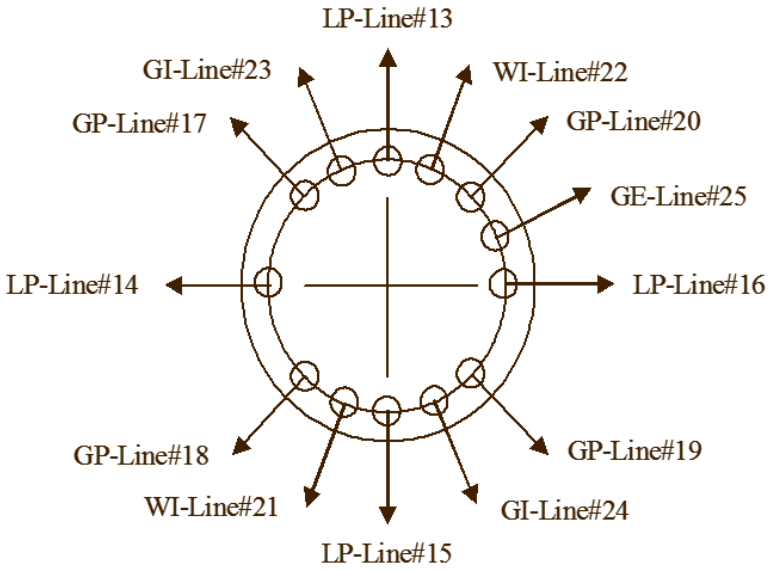

Figure 2.12 FPSO Riser Arrangement and Numbering (Ryu & Kim, 2005)

Table 2.6 Riser Details

Riser Type	Top Tension	OD	AE	EI	Weight Dry/Wet	Cdn
	kN	cm	kN	kNm2	N/m	
Liquid Production (LP)	2224	44.5	1.83×107	276	1927 1036	1
Gas Production (GP)	1223	38.6	1.08×107	113	1708 525	1
Water Injection (WI)	4048	53.1	1.86×107	224	2802 1897	1.414
Gas Injection (GI)	2714	28.7	3.14×106	64	1810 1168	1.414
Gas Export (GE)	912	34.3	8.63×106	71	1357 423	1
Total Length of Risers		3657.4 m				

2.4.2 Gulf of Mexico 100-Year Storm Conditions

- Bow, Stern Group Thruster Configuration

The DP FPSO, equipped with six azimuth thrusters, was simulated for evaluating the performance of fuel-consumption and gas-emissions reduction. The 6DOF coupled time-domain simulations were carried out under the GOM 100-year storm condition. The thruster configuration and constraints are presented in Figure 2.13, Table 2.7, and Table 2.8.

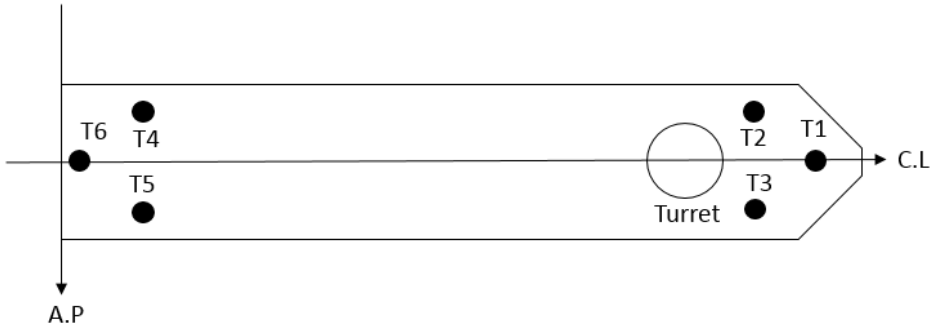

Figure 2.13 Group Thruster Configuration

Table 2.7 Thruster Details

Thruster Type	Azimuth Thruster
Thruster Maximum Capacity	150 KN
Thruster Maximum Change Rate	20 KN /sec
Thruster Angle Change Rate	10deg / sec
Thruster Position (A.P=0, C.L=0)	T1(290m,0m), T2(275 m,-15m), T3(275m,15m) T4(35m,-15m) T5(35m,15m) T6(20m,0m)

Table 2.8 Thruster Constraints

Thruster Capacity Constraint (KN)	$0 < T_{1,2,3,4,5,6} < 150$
Thruster Angle Constraint (deg)	$0 < \alpha_{1,2,3,4,5,6} < 360$
Thruster Rate Constraint Rate (KN/sec)	$0 < \dot{T}_{1,2,3,4,5,6} < 20$
Thruster Angle Change Rate (deg/sec)	$0 < \dot{\alpha}_{1,2,3,4,5,6} < 20$
Required Force Constraint	

Trajectories based on different thrust allocation methods are presented in Figure 2.14. The left graph shows the trajectory of the penalty-method-based thrust allocation algorithm. The one on the right presents trajectories of the pseudo-inverse method and quadratic programming. The penalty method shows slightly better position-keeping performance in surge motion, but there is no appreciable improvement in sway and yaw motions. The maximum of riser top tension of the penalty method and other methods are almost the same as those found in Table 2.9.

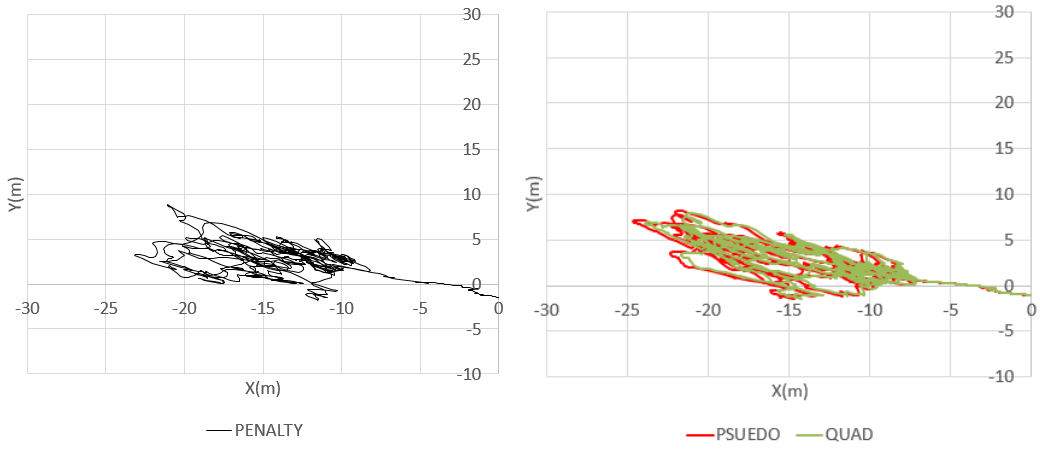

Figure 2.14 Surge -Sway Trajectories by Three Different Thrust Allocation Algorithms

Table 2.9 Statistical Analysis Results by Three Different Thrust Allocation Algorithms

	Surge Mean(M)	Surge STD	Surge Max	Sway MEAN (M)	Sway STD	Sway MAX	Yaw MEAN (M)	Yaw STD	Yaw MAX	TOP TENSION MAX
PENALTY	-13.3	4.87	-23.4	2.45	1.84	7.9	8.89	3.2	13.51	8108KN
PSEUDO	-13.4	5.64	-24.9	2.48	2.18	7.2	8.78	3.1	13.10	8108KN
QUAD	-13.1	5.53	-24.7	2.43	2.13	7.1	8.81	3.2	13.52	8109KN

Figure 2.15 shows the 6DOF motion simulation results when the penalty method is used for thrust allocation method.

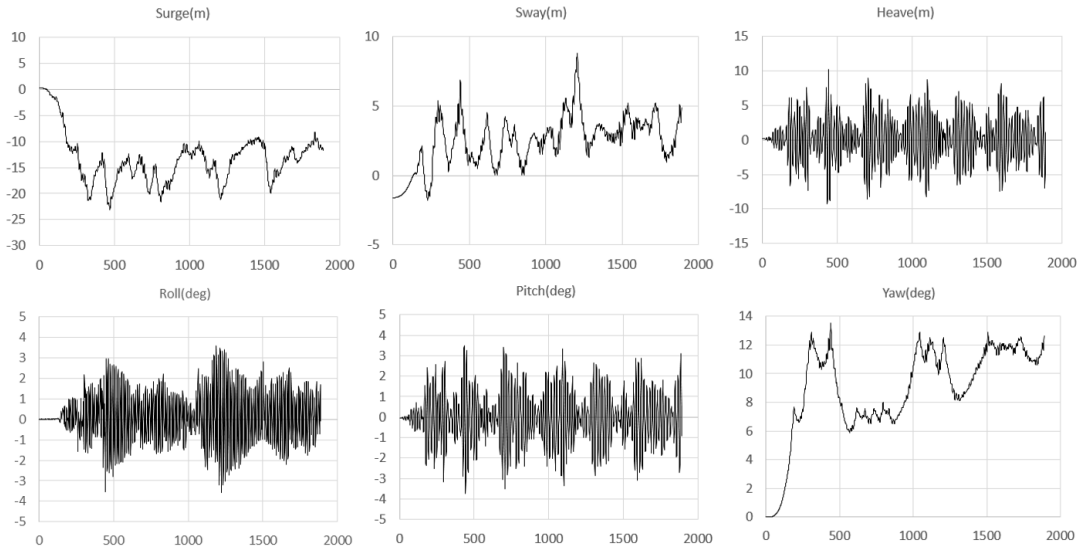

Figure 2.15 6DOF Motion by Penalty Method Thrust Allocation

Figure 2.16 shows fuel-consumption time history by three different thrust allocation methods. The red line is the pseudo-inverse method, and the green and black lines are the quadratic programming and penalty method. As the graph shows, the pseudo-inverse method consumes the largest amount of fuel compared to other thrust allocation methods. Peaks of the pseudo-inverse method occur when environmental forces reach the

thruster allocation capacity. The peak of the penalty method is lower than of the pseudo-inverse method and quadratic programming, at 32% and 26%, respectively. In case of the accumulated fuel consumption amount, the penalty method saves 6% and 5% compared the pseudo-inverse method and quadratic method.

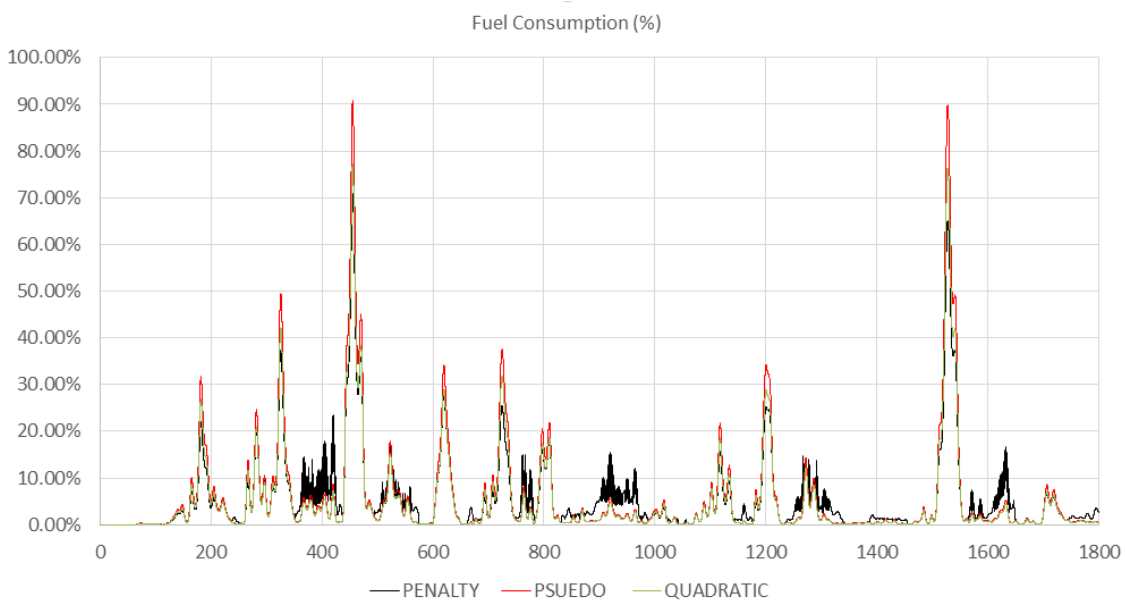

Figure 2.16 Fuel Consumption Index by Three Different Thrust Allocation Methods

Figure 2.17 additionally shows the fuel-consumption history when the genetic algorithm is used. The genetic algorithm further reduced fuel consumption by more than 2% compared to the penalty method. Although genetic algorithm shows the best fuel reduction performance, it is not feasible for a real-time DP controller because it takes much longer than the other methods. The genetic algorithm generally takes more than one minute per one thrust allocation step to optimize. Meanwhile, the penalty method, the pseudo-

inverse method, and the quadratic programming methods take less than one second for thrust allocation.

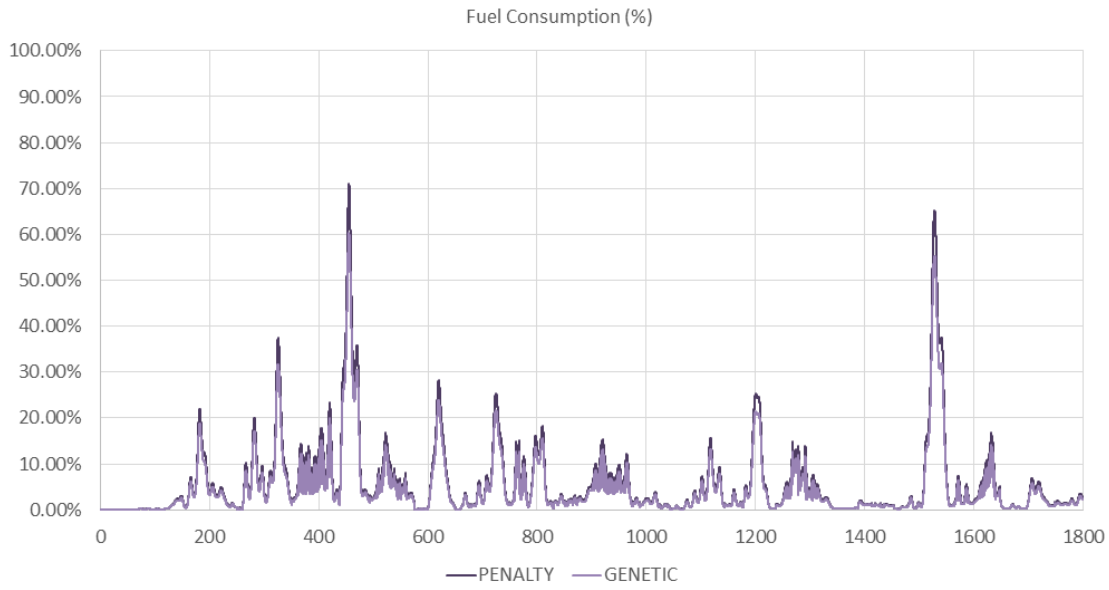

Figure 2.17 Fuel Consumption Index by Penalty Method and Genetic Algorithm

Figure 2.18 shows the CO_2 amounts produced during the dynamic positioning operation. The penalty method performed better than the pseudo-inverse method and quadratic programming, because CO_2 levels and fuel use have a direct, proportional relationship. The peak of the penalty method is lower than that of the pseudo-inverse and quadratic methods by a maximum of 16% and 14%, respectively. For accumulated CO_2 emissions, the penalty method saves 4% over the pseudo-inverse and quadratic programming methods.

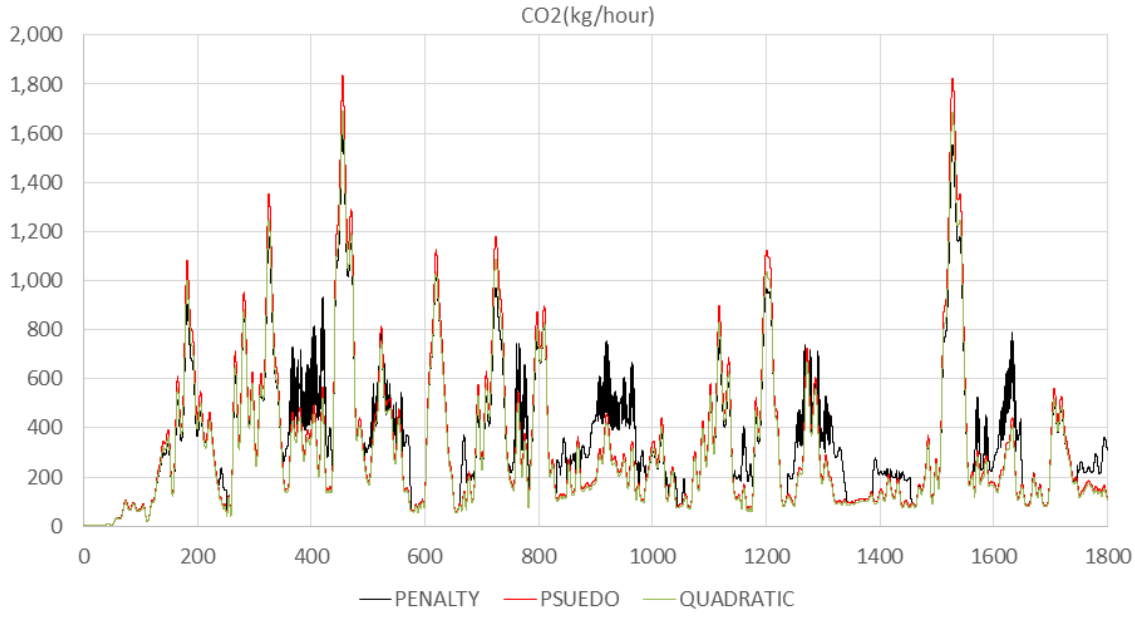

Figure 2.18 CO_2 Index by Three Different Thrust Allocation Methods

- Single Alignment

Next, to find out whether the previous conclusion depends on a specific thruster arrangement, a different thruster configuration was examined. In this case, the same six azimuth thrusters were arranged by single alignment, as shown in Figure 24. The 6DOF coupled time domain simulation was carried out under the same Gulf of Mexico 100-year storm conditions. The thruster configuration and constraints are presented in Figure 2.19, Table 2.10, and Table 2.8.

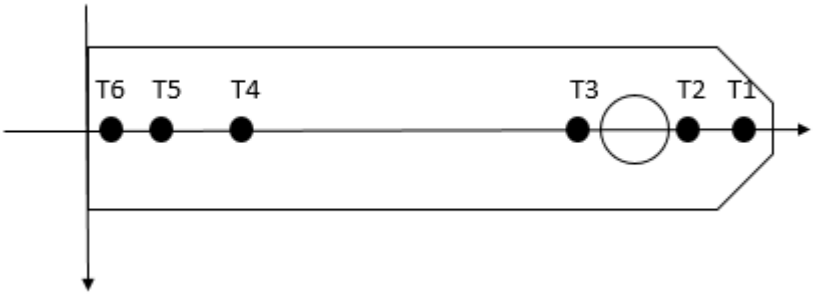

Figure 2.19 Single Alignment Thruster Formation

Table 2.10 Thruster Information

Thruster Maximum Capacity	150 KN
Thruster Maximum Change Rate	20 KN /sec
Thruster Angle Change Rate	10deg / sec
Thruster Position (A.P=0, C.L=0)	T1(290m,0m), T2(260m,0m), T3(220m,0m) T4(90m,0m) T5(50m,0m) T6(20m,0m)

Trajectories by three different thrust allocation methods are represented in Figure 2.20. The position-keeping differences among the different thruster allocation methods are bigger than in the previous case because the single alignment has a smaller moment arm, so it reaches the thruster constraint more frequently. The pseudo-inverse shows the best position-keeping performance, but its difference is negligible compared to other methods. The maximum riser top tensions of the three methods are almost same.

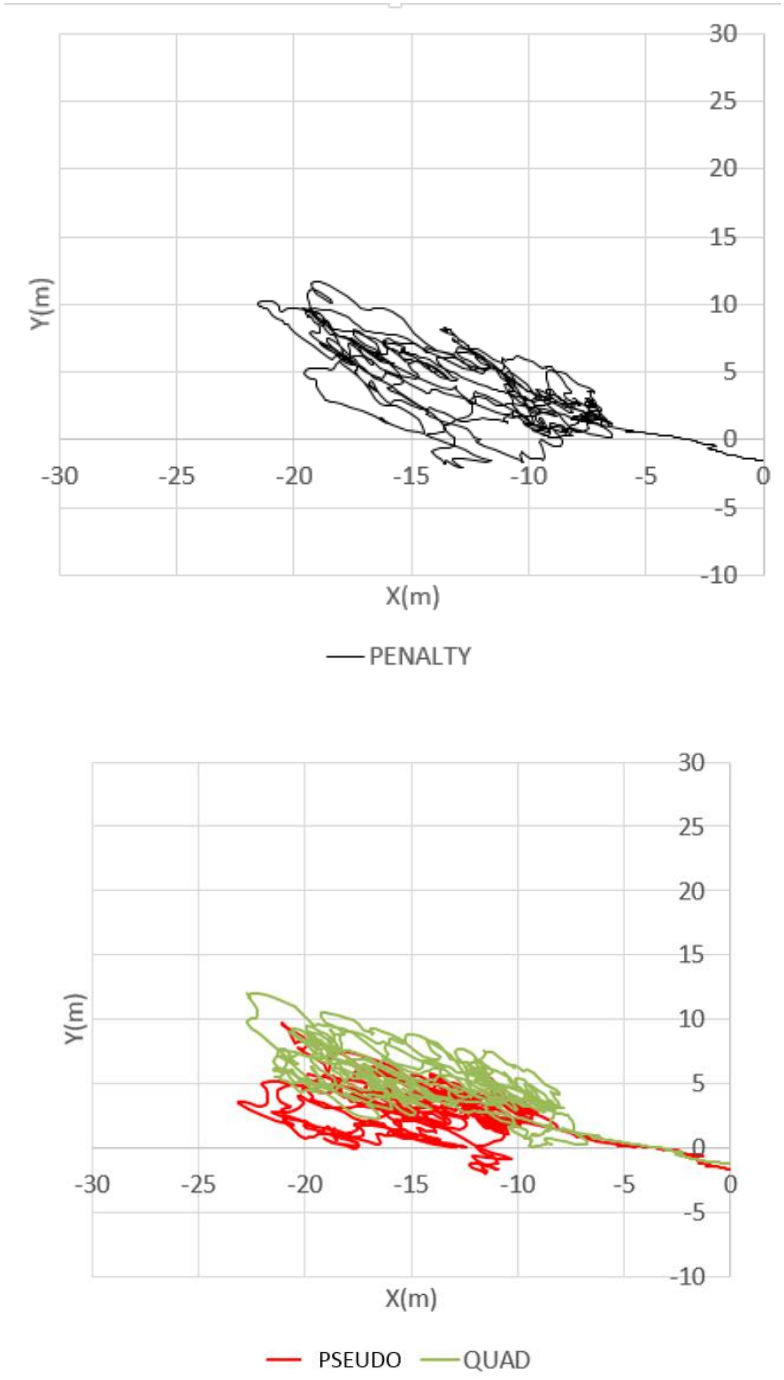

Figure 2.20 Surge and Sway Trajectories by Three Different Thrust Allocation Algorithms

Table 2.11 Mean Value and Standard Deviation by Three Different Thrust Allocation Algorithms

	Surge Mean(M)	Surge STD	Surge Max	Sway MEAN(M)	Sway STD	Sway MAX	Yaw MEAN (M)	Yaw STD	Yaw MAX	TOP Tension Max
PENALTY	-11.73	4.94	-21.56	3.55	3.11	11.68	8.50	3.08	15.30	8110KN
PSEUDO	-13.27	4.87	-23.16	2.69	2.02	9.72	8.89	3.20	13.51	8109KN
QUAD	-13.20	5.37	-22.72	4.73	2.73	12.04	8.90	3.31	15.52	8110KN

Figure 2.21 shows the plotting of 6DOF motions of DP-controlled FPSO with the penalty method and single-line method. When compared to the previous DP arrangement, the efficiency of sway and yaw modes is slightly diminished.

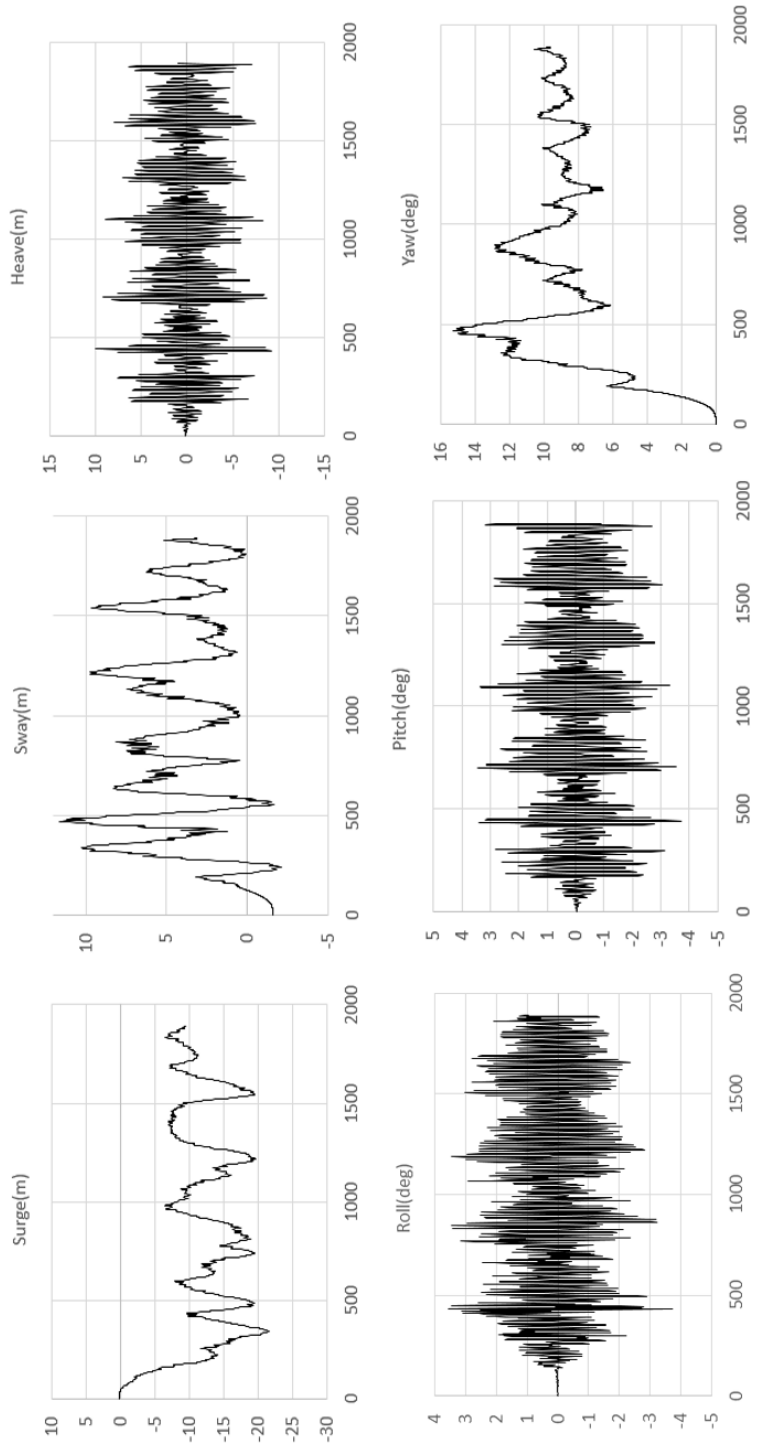

Figure 2.21 6DOF Motions by Penalty Method Single-Alignment Thruster Configuration

Figure 2.22 presents the fuel-consumption index of three different thruster-allocation methods in single-thruster alignment. The total accumulated fuel consumption was increased by 1% compared to the group thruster configuration. This difference comes from the thrust allocation efficiency depending on thruster configuration. The peak of the penalty method is lower than those of the pseudo-inverse method and quadratic programming by a maximum of 36% and 30%, respectively. In the case of accumulated fuel consumption, the penalty method saves 7% and 6% in total fuel consumption compared to the pseudo-inverse and quadratic methods.

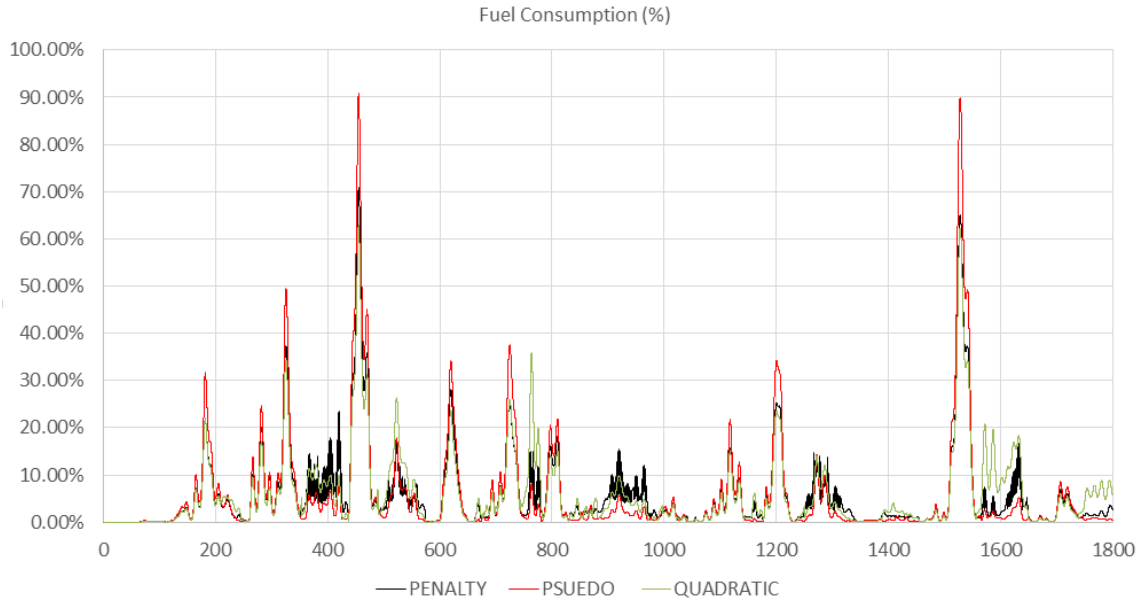

Figure 2.22 Fuel Consumption Index Time History by Three Different Thrust Allocation Algorithms

Figure 2.23 shows the CO_2 amounts produced during the dynamic positioning operation. The peak of the penalty method is lower than those of pseudo-inverse and quadratic methods by a maximum of 20% and 16%, respectively. In case of the accumulated CO_2 emissions, the penalty method produced 5% and 4% less CO_2 compared to the pseudo-inverse and quadratic programming methods.

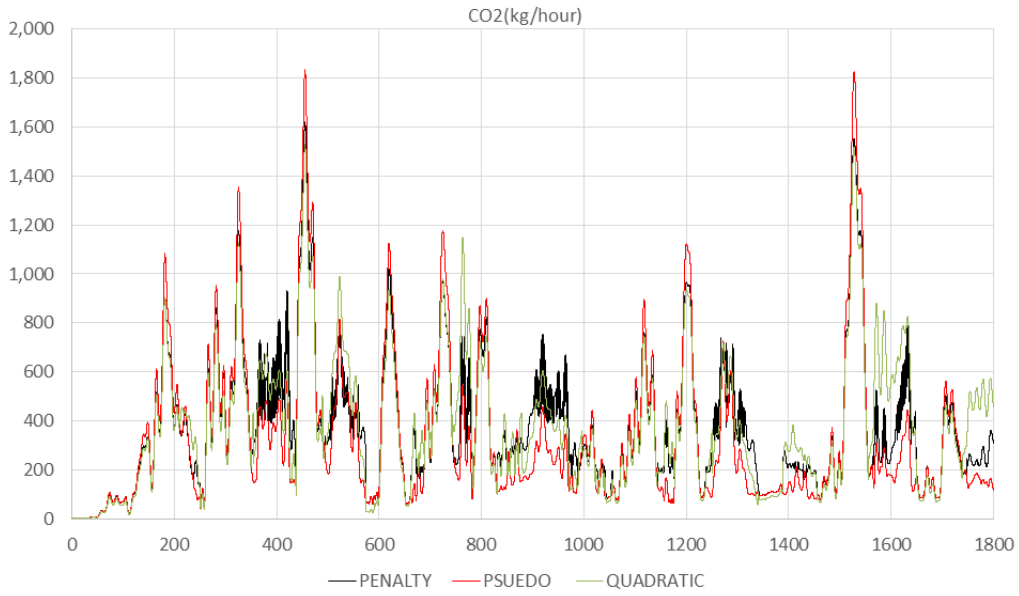

Figure 2.23 CO_2 Index Time History by Three Different Thrust Allocation Algorithms

2.4.3 Gulf of Mexico One-Year Storm Conditions

Next comes an investigation of whether the previous conclusion is affected by different storm conditions. A simulation under Gulf of Mexico (GOM) one-year storm conditions was conducted to analyze the change due to mild environmental conditions. The DP FPSO with group configuration of six azimuth thrusters, as shown in Figure 2.13, was simulated. The thruster configuration and constraints are the same as the previous GOM 100-year group configuration case.

Trajectories by three different allocation methods are presented in Figure 2.24. The watch circle is under 3m because the environmental force is much smaller compared to the GOM 100-year conditions. The corresponding statistics are summarized in Table 2.12. In this milder environment, there is no appreciable difference in position-keeping performance among the three different methods.

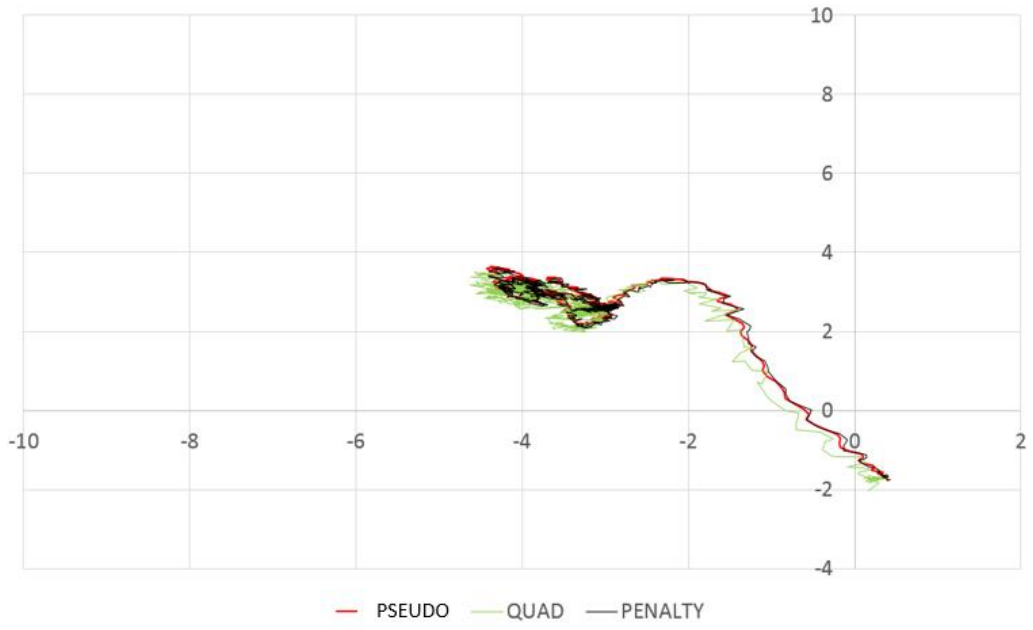

Figure 2.24 Surge and Sway Trajectories by Three Different Thrust Allocation Algorithms

Table 2.12 Mean Value and Standard Deviation by Three Different Thrust Allocation Algorithms

	Surge Mean (M)	Surge STD	Surge Max	Sway MEAN(M)	Sway STD	Sway MAX	Yaw MEAN (M)	Yaw STD	Yaw MAX	TOP TENSION MAX
PENALTY	-3.15	1.07	-4.39	2.56	1.06	3.59	8.38	3.70	14.19	4386KN
PSEUDO	-3.2	1.07	-4.43	2.62	1.06	3.64	8.41	3.71	14.21	4387KN
QUAD	-3.30	1.08	-4.58	2.49	1.06	3.58	8.50	3.74	14.40	4387KN

Figure 2.25 shows 6DOF motion results of DP controlled FPSO with the penalty method. In general, motion amplitudes are much smaller than those in the case of the 100-year storm.

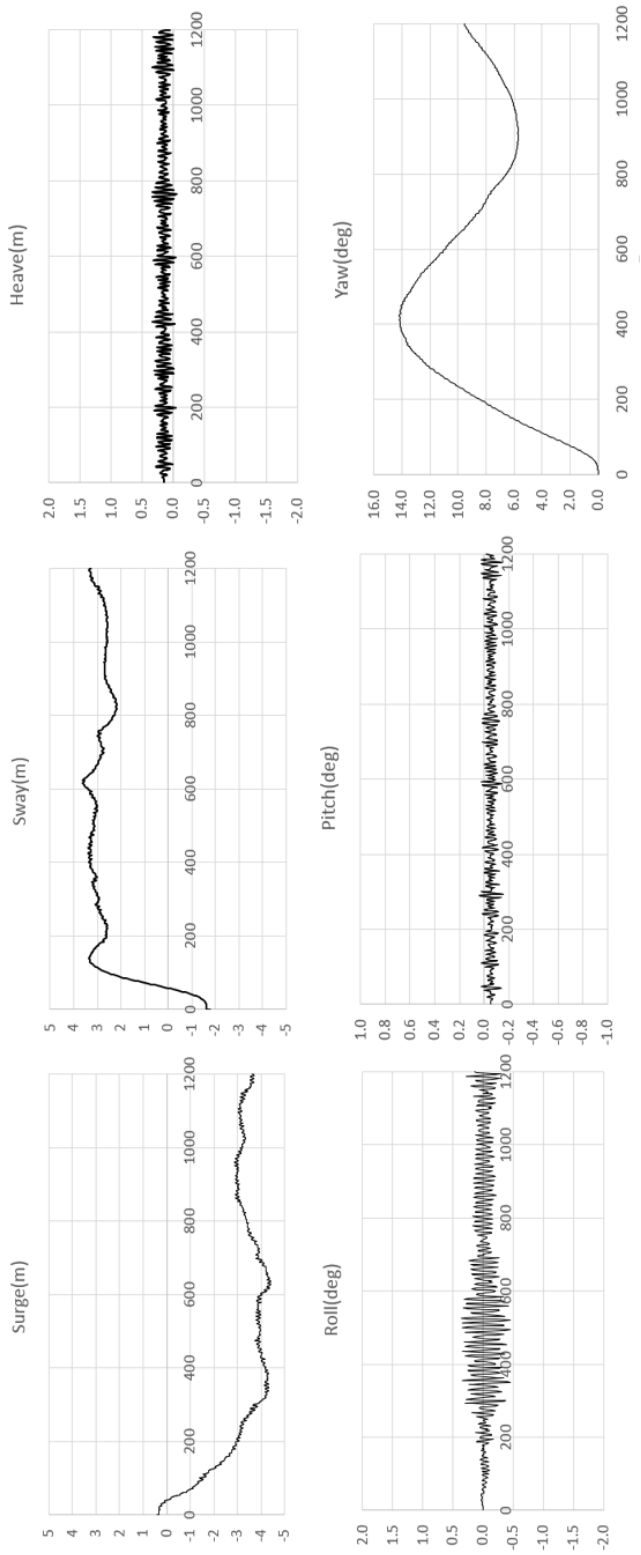

Figure 2.25 6DOF Motions under Gulf of Mexico One-Year Conditions

Figure 2.26 shows fuel consumption amounts based on the pseudo-inverse, penalty, and quadratic programming methods. The peak of the penalty method is lower than those of pseudo-inverse and quadratic methods by a maximum of 13% and 9%, respectively. In the case of the accumulated fuel consumption amount, the penalty method saves 3% and 2% in total accumulated fuel consumption compared to the pseudo-inverse and quadratic-programming methods.

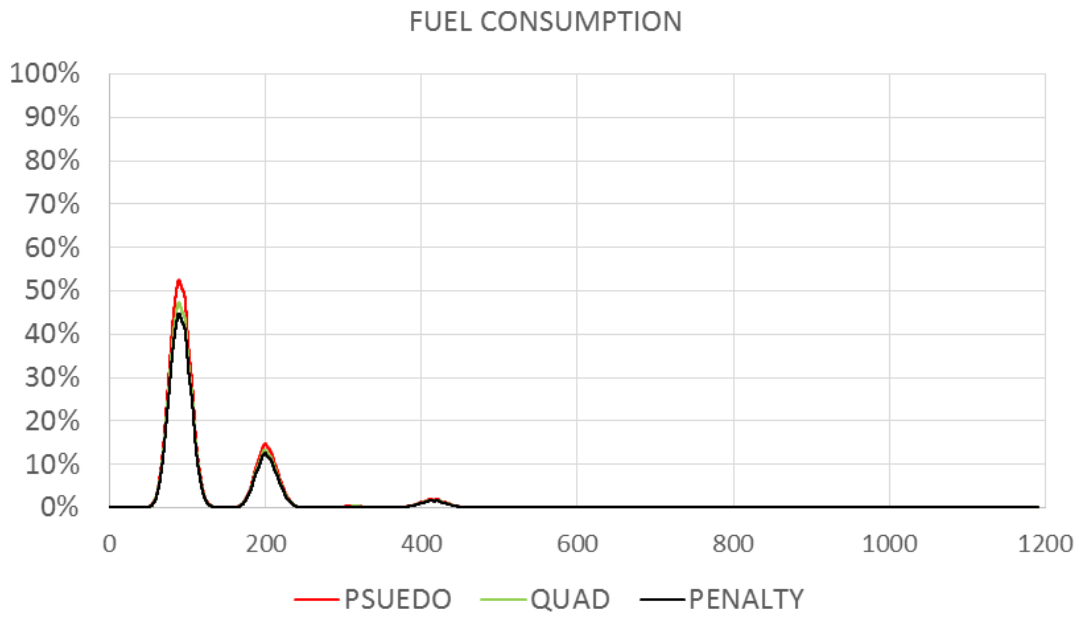

Figure 2.26 Fuel Consumption Index Time History by Three Different Thrust Allocation Algorithms

Figure 2.27 shows the CO_2 amounts produced during the dynamic positioning operation. The penalty method performed better than the pseudo-inverse and quadratic programming methods. The peak of the penalty method is lower than those of the pseudo-inverse and quadratic programming methods by a maximum of 9% and 7%, respectively.

In the case of the accumulated CO_2 emissions amount, the penalty method produced 2% less CO_2 compared to the pseudo-inverse and quadratic programming methods.

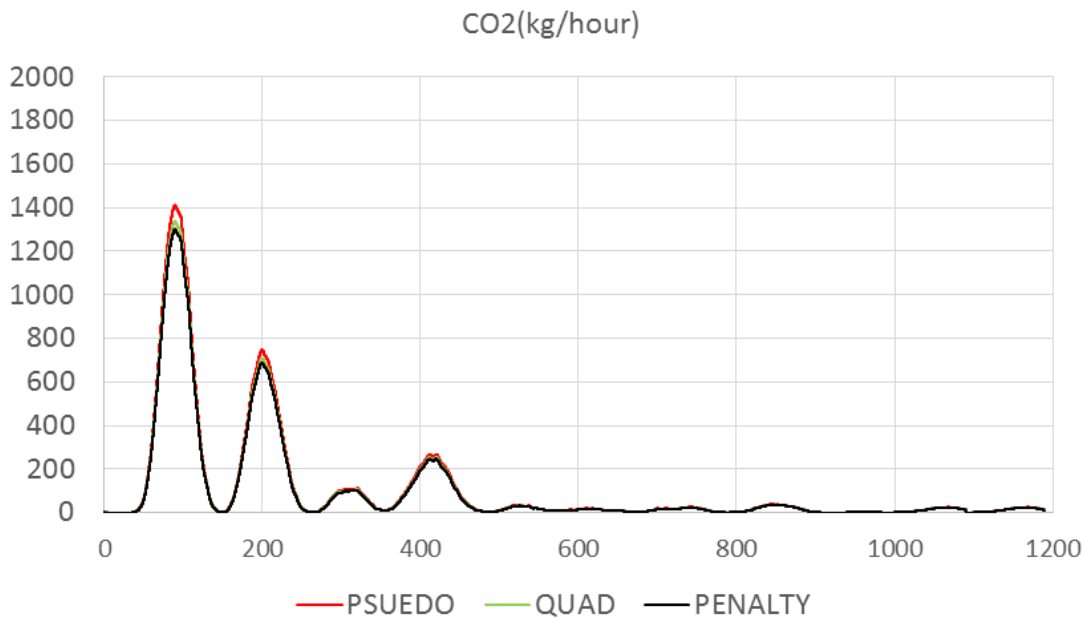

Figure 2.27 CO2 Index Time History by Three Different Thrust Allocation Algorithms

2.5 Conclusions

In this research, a new thrust allocation algorithm, called the penalty method, is proposed for optimal DP operation with minimal fuel consumption and CO_2 emissions, while also maintaining good performance in vessel position-keeping. Its performance was compared with other, existing thruster-allocation methods, such as the pseudo-inverse and quadratic programming methods. To demonstrate the performance of the respective thruster-allocation methods, a DP-controlled, turret-moored FPSO was considered. The thrust-allocation methods were implemented in the time-domain hull-motion with DP

control simulation program. The time-domain simulation tool was validated by comparison with its reference cases.

The effects of environmental conditions and thruster arrangements were analyzed in time-domain simulations. The developed penalty method shows the best performance in the reduction of fuel consumption and gas emissions, compared to the conventional pseudo-inverse and quadratic programming methods in all cases. In the case of the genetic algorithm, despite high performance, it is not feasible for a real-time DP controller because the computation time per unit thrust allocation is typically longer than one minute. In the case of thruster configuration, the group thruster configuration shows better performance compared to the single alignment configuration.

Application of the newly developed penalty method in thrust allocation can save about 7% (or 6%) in accumulated fuel consumption and 5% (or 4%) in CO_2 emissions as compared to the pseudo-inverse (or quadratic-programming) methods in GOM 100-year conditions. Similarly, the penalty method can reduce accumulated fuel consumption and CO_2 emissions by about 3% (or 2%) when compared to pseudo-inverse (or quadratic programming) methods in GOM one-year storm conditions.

CHAPTER III

FEED-FORWARD CONTROL FOR DP FPSO

3.1 Introduction

Conceptually, feed-forward control is a control method that generates counter-acting forces and moments to environmental loads such as wind, waves, and current. The strength of feed-forward control is the quicker production of the control force compared to feedback control, so the DP controller can react in the initial movement stage. The inertia of the offshore platform and vessel is significant, and movement makes controlling the position of the offshore platform very difficult. Therefore, feed-forward control can enhance fuel consumption performance by minimizing position deviation.

Practically, feedback control has been widely employed in conventional DPS because it is very robust under unexpected environmental disturbances. Another example of its versatility is that its gain tuning is intuitive to DP operators (Sørensen, 2011). Furthermore, knowledge of environmental load mathematical modeling has accumulated as the application of feed-forward has expanded. Currently, most DP controller usage adopts a feed-forward and feedback control together. The feedback and feed-forward controls mutually compensate for the weaknesses found in each. The feed-forward control makes pre-emptive control possible before the set-time error can occur. Feedback control improves the robustness of the controller.

The major environmental loads affecting the offshore platform are wind, current, and wave forces. Generally, wind, current forces and moment can be presented as equation (3.1):

$$Wind, Curret\ Load = \frac{1}{2}\rho S V^2 C_D \tag{3.1}$$

where,

ρ: density (air/water)

S: projection area

V: speed(wind/current)

C_D: coefficient(wind/current)

The key in estimating wind current force is the measurement of the coefficient and the speed of the wind and current. The measurement methods for the wind and current coefficient and speed are well established in comparison with wave elevation measurement technology. Wind and current resistance are also very important to commercial vessels such as tankers, container ships, and naval ships, because resistance is the main source of reduction in the vessel's speed. Therefore, the estimation of wind and current has been researched thoroughly in the field of naval architecture. Generally, the wind and current coefficient are determined by the shape of the offshore platform and vessel, and the wind tunnel test and Computational Fluid Dynamics (CFD) are widely used for this calculation. Wind tunnel testing has enormous databases. The Isherwood (1973) and OCIMF (1996)methods are widely used to estimate wind and current coefficients. CFD has an advantage for use estimating the wind coefficient of a newly built offshore platform because it is easy to study the large number of design matrixes.

The speed of wind and current are directly measured by the anemometer and the current speed meter that are installed in offshore platforms; they are basic equipment, making these measurements convenient Therefore, the wind and current feed-forward control were implemented faster than the wave feed-forward control (J.Sorensen, 1999).

Wave load force can be divided into two categories: first-order and second-order. The first-order wave force makes large, oscillatory, zero-mean motions. Physically, hydrostatic restoring forces, added mass, and damping effects are associated with the radiation of free surface waves. First-order waves are difficult to address using DP, because their scale is so large compared to the total sum of thruster force that the thruster would need to equip high-thrust to withstand them. Additionally, the frequency of the first-order force is too high to attenuate by thruster reaction. Finally, the total sum of the first order force drift motion is zero, so the offshore platform would assume its original position again naturally.

Second-order forces are proportional to the square of wave amplitude and are non-zero mean. They typically are smaller than first-order wave loads, small enough to be controlled by the platform's thrusters. Physically, natural damping is not effective in reducing this force, so the DPS is essential to lessen this load. The second-order force is the target force for feed-forward control, because it is controllable.

This dissertation first seeks to apply the direct integration method based on the second-order impulse response function technique for the FPSO. This technique is powerful for application of the practical DP because the wave elevation time history is the only information necessary for the calculation.

The performance of the feed-forward application will be analyzed in this chapter by using the time-domain coupled simulation analysis. The GOM one-year and GOM 100-year conditions will be tested in the simulation to evaluate the feed-forward control performance in terms of position deviation, fuel consumption, and gas emissions

.

3.2 Literature Review

The first application of wave feed-forward DP control was demonstrated in a model test by Pinkster (1978), who used the water line integral method for the dynamic positioning control using second-order drift force. Pinkster (1981) also compared the difference of the second-order wave drift force between the direct integration method and the indirect integration method.

Several ways of estimating drift force were proposed. Initially, it was assumed that drift force is proportional to the square of the wave height elevation. P.Sincock (1989) applied the second-order Volterra series model to parameterize the response of a nonlinear system by using a quadratic impulse response function. It mathematically convolved the input at different time lag in the frequency domain by using the quadratic transfer function (QTF) that shows how different frequencies in the input interact to produce a response in the sum and difference of the frequencies, but this approach did not consider real-time implementation.

Aalbers, Tap, and Pinkster (2001), Waals, Aalbers, and Pinkster (2002), Quadvlieg, Hallmann, Hughes, and Harris (2011) applied wave feed-forward control by using second-

order drift force estimation based the Quadratic Transfer Function(QTF) method by the water integral with the wave measurement probe.

3.3 Aims and Contribution

This chapter seeks to analyze performance change in positioning, fuel consumption, and gas emissions resulting from application of the feed-forward control method. For feed-forward control implementation in the DP algorithm, the feed-forward control will be mathematically modeled. Also, the second-order drift force direct integration through real-time wave elevation measurement will be tested for DP control.

3.4 Mathematical Modeling

3.4.1 Equation of Motion

The equation of motion of an offshore platform can be presented as in Equation (3.2):

$$[\boldsymbol{M} + \boldsymbol{M^a}(\infty)]\ddot{\boldsymbol{\varsigma}} + \boldsymbol{K\varsigma} = \boldsymbol{F_I}(t) + \boldsymbol{F_c}(t, \dot{\boldsymbol{\varsigma}}) + \boldsymbol{F_n}(t, \boldsymbol{\varsigma}) \quad (3.2)$$

where,

$\boldsymbol{F_c}(t, \dot{\boldsymbol{\varsigma}}) = -\int_{-\infty}^{t} R(t-\tau)\,\dot{\varsigma} d\tau$

$\boldsymbol{F_I}(t)$ = the first-and second-order wave exciting forces defined in equations

$\boldsymbol{F_n}(t, \boldsymbol{\varsigma})$ = the nonlinear drag forces from Morison's formula

The Adams-Moulton method has second-order precision. The reason for using this method is to apply the Finite Element Analysis (FEA) to mooring-line, platform-coupled analysis. To apply the Adams-Moulton method, the motion equation should be reduced to the following two differential equations:

$$\bar{\boldsymbol{M}}\dot{\boldsymbol{\xi}} = \boldsymbol{F_I}(t) + \boldsymbol{F_c}(t, \dot{\boldsymbol{\varsigma}}) + \boldsymbol{F_n}(t, \boldsymbol{\varsigma}) - \boldsymbol{K\varsigma} \tag{3.3}$$

$$\dot{\boldsymbol{\varsigma}} = \boldsymbol{\xi}$$

Where, $\bar{\boldsymbol{M}} = \boldsymbol{M} + \boldsymbol{M^a}(\infty)$

After integrating the above equations from time step $t^{(n)}$ to $t^{(n+1)}$;

$$\bar{\boldsymbol{M}}\boldsymbol{\xi}^{(\boldsymbol{n+1})} - \bar{\boldsymbol{M}}\boldsymbol{\xi}^{(\boldsymbol{n})} = \int_{t^{(n)}}^{t^{(n+1)}} \left(\boldsymbol{F_I}(t) + \boldsymbol{F_c}(t, \dot{\boldsymbol{\varsigma}}) + \boldsymbol{F_n}(t, \boldsymbol{\varsigma})\right) dt - \int_{t^{(n)}}^{t^{(n+1)}} \boldsymbol{K\varsigma}\, dt \tag{3.4}$$

$$\boldsymbol{\varsigma}^{(n+1)} - \boldsymbol{\varsigma}^{(n)} = \int_{t^{(n)}}^{t^{(n+1)}} \boldsymbol{\xi}\, dt$$

Applying the Adams-Moulton scheme: $\int_{t^{(n)}}^{t^{(n+1)}} x\, dt = \frac{\Delta t}{2}\left[x^{(n)} + x^{(n+1)}\right]$

$$\bar{\boldsymbol{M}}\boldsymbol{\xi}^{(\boldsymbol{n+1})} = \bar{\boldsymbol{M}}\boldsymbol{\xi}^{(\boldsymbol{n})} + \frac{\Delta t}{2}\left(\boldsymbol{F_I}^{(n+1)} + \boldsymbol{F_I}^{(n)} + \boldsymbol{F_c}^{(n+1)} + \boldsymbol{F_c}^{(n)} + \boldsymbol{F_n}^{(n+1)} + \boldsymbol{F_n}^{(n)}\right) -$$

$$\frac{\Delta t}{2}\boldsymbol{K}\left(\boldsymbol{\varsigma}^{(n+1)} + \boldsymbol{\varsigma}^{(n)}\right) \tag{3.5}$$

$$\boldsymbol{\varsigma}^{(n+1)} - \boldsymbol{\varsigma}^{(n)} = \frac{\Delta t}{2}\left(\boldsymbol{\xi}^{(n+1)} + \boldsymbol{\xi}^{(n)}\right) \rightarrow \quad \boldsymbol{\xi}^{(n+1)} = \frac{2}{\Delta t}\left(\boldsymbol{\varsigma}^{(n+1)} - \boldsymbol{\varsigma}^{(n)}\right) - \boldsymbol{\xi}^{(n)}$$

The above equations are linear algebraic equations with unknown variables $\boldsymbol{\xi}^{(\boldsymbol{n+1})}$ and $\boldsymbol{\varsigma}^{(n+1)}$. The convolution integral and drag force are functions of the unknown velocity of the platform at time step $(n+1)$. Therefore, for solving this equation, an iterative process is necessary with an initial assumption of the $\boldsymbol{\xi}^{(\boldsymbol{n+1})}$ in computing the $\boldsymbol{F_c}^{(n+1)}$ and $\boldsymbol{F_n}^{(n+1)}$. In this study, the iterative procedure is avoided by using the Adams-Bashforth scheme with the following nonlinear force terms:

$$\int_{t^{(n)}}^{t^{(n+1)}} \boldsymbol{F_c}\, dt = \frac{\Delta t}{2}\left(3\boldsymbol{F_c}^{(n)} - \boldsymbol{F_c}^{(n-1)}\right) \text{ and } = \Delta t \boldsymbol{F_c}^{(0)} \text{ for } n = 0 \tag{3.6}$$

$\int_{t^{(n)}}^{t^{(n+1)}} \boldsymbol{F_n}\, dt = \frac{\Delta t}{2}\left(3\boldsymbol{F}_n^{(n)} - \boldsymbol{F}_n^{(n-1)}\right)$ and = $\Delta t \boldsymbol{F}_n^{(0)}$ for $n = 0$

3.4.2 Controller Design

The feedback and feed-forward control were combined in the DP controller design. Feedback and feed-forward control can indemnify mutual shortages. Feed-forward could compensate for drawbacks such as slow reactions that postpone control until error accumulation. Also, feedback control compensates for the robustness of feed-forward control, because feed-forward control essentially is based on the mathematical modeling of external disturbance, but mathematical modeling cannot be perfect in describing the physical environment. It is natural to have an unexpected external disturbance. Feed-forward control is very weak and can lose stability under these environmental conditions.

$$F_{control} = C_1 F_{feedback} + C_2 F_{feedforward} \tag{3.7}$$

where, $F_{control}$ is total control force, $F_{feedback}$ is feedback control force, $F_{feedforward}$ is feed-forward control force, and C_1 and C_2 are the weight constant for feed-forward control. In this dissertation, those are 0.5

For the calculation of feedback control force, the system equation is necessary. The time invariant linear system state was considered as seen in Equation (3.8):

$$\dot{\mathbf{x}} = \mathbf{A}\mathbf{x} + \mathbf{B}\mathbf{u}$$
$$\mathbf{y} = \mathbf{C}\mathbf{x} + \mathbf{v} \tag{3.8}$$

where, dot (·) denotes time derivative, and each vector written in lowercase can be described by the following set of definitions:

State $\mathbf{x} = [u, x, v, y, \omega, \psi]^T$

Control Input $u = [F_{FB\_x} + F_{FF\_x}, F_{FB\_y} + F_{FF\_y}, F_{FB\_N} + F_{FF\_N}]^T$

Measurement $\mathbf{y} = [x, y, \psi]^T$

Measurement-Noise $\mathbf{v} = [v_x, v_y, v_\psi]^T$

$$u = C_1 FB + C_2 FF$$
$$= -C_1 Ke - C_2(wind\ load + current\ load + wave\ load) \tag{3.9}$$

where, error matrix $e = \hat{x} - x_{target}$, u is the thruster commands matrix , $\hat{x}$ is the state estimation matrix, and x_{target} is the target state matrix. C_1 and C_2 are the weight constant for feed-forward control. In this dissertation, those are 0.5.

where the PD gain matrix K is

$$\mathbf{K} = \begin{bmatrix} D_x & P_x & 0 & 0 & 0 & 0 \\ 0 & 0 & D_y & P_y & 0 & 0 \\ 0 & 0 & 0 & 0 & D_\psi & P_\psi \end{bmatrix} \tag{3.10}$$

For feedback control gain (K) gain decision, and calculating PID gains, the linear quadratic regulator (LQR) was employed. The LQR is conventionally used for finding

optimal control gain matrix K that can minimize state error and thruster usage together, as seen in Equation (3.11)(Ryu, 2005).

$$\mathbf{K} = \mathbf{R}_o^{-1}\mathbf{B}^T\mathbf{P} \tag{3.11}$$

Then P should be defined to decide K. P is the solution of the following the Ricatti equation (3.12):

$$\mathbf{A}^T\mathbf{P} + \mathbf{P}\mathbf{A} - \mathbf{P}\mathbf{B}\mathbf{R}_o^{-1}\mathbf{B}^T\mathbf{P} + \mathbf{Q}_o = 0 \tag{3.12}$$

This equation satisfies the performance index that minimizes state and input together.

$$J = \int_0^\infty \left\{ \mathbf{e}(t)^T \mathbf{Q}_o \mathbf{e}(t) + \mathbf{u}(t)^T \mathbf{R}_o \mathbf{u}(t) \right\} dt \tag{3.13}$$

where e is error matrix, Q_0, R_0 are the initial weight matrixes.

For feed-forward controller design, environmental loads modeling is essential. Environmental loads are composed of wind, waves, and current, which will be modeled and implemented in the following section.

3.4.3 Wind and Current Loads

Wind and current loads in the horizontal plane can be formulated using the following (Isherwood, 1973):

$$F_{wind} = \begin{bmatrix} X_{wind} \\ Y_{wind} \\ N_{wind} \end{bmatrix} = \begin{bmatrix} 0.5 C_{wind-X}(\psi_{wind}) \rho_{air} A_{transverse} V_{wind}^{\ 2} \\ 0.5 C_{wind-Y}(\psi_{wind}) \rho_{air} A_{lateral} V_{wind}^{\ 2} \\ 0.5 C_{wind-N}(\psi_{wind}) \rho_{air} A_{lateral} L_{pp} V_{wind}^{\ 2} \end{bmatrix} \tag{3.14}$$

$$F_{current} = \begin{bmatrix} X_{current} \\ Y_{current} \\ N_{current} \end{bmatrix} = \begin{bmatrix} 0.5 C_{current-X}(\psi_{current}) \rho_{water} A_{transverse} V_{current}^{\ 2} \\ 0.5 C_{current-Y}(\psi_{current}) \rho_{water} A_{lateral} V_{current}^{\ 2} \\ 0.5 C_{current-N}(\psi_{current}) \rho_{water} A_{lateral} L_{pp} V_{current}^{\ 2} \end{bmatrix} \quad (3.15)$$

The wind coefficients C_{wind-X}, C_{wind-Y}, and C_{wind-N} the current coefficients $C_{current-X}, C_{current-Y}$ and $C_{current-N}$ are the function of wind and current incident angle to the offshore platform. Those coefficients generally are obtained in a wind tunnel test. In this study, the wind tunnel test value was used. The typical wind and current coefficient is seen in Figure 3.1.

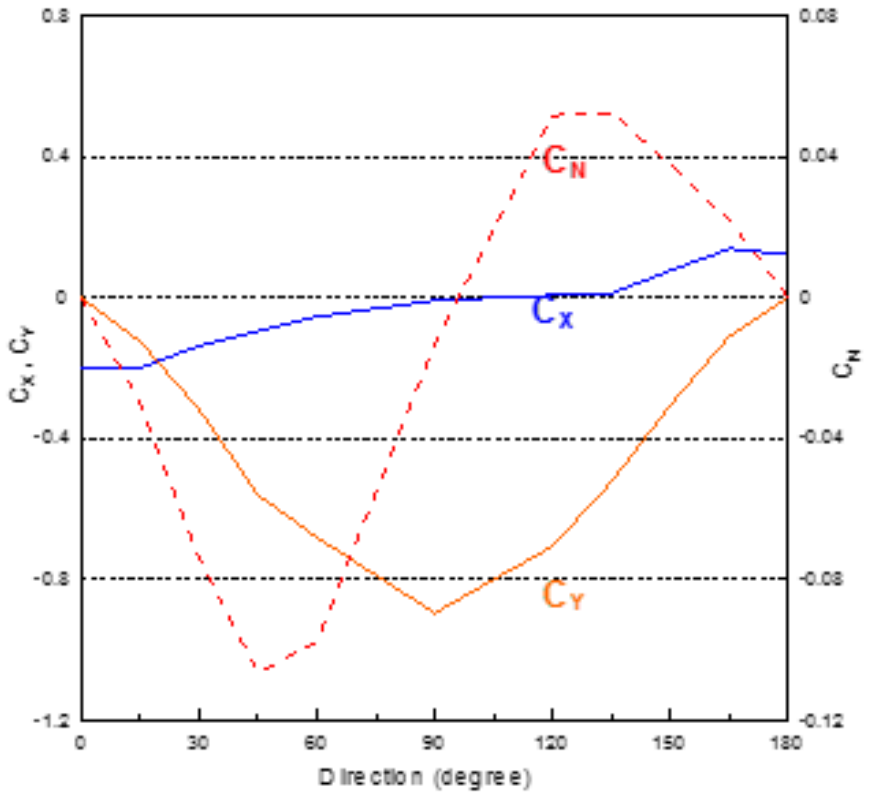

Figure 3.1 Wind Coefficients

3.4.4 Wave Load Estimation

Wave load modeling is the central part of feed-forward control. Wave load real-time estimation could be modeled as in the Volterra time series form as seen in Equation 3.16:

$$\begin{aligned} F_{wave} &= 1st\ order\ waver\ \ force + 2nd\ order\ wave\ force \\ &= F^{(1)}(t) + F^{(2)}(t) \\ &= \int_{-\infty}^{\infty} h(\tau)\eta\left(t-\tau\right)d\tau + \int_{-\infty}^{\infty}\int_{-\infty}^{\infty} h\left(\tau_1,\tau_2\right)\eta(\mathrm{t}-\tau_1)\eta(\mathrm{t}-\tau_2)\,\mathrm{d}\,\tau_1\,\mathrm{d}\,\tau_1 \end{aligned} \tag{3.16}$$

where

t : present time
τ : *time to calculate memory effect*
$h\left(\tau\right)$: *1st order impulse function*
$h(\tau_1,\tau_2)$: *2nd order impulse function*

Second-order force is the double convolved form of the quadratic impulse function, wave elevation in τ_1,τ_2 domain. There are two ways to calculate the second-order force in time domain. One is direct integration that calculates the second-order force by using the quadratic impulse function $h\left(\tau_1,\tau_2\right)$ and wave elevation time series, $\eta\left(t\right)$. The other is indirect integration that uses the frequency domain QTF. The indirect method is the conventional way to calculate the second-order force for the time domain motion analysis program such as CHARM 3D. The way of the indirect method can be summarized by Equation 3.5. The indirect method calculates the second-order wave force using the summation of the multiplication of wave amplitude, QTF, and phase of difference

frequency from the incident wave potential and diffraction potential. The QTF generally is calculated by using the frequency domain motion simulation program.

$$F^{(2)}(t) = Re\left[\sum_{i=1}^{N}\sum A_i A_j D\left(\omega_i - \omega_j\right) e^{i\left(\omega_i - \omega_j\right)t + \left(\varepsilon_i - \varepsilon_j\right)}\right] \tag{3.17}$$

where,

D: Difference Frequency Quadratic Transfer Function in Frequency Domain

ω_i, ω_j : Wave Frequency (rad/sec)

A_i,A_j : Wave Amplitudes of Different Frequencies

ε_i, ε_j: Wave Amplitudes of Different Frequencies

While this indirect method is well established and its accuracy proven, it also has disadvantages when applied to feed-forward control. When using the indirect method in the second-force calculation, random phase information is necessary, but this cannot be measured in an irregular sea. The only information that can be measured in the real system is the wave elevation time series. Therefore, the direct integration method can be the alternative way to calculate second-order force for the feed-forward DP control. This dissertation first tries to apply this direct integration method for real-time, feed-forward DP control.

The direct integration method of the second-order wave force requires two datum: the quadratic impulse response function in the time domain, and wave elevation time history. The quadratic impulse function can be obtained from the QTF in the frequency

domain. The quadratic impulse response function $h(\tau_1,\tau_2)$ is the double inverse Fourier transform of the Quadratic Transfer Function (QTF) in frequency domain, so the quadratic impulse function and the QTF has following relation (P.Sincock, 1989):

$$h(\tau_1,\tau_2)=\frac{1}{(2\pi)^2}\int_{-\infty}^{+\infty}\int_{-\infty}^{+\infty} QTF(\omega_1,\omega_2)\exp\left(i(\omega_1\tau_1+\omega_2\tau_2)\right)d\tau_1 d\tau_2 \tag{3.18}$$

For a more realistic calculation, the Nyquist Frequency could be considered

$$h(\tau_1,\tau_2)=\frac{1}{(2\pi)^2}\int_{-\omega_N}^{\omega_N}\int_{-\omega_N}^{\omega_N} QTF(\omega_1,\omega_2)\exp\left(i(\omega_1\tau_1+\omega_2\tau_2)\right)d\tau_1 d\tau_2 \tag{3.19}$$

where

$$\omega_N=\frac{2\pi}{\Delta t}$$

Δt : *time step in the time domain simulation*

Figure 3.2 shows the surge quadratic impulse response function $h(\tau_1,\tau_2)$ in a bi-time domain. In this dissertation, the wave loads originate in the head sea, so only the surge second-order wave load was considered.

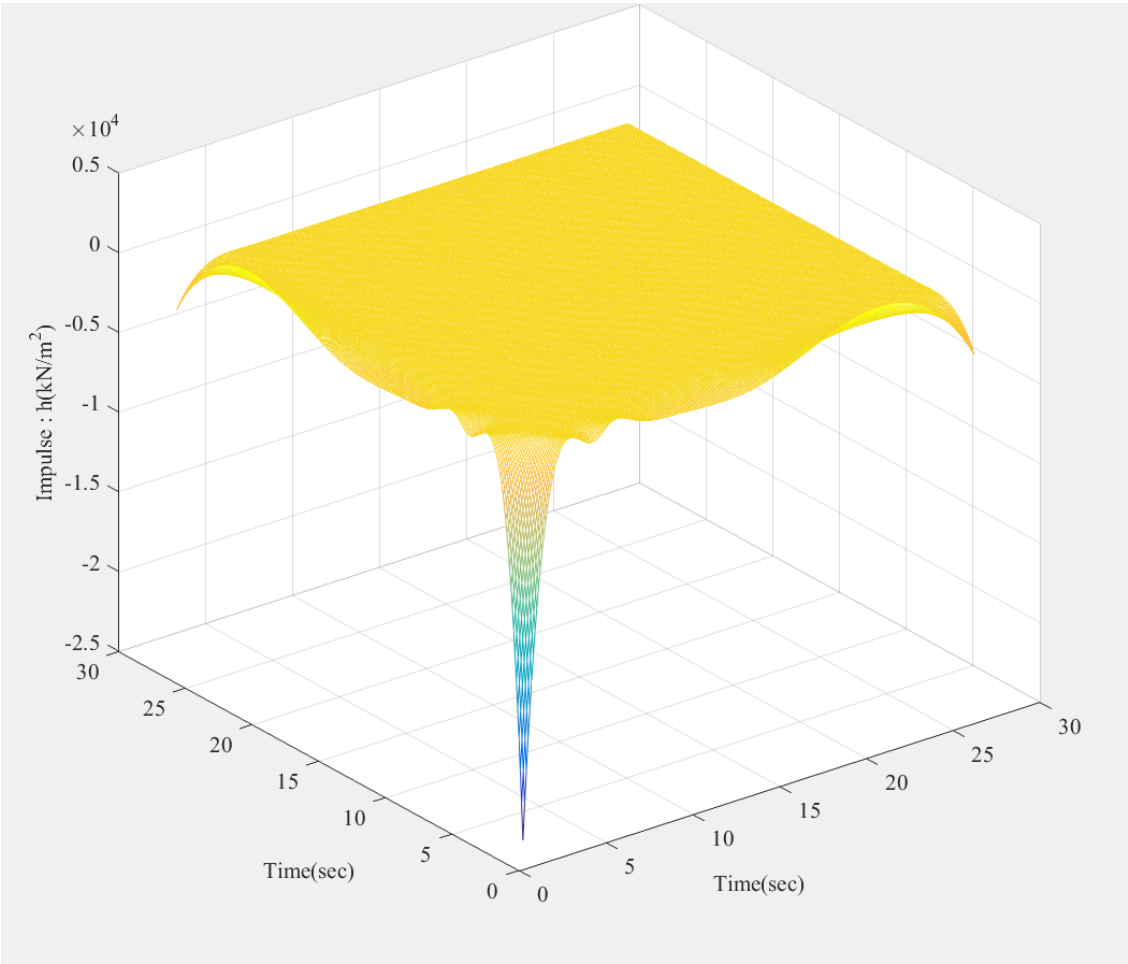

Figure 3.2 Quadratic Impulse Function in Bi-Time Axis

Figure 3.3 illustrates the contour line of the surge quadratic impulse response function.

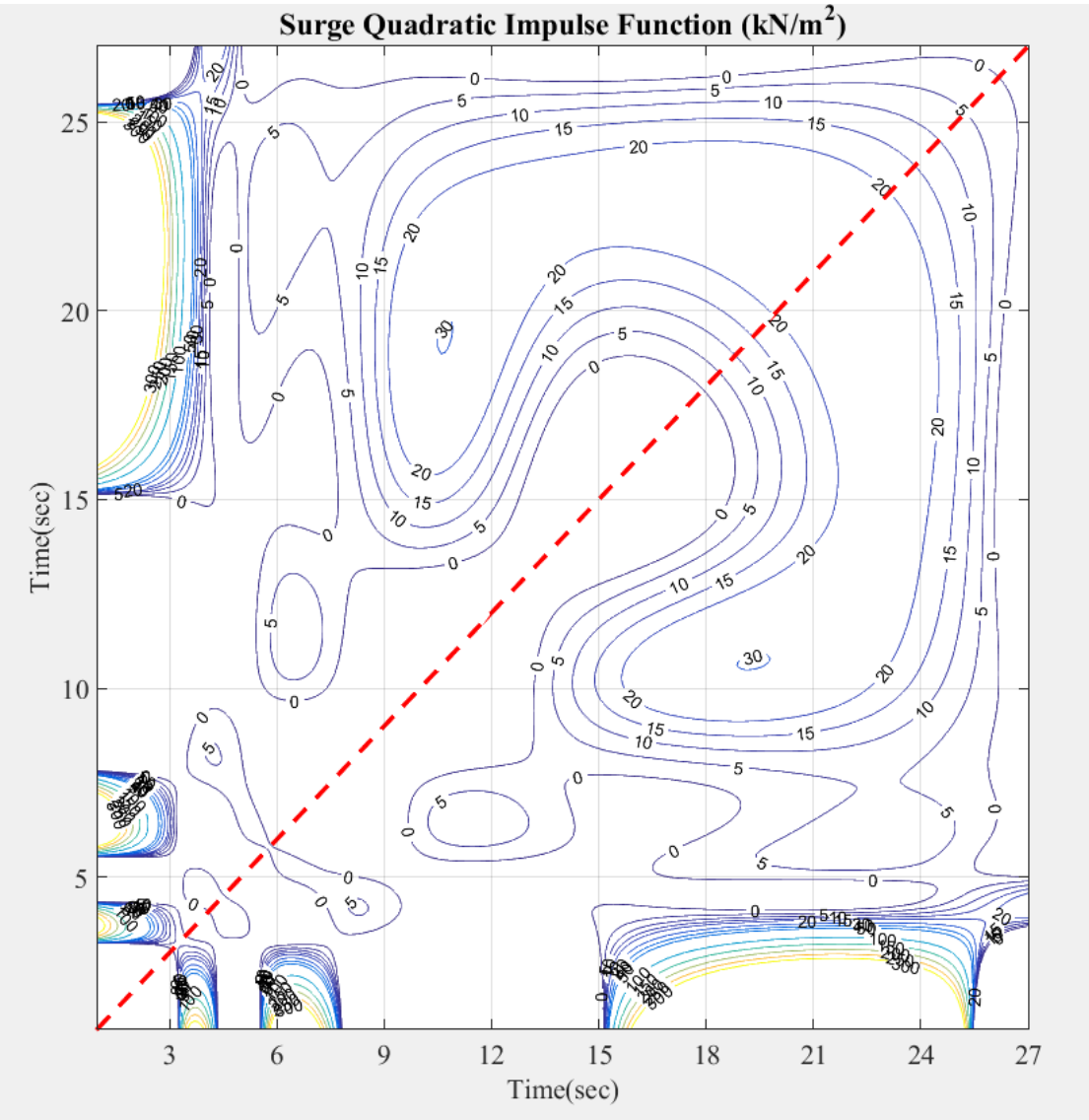

Figure 3.3 Quadratic Impulse Response Function in 2D

For the real-time, second-order wave force calculation, the wave elevation time history $\eta(t)$ will be measured and stored in the DP control algorithm. While the measurement technology is not included in this dissertation, it is assumed that it is possible to measure from the floating buoy near the DP vessel. In reality, wave elevation

measurement has been developed in various ways, such as the radar measuring technique, the buoy method, and inverse filtering using the Gyro and RAO of the offshore platform.

Figure 3.4 is the wave elevation time history under the GOM 100-year storm conditions. The following data were used for the wave elevation calculation: $\eta(\tau_1), \eta(\tau_2)$.

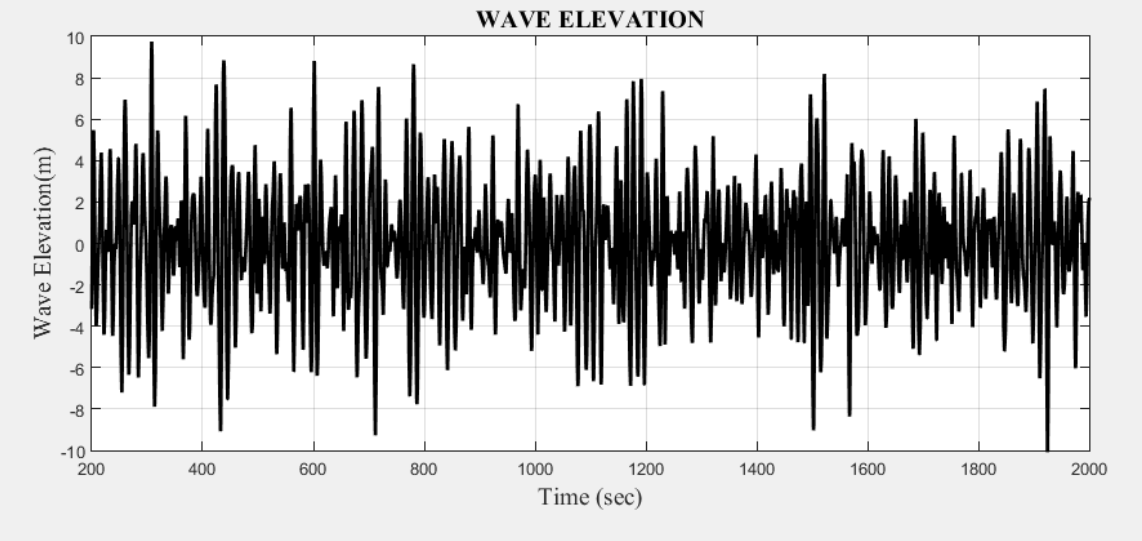

Figure 3.4 Wave Elevation Time History

Figure 3.5 compares the direct and indirect calculation of the second-order drift force. The black line is the indirect method that used the QTF in the frequency domain, and the red dotted line is the direct method found in the time domain by using the quadratic impulse response function and wave elevation. The direct method is well matched with the trend of the indirect method. Therefore, the result of the second-order force by using the direct integration method has sufficient accuracy to apply the wave feed-forward control.

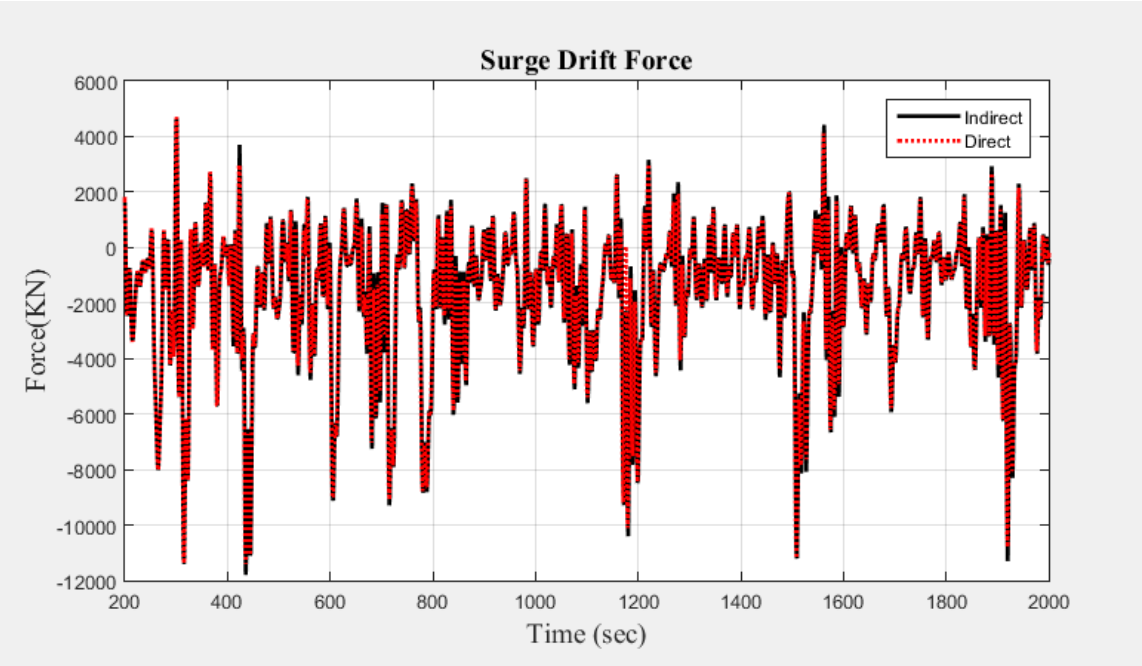

Figure 3.5 Surge Drift Force Estimation Using Indirect and Direct Methods

3.5 Optimization Modeling

In optimization modeling, the problem of optimizing fuel consumption and minimizing gas emissions was defined for thrust allocation. The optimization formulation is basically the same as used in Chapter II. Here, only the penalty method that showed the best thrust allocation performance in Chapter II was employed. The constraints for the optimization were changed to satisfy the required force and moment condition. The control force includes the feed-forward control force; thus, the required control force was changed.

Object to

minimize

$$\left(\frac{1}{2}x^T Hx+\frac{1}{2}u^T Ku+c\left(\begin{array}{l}\max\{0,\mathrm{u}-\mathrm{u}_{\max}\}^2+\max\{0,u_{\min}-u\}^2\\+\max\{0,\dfrac{u_{previous}-\mathrm{u}_{current}}{dt}-\dot{\mathrm{u}}_{\max}\}^2+\left(\tau-Bu\right)^2\end{array}\right)\right) \tag{3.18}$$

where, $x=(x,y,\phi,u,v,r)^T, u=(T_1\cos\alpha,T_1\sin\alpha,...,T_n\cos\alpha,T_n\sin\alpha)$, H is a state weight matrix, K is the fuel consumption parameter weight matrix, τ is the required force and moment matrix, B is the thrust allocation matrix, u is thruster matrix

Subject to

$$Required\ Force\ for\ Control=F_{Feedback}+F_{Feed-forward}$$
$$F_{Feedback\_X}+F_{Feed-forward\_X}=T_{x1}\cos\alpha_1+T_{x2}\cos\alpha_2+.....T_{xn}\cos\alpha_n$$
$$F_{Feedback\_\mathrm{Y}}+F_{Feed-forward\_\mathrm{Y}}=T_{y1}\sin\alpha_1+T_{y2}\sin\alpha_2+.....T_{yn}\sin\alpha_n$$
$$F_{Feedback\_\mathrm{N}}+F_{Feed-forward\_\mathrm{N}}=y_1T_{x1}\cos\alpha_1-x_1T_{y1}\sin\alpha_1+y_2T_{x2}\cos\alpha_2$$
$$-x_2T_{y2}\sin\alpha_2+....+y_nT_{xn}\cos\alpha_n-x_nT_{yn}\sin\alpha_n$$

where, T is thrust matrix.

1.*Thrust & Azimuth Angle Constraint* : $T_{\min}<T<T_{\max},\alpha_{\min}<\alpha<\alpha_{\max}$

2.*Thrust & Azimuth Angle Rate Constraint* : $\dot{T}_{\min}<\dot{T}<\dot{T}_{\max},\dot{\alpha}_{\max}<\dot{\alpha}<\dot{\alpha}_{\max}$

3.*Required Forces and Moment Constraint* :

$$X=T_{x1}\cos\alpha_1+T_{x2}\cos\alpha_2+.....T_{xn}\cos\alpha_n$$
$$Y=T_{y1}\sin\alpha_1+T_{y2}\sin\alpha_2+.....T_{yn}\sin\alpha_n$$
$$N=y_1T_{x1}\cos\alpha_1-x_1T_{y1}\sin\alpha_1+y_2T_{x2}\cos\alpha_2-x_2T_{y2}\sin\alpha_2+....+y_nT_{xn}\cos\alpha_n-x_nT_{yn}\sin\alpha_n$$

3.6 Simulation Results

3.6.1 Simulation Matrixes

Two environmental simulation conditions were considered: the GOM one-year and 100-year conditions described in Chapter II. The intention is to compare the results when the feed-forward control is hired and not hired. Therefore, all the results will be compared to those of feedback control only.

Table 3.1 Simulation Condition: The Environment

		GOM 1-Year Storm	GOM 100-Year Storm
Wave	Significant Wave Height H_s	4.3m	12.19m
	Peak Period T_p	9sec	14sec
	Overshoot Parameter γ	2	2.5
Wind		14.3m/sec at 10m	41.1m/sec at 10m
Current		0.33m/sec	1.07 m/sec

A noncollinear environmental condition was used: waves from the head sea, wind from 210 degrees, and current from 150 degrees, respectively, as also used in Chapter II. A JONSWAP spectrum and the API wind spectrum were considered in the simulation. In the current load case, the vertical current profile was considered in the program: the FPSO-equipped internal turret, 12-chain polyester-chain moorings and 13 steel catenary risers. The moorings and risers were identical to those in table 2.5 and 2.6.

Six azimuth thrusts were installed in the simulation, with group configuration. Three thrusters were located in the bow, and the other three in the stern. Figure 3.6 shows the thruster configuration and location in the FPSO.

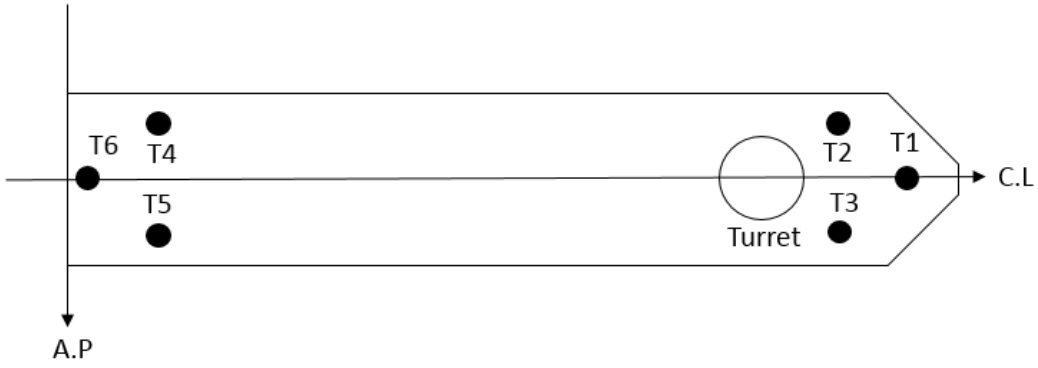

Figure 3.6 Thruster Configuration for Feed-Forward Control

Table 3.2 Thruster Details of Group Configuration

Thruster Maximum Capacity	150kn
Thruster Maximum Change Rate	20kn/sec
Thruster Angle Change Rate	10deg/sec
Thruster Position (A.P=0, C.L=0)	T1(290m,0m), T2(275m,-15m), T3(275m,15m) T4(35m,-15m) T5(35m,15m) T6(20m,0m)

3.6.2 Gulf of Mexico 100-Year Simulation

Figure 3.7 shows the horizontal motion of the feedback control and feed-forward control. The black line is the feedback control and the red line is the feed-forward control. In the case of the surge value, the feed-forward control reduced the surge position excursion from 23 meters to 17 meters. Attenuation of 26% by feed-forward compared to the feedback control was achieved.

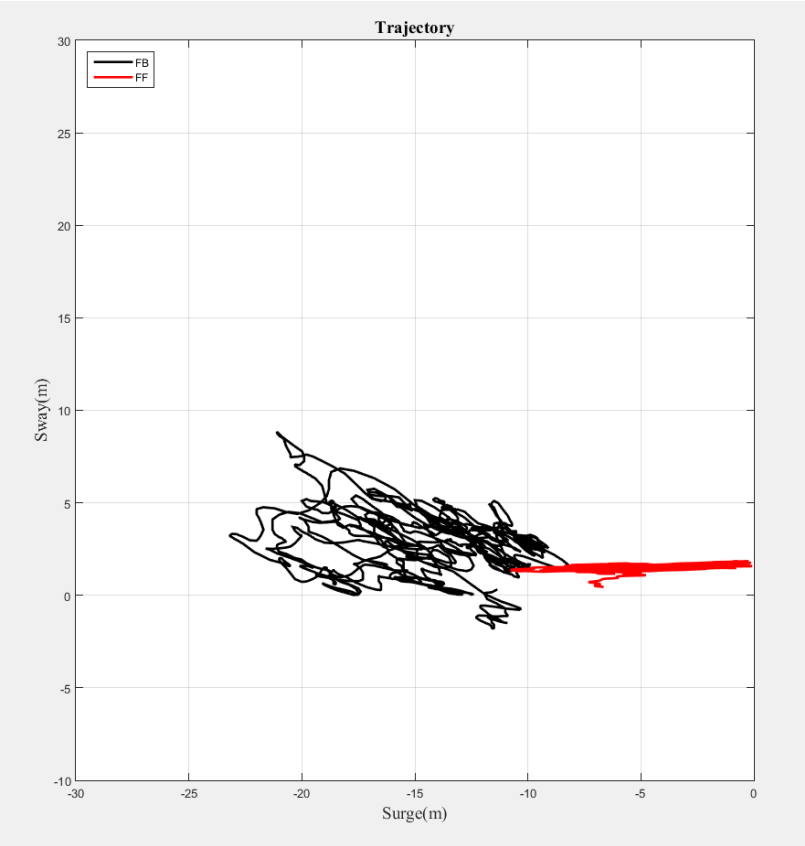

Figure 3.7 100-Year Position Difference (Surge-Sway)

Figure 3.8 shows the 6DOF motion time history of the feedback and feed-forward control case.

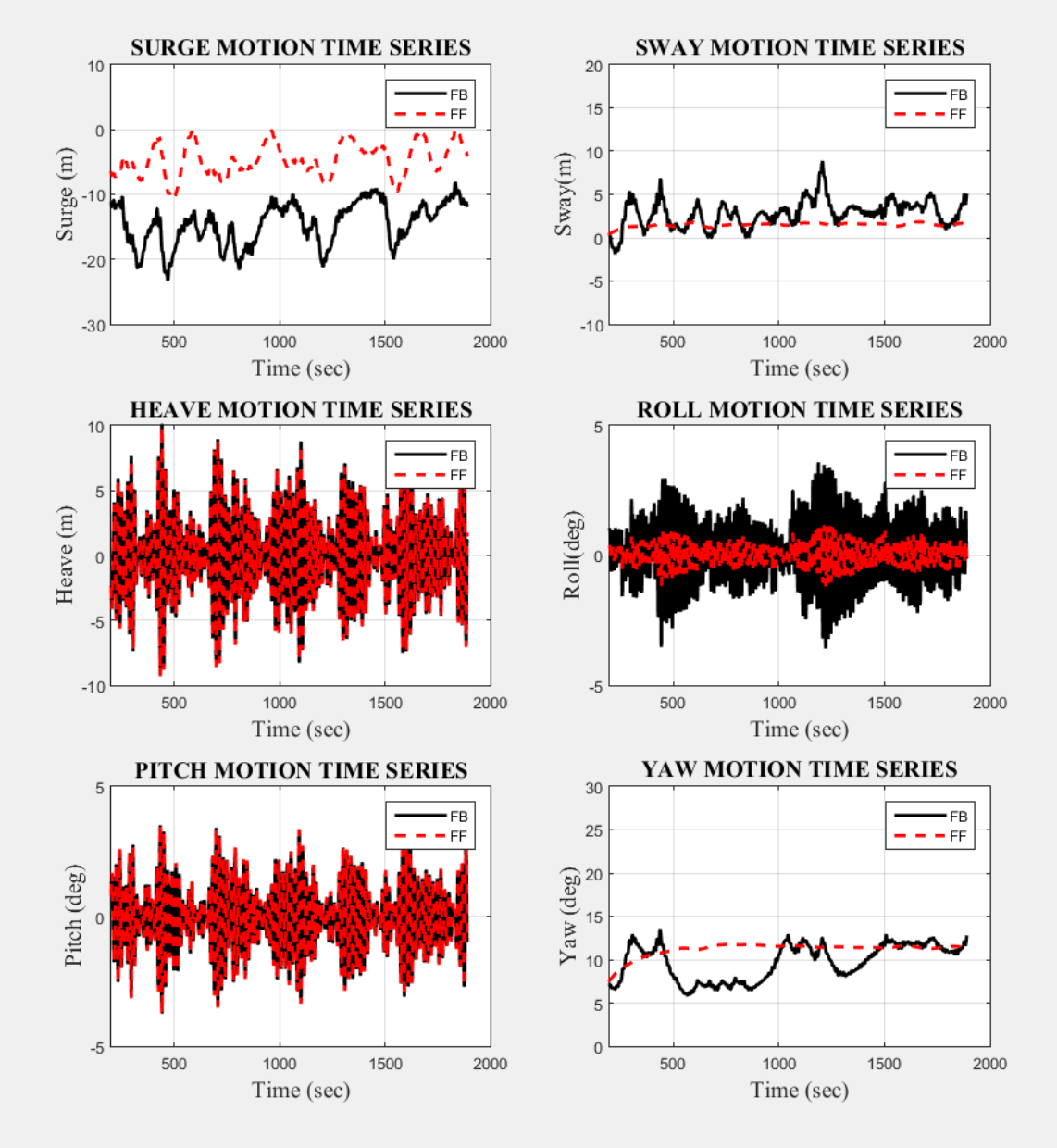

Figure 3.8 6DOF Motion History

Figure 3.9 shows 6DOF motions spectra of feedback and feed-forward control method. The position keeping performance of feed-forward control was improved in a surge, sway, roll, and yaw motion.

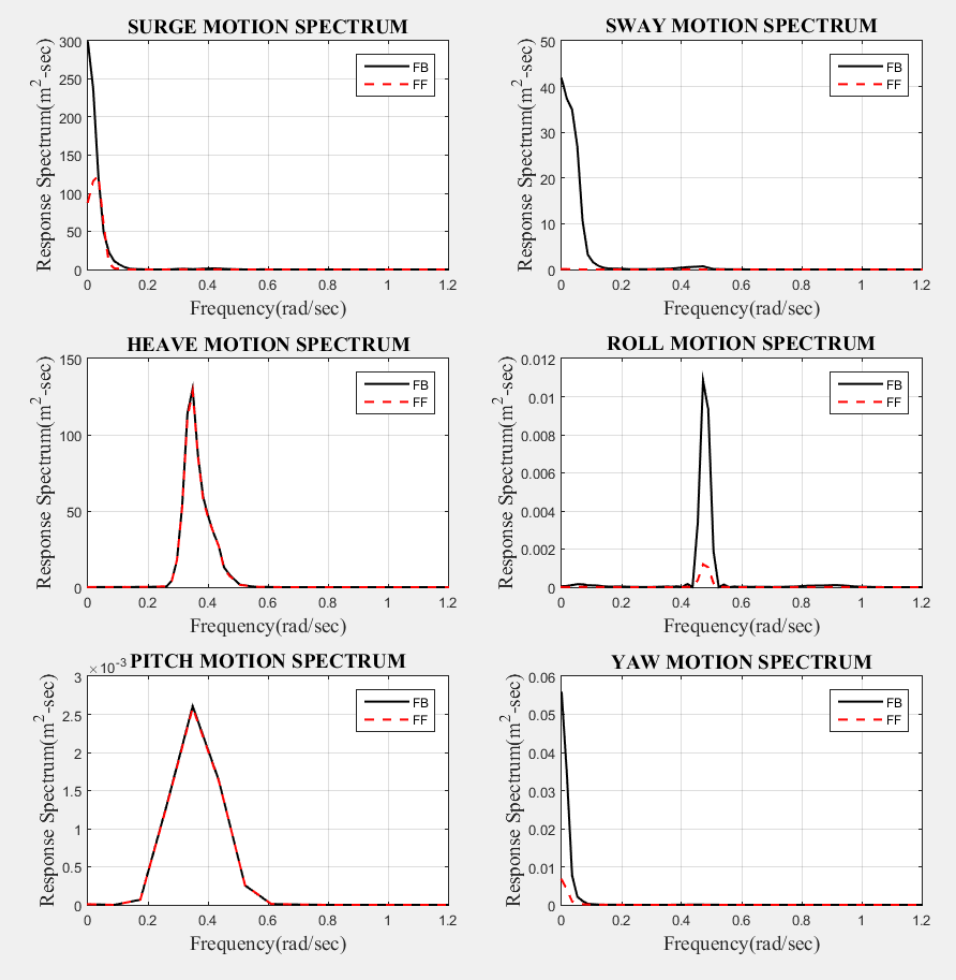

Figure 3.9 6DOF Motion Spectra

Figure 3.10 presents the mooring top-tension time histories of feedback and feed-forward control. The mooring line considered is the #2 taut-side line. The maximum mooring top tensions of feed-forward control was apparently reduced compared to that of feedback control. The surge-direction environment load attenuation by feed-forward control achieved this reduction in mooring top tension at fairlead.

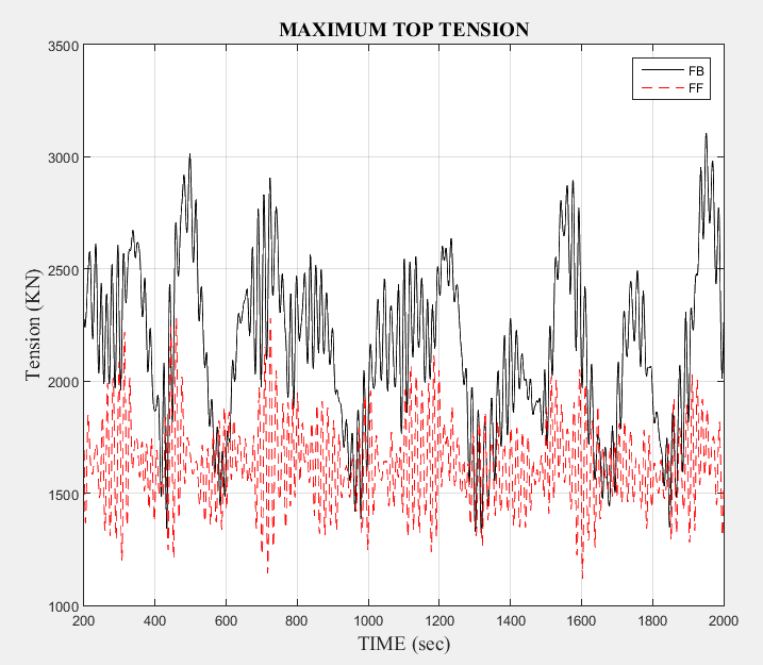

Figure 3.10 Maximum Mooring Top Tension of 100-Year Conditions by Feedback and Feed-Forward Control

In case riser which is the #22 water injection line, The maximum top tension of feedback and feed-forward control is almost similar because the heave motion is dominant for the riser top tension in Figure 3.11.

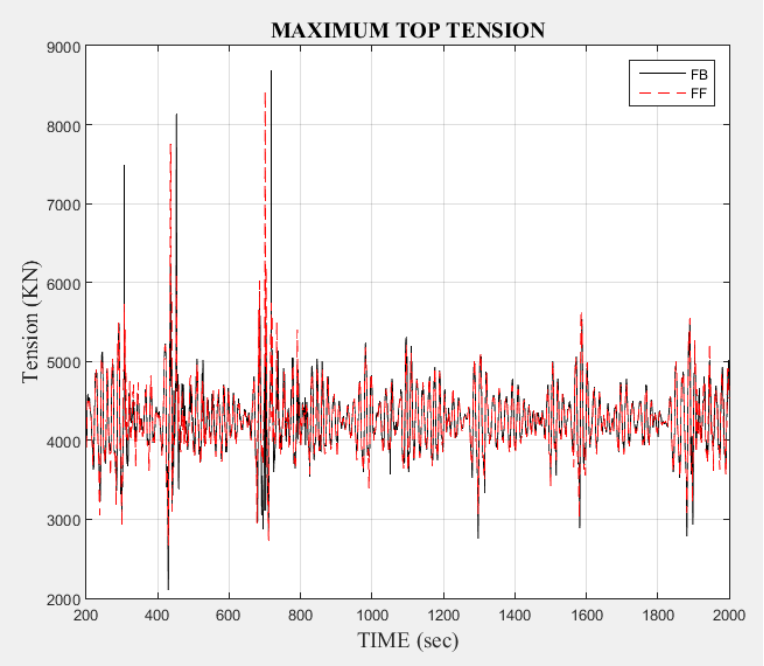

Figure 3.11 Maximum Riser Top Tension of 100-yr Condition by Feedback and Feed-Forward Control

Figure 3.12 shows the fuel consumption results when using feedback control and feed-forward control. The black line illustrates the fuel consumption of the feedback control, and the red line indicates that of the feed-forward control. The feed-forward control shows better fuel consumption performance compared to the feedback control. The feed-forward control reduces the fuel consumption by an accumulated value of 18%, compared to that of the feedback case.

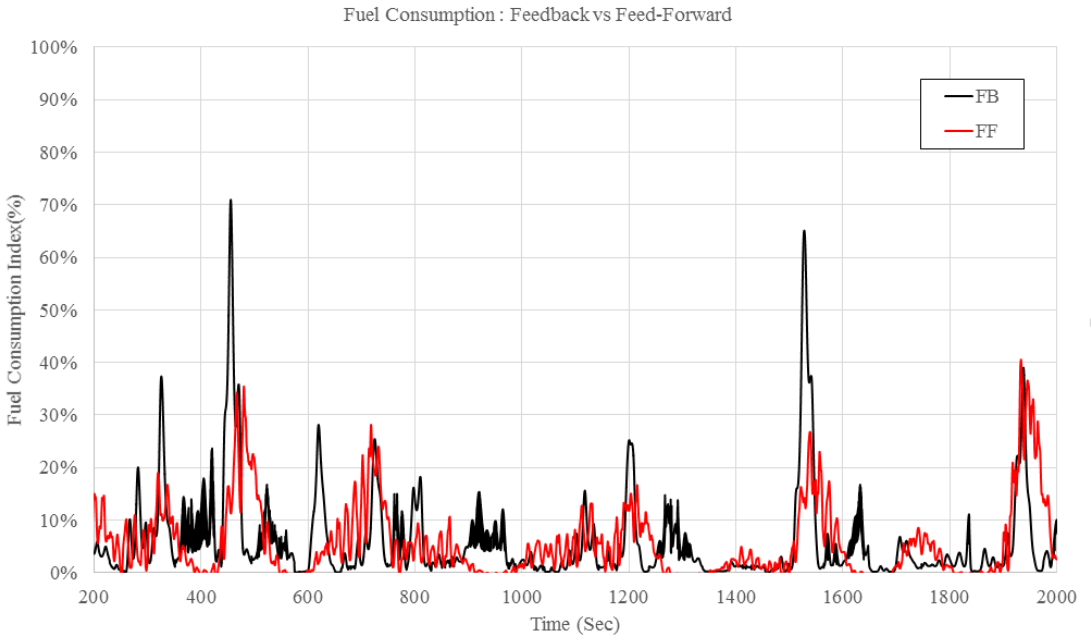

Figure 3.12 Fuel Consumption Comparison between Feedback and Feed-Forward

Following figure 3.13 presents the CO2 Gas emission amount of feed-forward and feedback case. The black line illustrates the fuel consumption of the feedback control and the red line indicates that of the feed-forward control, respectively. The results indicates

the feed-forward control attenuated the by the accumulated value 8% from that of the feedback control.

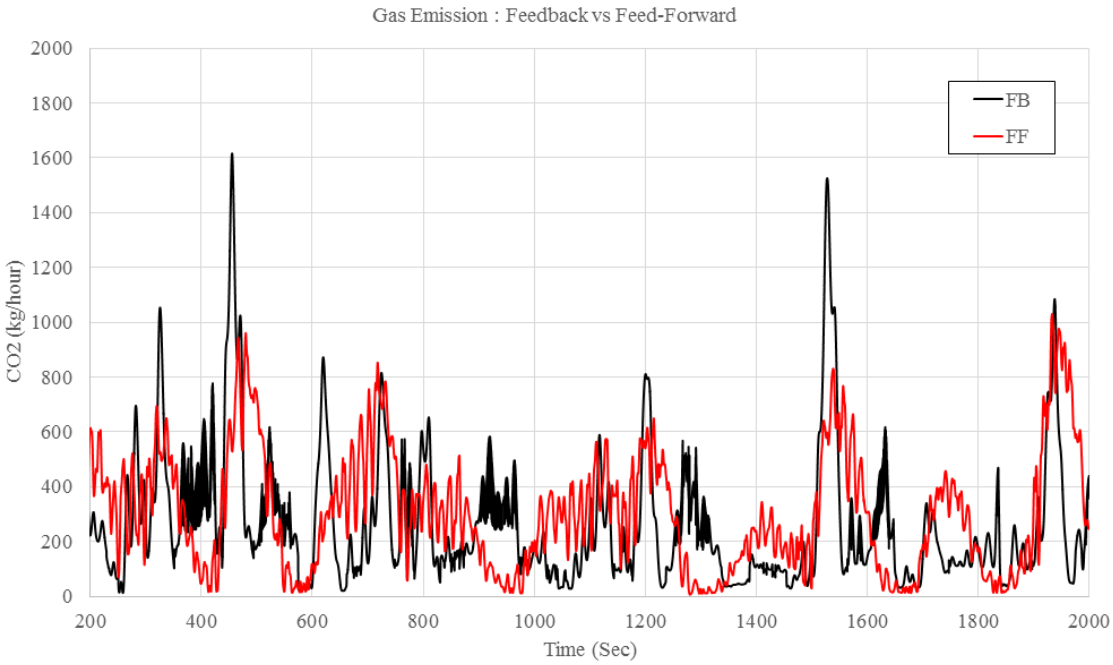

Figure 3.13 Gas Emission of the Feedback and Feed-Forward Simulation

3.6.3 Gulf of Mexico One-Year Conditions

Figure 3.14 shows the horizontal motion of the feedback control and feed-forward control under GOM one-year storm conditions. As the environmental load becomes smaller, the enhancement of feed-forward control also decreases.

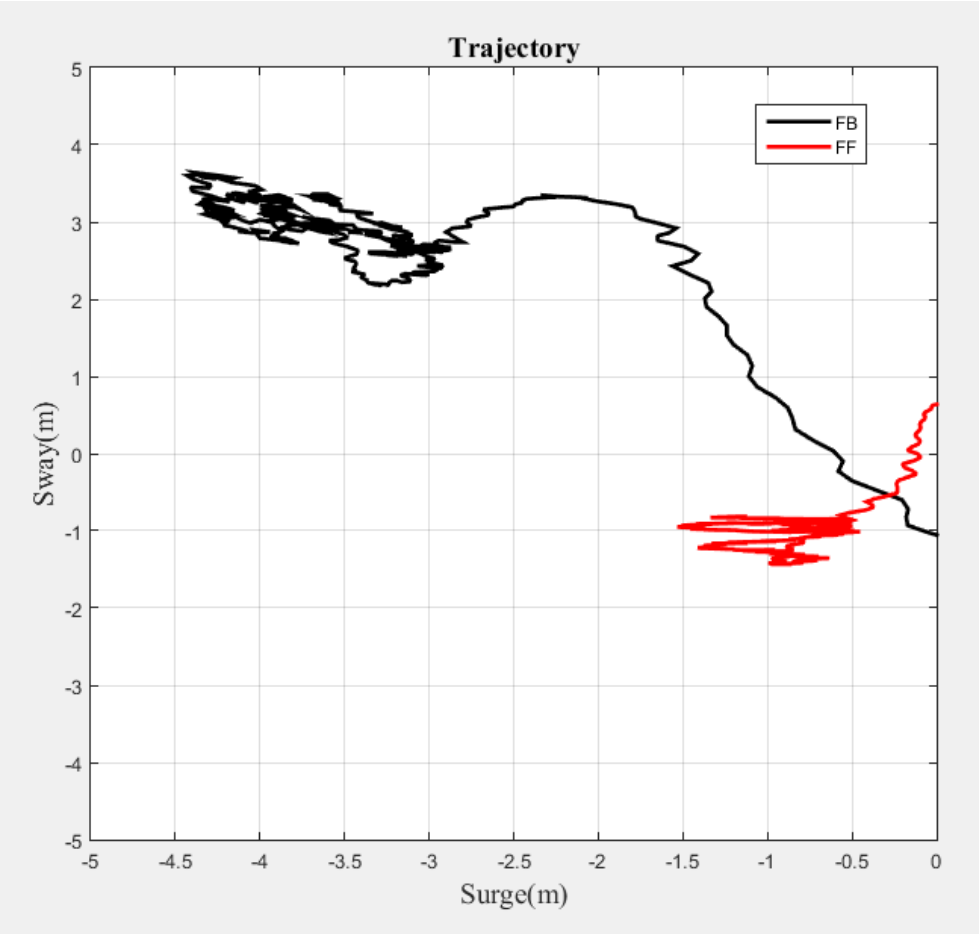

Figure 3.14 Position Difference (Surge-Sway): Gulf of Mexico One-Year Conditions

Figure 3.15 represented the horizontal motion of the feedback control and feed-forward control under GOM 1-yr storm condition. As the environmental load became weaker compare to the GOM 100-yr case, as the amount of feed-forward control position keeping performance enhancement is also decreased. However, the position keeping performance of feed-forward control is over that of feedback in surge, sway, and yaw. The surge motion feed-forward control fluctuated at the 1 m, otherwise the feedback control oscillated at the 5 m. In addition, the sway motion of feed-forward was steady at near -1m then the feedback control sway motion vibrated between 3m to 5m.

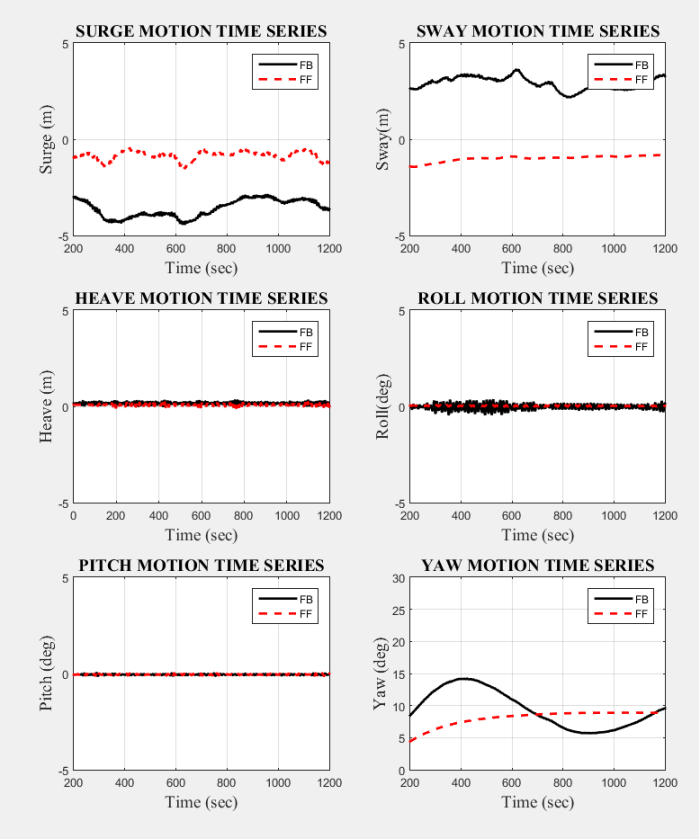

Figure 3.15 6DOF Gulf of Mexico Conditions Motion Time History, One-Year Feed-Forward versus Feedback

Figure 3.16 shows 6DOF motions spectra of feedback and feed-forward control method in GOM 1-yr case. The feed-forward control has much smaller motion spectra compared to those of the feedback control.

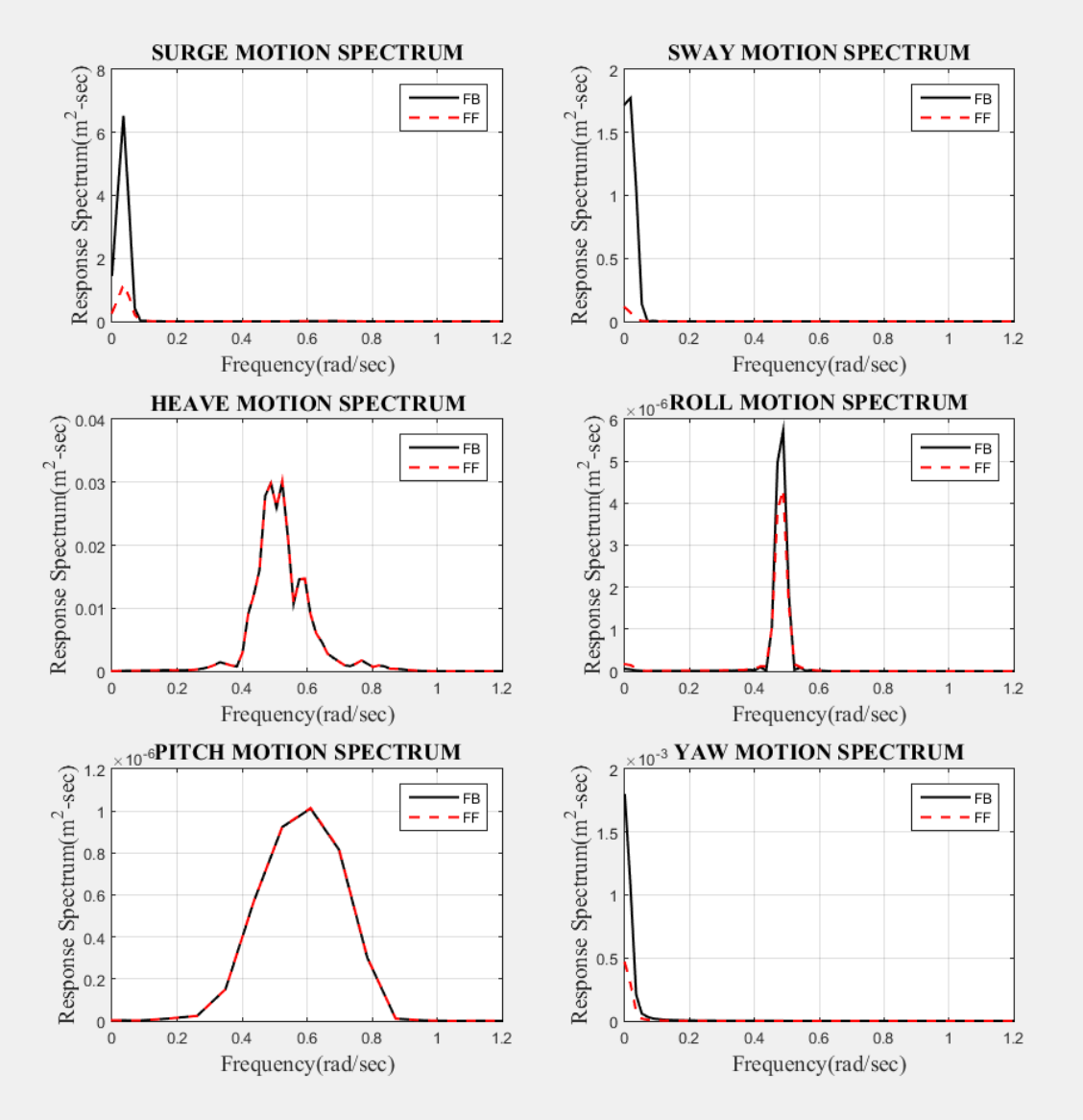

Figure 3.16 6DOF Motion Time History Gulf of Mexico One-Year, Feed-Forward versus Feedback

Figure 3.17 presents the mooring top-tension time histories of feedback and feed-forward control. The mooring line considered is the #2 taut-side line. The maximum mooring top tensions of feed-forward control was apparently reduced compared to that of feedback control. The surge-direction environment load attenuation by feed-forward control also achieved in GOM 1-yr condition in consistency.

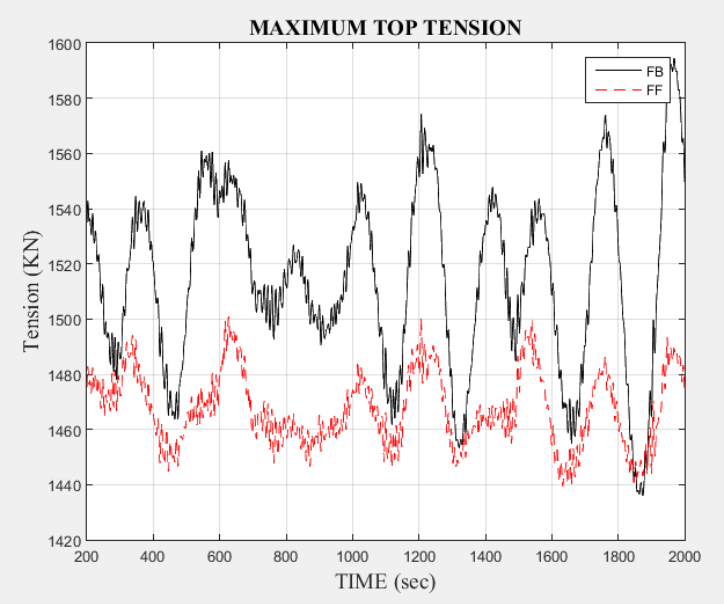

Figure 3.17 Maximum Mooring Top Tension of Feedforward Control Gulf of Mexico One-Year Conditions

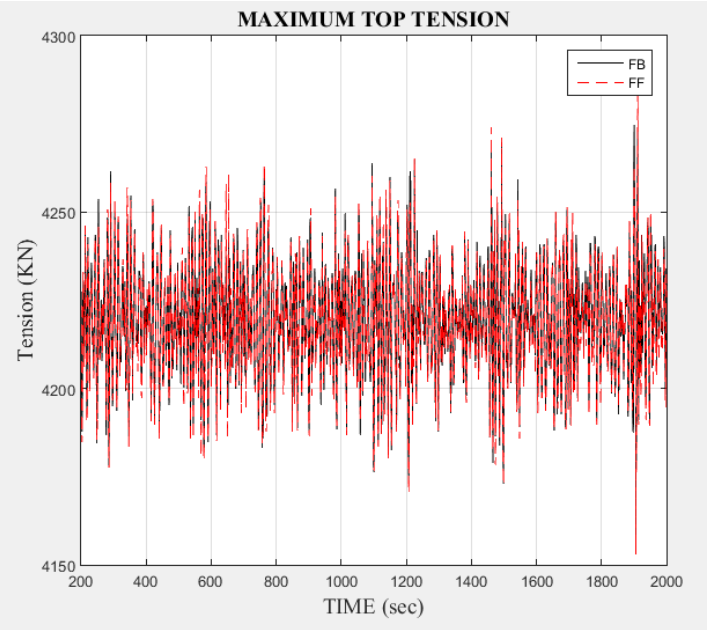

Figure 3.18 Maximum Riser Top Tension of Feed-Forward Control Gulf of Mexico One-Year Conditions

Figure 3.19 illustrated the fuel consumption trend when the feedback and feed-forward control were hired under GOM-1yr case. Amount of fuel consumption difference between two comparison cases were reduced compared to G0M 100-yr case because thrusters loads not reached to the thruster constraint. The black line illustrates the fuel consumption of the feedback control and the red line indicates that of the feed-forward control, respectively. The accumulated fuel consumption value of feed-forward control was improved by 4%.

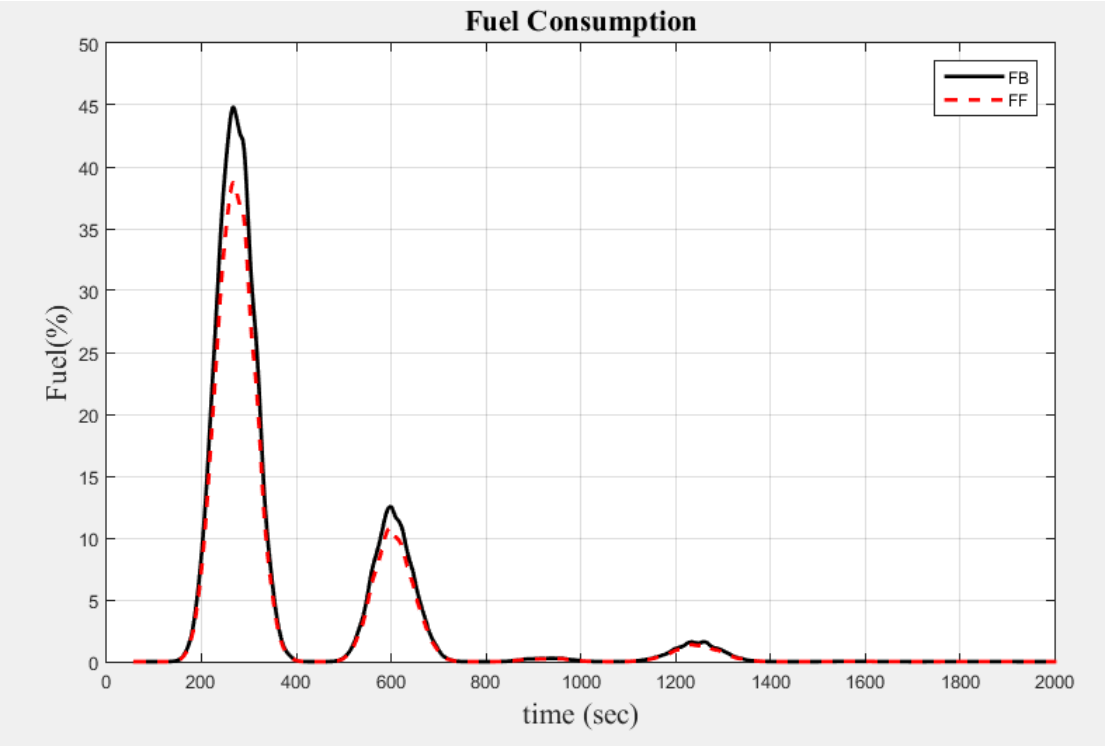

Figure 3.19 Gulf of Mexico Conditions Fuel Index Time History, One-Year Feed-Forward versus Feedback

Figure 3.20 is the CO_2 Gas emission amount of feed-forward and feedback case. According to the simulation results, the CO_2 emission of feed-forward case was small by 2.5% compare to that of feedback control case.

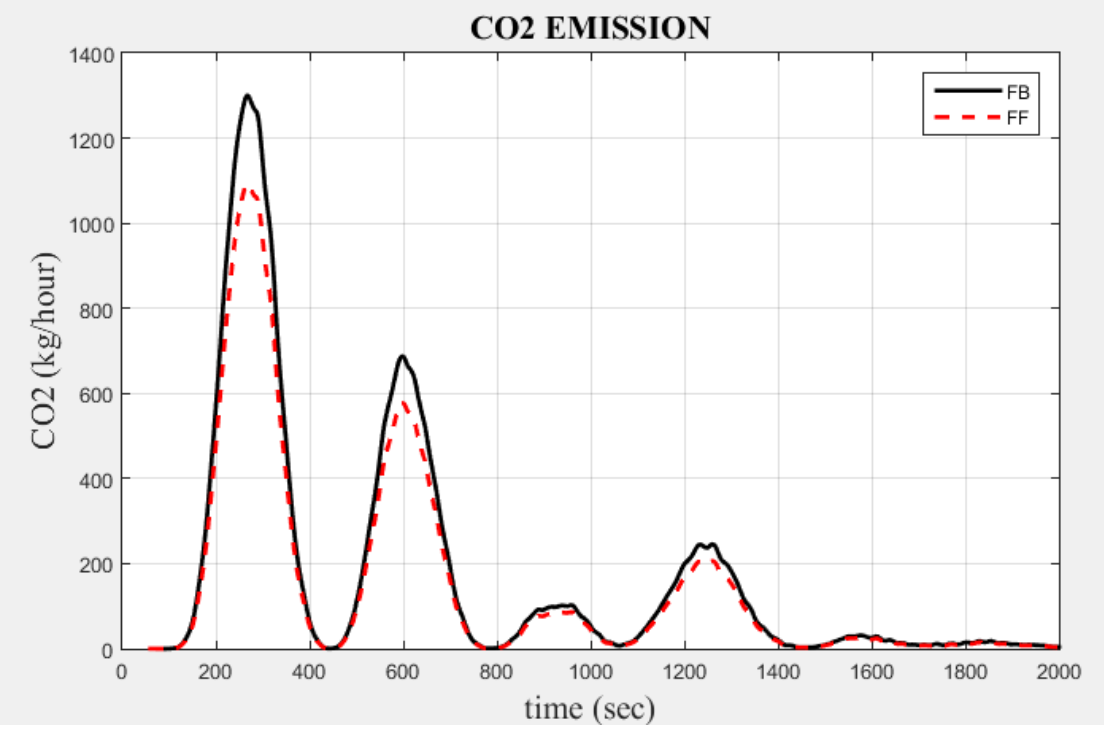

Figure 3.20 Gulf of Mexico Conditions CO_2 Time History, One-Year Feed-Forward versus Feedback

3.7 Conclusion

The feed-forward control that was designed to reduce fuel consumption and gas emission, was mathematically modeled and compared to the feedback control method. The feedback control intend to reduce position excursion error, meanwhile the feed-forward control compensates the environmental loads based on the environment physical modeling. Wind, current, and waver loads were included in the feed-forward controller. Wind and current loads were estimated based on the drag theory by using wind tunnel test results which is conventional way. Meanwhile, the second order wave load modeling was calculated by direct integration method using time domain quadratic response function and wave elevation. This method firstly implemented in the feed-forward control with optimization method.

According to the results, the feed-forward control has benefit in surge, sway, roll, and yaw motion under both GOM 1-yr and 100-yr case. In addition, the feed-forward enhanced the fuel consumption and gas emission performance. Moreover, it has a benefit in taut-side mooring tension reduction. The reason why the feed-forward control can improve the position keeping, fuel consumption, and gas emission performance, is the pre-emptive control method that can attenuate the response before the large excursion occurred. Generally, the inertia of offshore platform is enormous therefore the feed-forward control can react efficiently in the initial movement stage due to environmental loads.

CHAPTER IV

DYNAMIC POSITIONING PERFORMANCE OF FPSO DUE TO TURRET POSITION

4.1 Introduction

For the past two decades, the internal turret mooring FPSO is a dominant paradigm for FPSO development. The turret system has a bearing that permits FPSOs to rotate freely so that the heading of the vessel can be towards the direction of minimal environmental force. The FPSO turret position is an important factor for top-side design and overall system dynamics. The system dynamics and performance are related to the turret position. As the turret position approaches the bow part of the vessel, the weathervaning capability is generally improved but the vertical motion at its location can significantly be increased due to coupling with pitch motion, which is a big concern for mooring and riser design. Particularly when steel catenary risers are used, large amplitude downward motion at turret can cause serious structural problem for risers. If the turret is located in the mid part of the vessel, the vertical motion can significantly be reduced without pitch-induced contribution, which is good for mooring-riser design. The disadvantage of the mid-ship turret position is that it generally increases yaw motions, and thus heading control is more difficult. The disadvantage of the midship turret can be overcome by additionally employing DP system.

Considering those pros and cons, the Gryphon FPSO was developed to have mid-ship internal turret with the dynamic positioning system in the North Sea. Unfortunately, during a less-than survival condition, its DP system failed and risers and mooring lines

were damaged. It occurred in February 2011 from 175 miles north east of Aberdeen under the wind speed 60 knots and wave height about 12 meters. The FPSO lost its heading control and faced environmental loads from beam side. In consequence, the anchors and mooring lines were damaged. Figure 4.1 shows the anchor chain failure.(Finucane, 2012).

Figure 4.1 The Anchor Chain Failure of Gryphon (Finucane, 2012)

The Gryphon originally equipped ten mooring lines connected to mid-ship turret, as shown in Figure 4.2, and it was assisted by five-thruster DP system. The DP system was responsible for heading control but when it was shut-down during the incident. As a result, mooring lines could not bear unexpected environmental loadings from beam side. Figure 4.2 presents the initial stage of the Gryphon FPSO drive off incident. The Gryphon initially maintained the heading towards the wind direction.

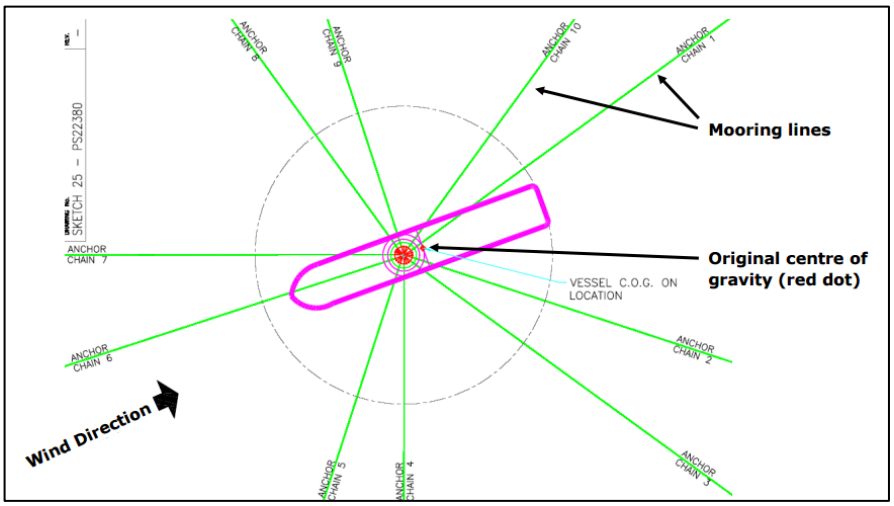

Figure 4.2 The Initial Stage of the Gryphon (Finucane, 2012)

Figure 4.3 presents the final stage of the Gryphon FPSO incident, in which four moorings were disconnected and four anchor chains broken. The FPSO drifted off 180m in a sway direction.

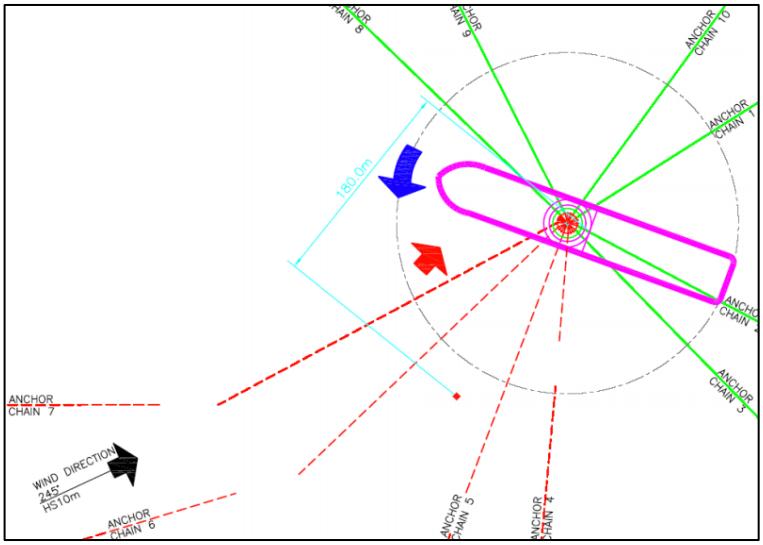

Figure 4.3 The Final Stage of the Gryphon (Finucane, 2012)

This kind of circumstance needs to be checked during the design stage. However, the fully coupled hull-mooring-riser-DP analysis tool in time domain is very rare. The authors have developed such a simulation program in time domain and it is used here to investigate the global dynamic performance of a turret-moored FPSO with DP control.

4.2 Literature Review

Thiagarajan and Finch (1999) conducted wave tank tests to evaluate global motion change resulting from four turret locations: external, internal bow, internal mid-ship, and internal stern turret. They found that the lowest vertical motion occurred at the turret near the longitudinal center of gravity (LCG). The vertical motion internal bow turret and mid-turret vertical motion are smaller than that of the external turret. The stern internal turret location is very poor in terms of vertical motion performance. The magnitude of the vertical motion at the stern location is twice that of the bow and the mid-turret. In addition, acceleration at the stern turret position could be several times larger than the bow and mid-turret locations. Duggal, Heyl, and Vance (2000) conducted a numerical analysis and model test to define the ability of the FPSO with an internal turret mooring system to withstand the eastern sea of Canada during 100-year storm conditions. The found that the mid-ship turret considerably enhanced vertical stability compared to the bow turret. Otherwise, the equilibrium heading angle of the mid-ship turret was increased from 0 degrees at the bow turret to 90 degrees in the case of the mid-ship turret. This phenomenon degrades the horizontal stability of the FPSO.

Kannah and Natarajan (2006) analyzed the global performance of FPSO with varying internal turret locations. They tested three internal turret positions: bow, mid-ship, and semi-aft. They considered 40%, 70%, and 100% loading conditions under linear wave conditions coming from the head sea and found that the heave RAO of the bow location is smaller than that of the mid-ship turret. These findings are quite controversial, however, because they conflict with previous research, most of which argued that the mid-ship turret location is best option in vertical motion performance.

There apparently have been no studies to date on the global performance change due to FPSO turret positions with a thruster-assisted mooring system. Therefore, this dissertation will analyze the global performance of the DP FPSO with turret moorings located in the bow and mid-ship.

4.3 Aims

This chapter aims to analyze the global dynamic performance of a turret-moored FPSO with DPS for two internal turret positions. Both collinear and non-collinear 100-yr storm conditions are considered. The 6DOF FPSO motions and mooring tensions with and without DPS are compared. When DP is employed, the cases of position control only and position+heading control are also compared. The fuel consumptions of the corresponding DP cases are also compared.

4.4 Simulation Model Description

The DP FPSO has a 200,000-ton tanker moored in 1,829m water depth. Hull, mooring, riser, and DP coupled time domain simulations were conducted based on CHARM3D program (e.g. Yang & Kim, 2011; Kang & Kim, 2014) developed by the research group of second author during the past 20 years. The wind and current forces for different headings are based on the OCIMF(Oil Companies International Maritime Forum) data. The wave forces are calculated for many heading angles with 5-degree interval (Tahar & Kim, 2003). The second-order slowly varying wave forces and vessel responses are based on the Newman's approximation, which has been validated through comparison with experiment (M. Kim, Koo, Mercier, & Ward, 2005). The wave forces and hydrodynamic coefficients of the hull are calculated from 3D diffraction/radiation panel program WAMIT. The panel discretization used for the present FPSO is illustrated in Figure 4.4 and 5. The hull viscous damping is included through modified Morison formula representing cross-flow drags.

The major control variable of this chapter is turret position. The bow and mid-turret positions are considered in the simulation. In the bow turret case, the turret location is identical with that of the previous chapters (2.4.2). The principal, particular variation due to turret location is presented in Table 4.1.

Table 4.1 Principal Details of the Bow and Mid-Ship Turret Simulation

Designation	Symbol	Unit	BOW	MID
Trans. radius of gyration in air	Kxx	m	14.8	14.2
Long. radius of gyration in air	Kyy	m	77.5	134.3
Yaw radius of gyration	Kzz	m	79.3	135.3
Turret in centerline behind Fpp (turret position)		m	63.5	155

The DEEPSTAR FPSO 100% DWT load hull panel is used for the simulation, which is consistent with the previous Chapter III.

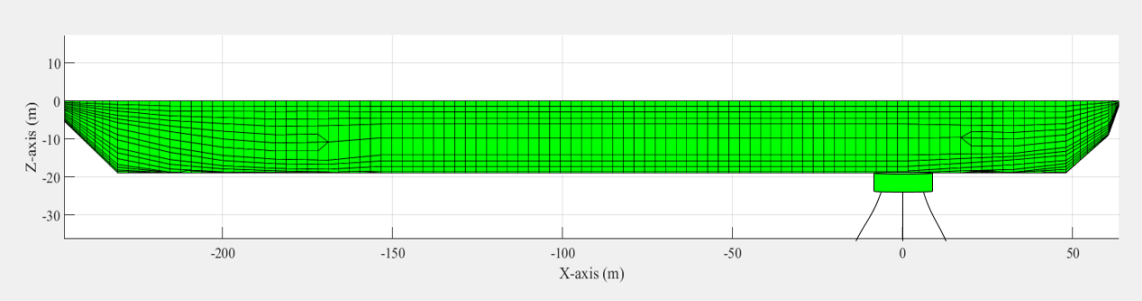

Figure 4.4 Bow Turret Case Mesh Model

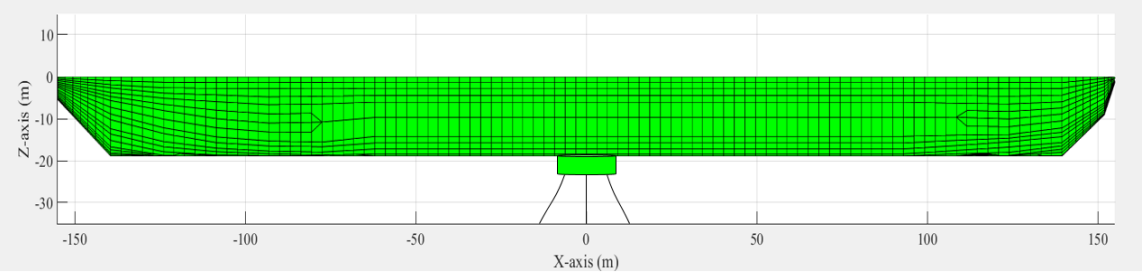

Figure 4.5 Mid-Ship Turret Mesh Model

Twelve chain-polyster-chain mooring lines and thirteen steel catenary risers are applied in the simulation. The mooring and riser elements are modeled by high-order FEM (finite element method; Ran & Kim, 1997). Six azimuth thrusters were implemented in the simulation for both bow and mid-turret cases. The hull mesh with the inner-bow and mid-ship-turret and mooring, DP, and riser arrangement are, for example, shown in Figure 4.6 and 4.7.

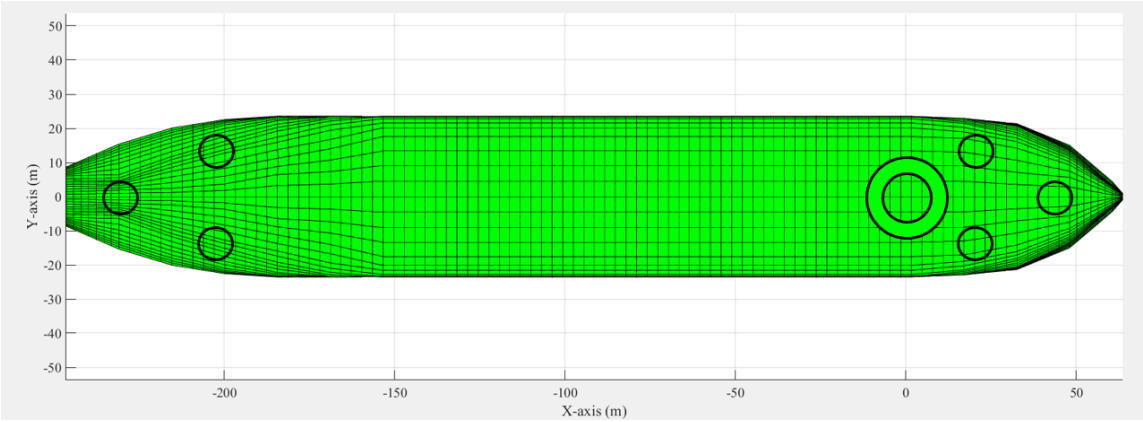

Figure 4.6 Thrusters and Turret Arrangement: Bow Turret

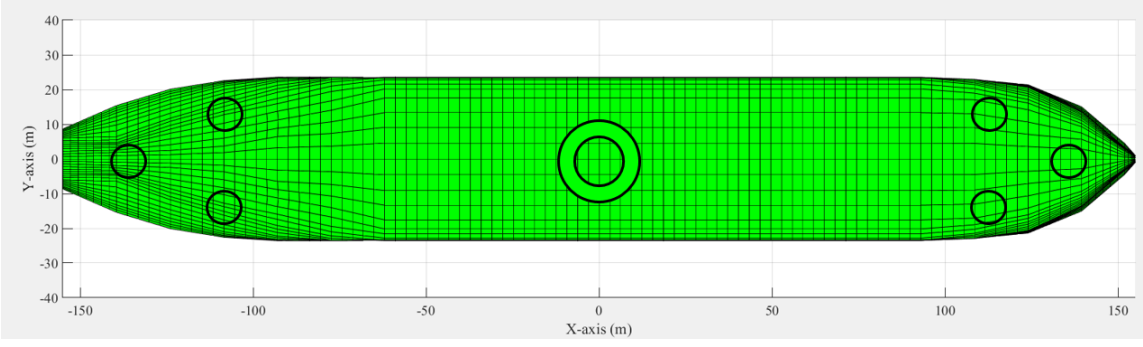

Figure 4.7 Thrusters and Turret Arrangement: Mid-Ship Turret

The extended Kalman Filter, the PID controller based on the LQR theory, and the penalty-method-based thrust allocation were integrated in the DP controller used in this chapter. The PID gain was calculated to minimize energy input and the thrust allocation based on the penalty method was designed to minimize fuel consumption.

The forces and moments that can maintain the position of an offshore platform can be defined by multiplying PID gain and error matrix. The key function of the PID controller design is to define the gain control. In this PID controller design, the system of the offshore platform is assumed to be the linear, time-invariant system. A linear, time-invariant system of equations of motion follows the following form:

$$\dot{\mathbf{x}} = \mathbf{Ax} + \mathbf{Bu}, \mathbf{y} = \mathbf{Cx} + \mathbf{v} \tag{4.1}$$

where dot (·) denotes the time derivative, and each vector, written in lower case, can be described by the following set of definitions:

State $\mathbf{x} = [u, x, v, y, \omega, \psi]^T$ Control Input $u = \left[\tau_x, \tau_y, \tau_\phi\right]^T$ Measurement $\mathbf{y} = [x, y, \psi]^T$

Measurement-Noise $\mathbf{v} = [v_\chi, v_y, v_\psi]^T$

where $\mathbf{A} = \mathbf{M}^{-1}\begin{bmatrix} 0 & 0 & 0 & 0 & 0 & 0 \\ 1 & 0 & 0 & 0 & 0 & 0 \\ 0 & 0 & 0 & 0 & 0 & 0 \\ 0 & 0 & 1 & 0 & 0 & 0 \\ 0 & 0 & 0 & 0 & 0 & 0 \\ 0 & 0 & 0 & 0 & 1 & 0 \end{bmatrix}$ $\mathbf{B} = \mathbf{E} = \mathbf{M}^{-1}\begin{bmatrix} 1 & 0 & 0 \\ 0 & 0 & 0 \\ 0 & 1 & 0 \\ 0 & 0 & 0 \\ 0 & 0 & 1 \\ 0 & 0 & 0 \end{bmatrix}$ $\mathbf{C} = \begin{bmatrix} 0 & 1 & 0 & 0 & 0 & 0 \\ 0 & 0 & 0 & 1 & 0 & 0 \\ 0 & 0 & 0 & 0 & 0 & 1 \end{bmatrix}$

where $M_{11} = m + a_{11}(0)$ $M_{22} = m + a_{22}(0)$ $M_{26} = m + a_{26}(0)$ $M_{62} = m + a_{62}(0)$ $M_{66} = I + a_{66}(0)$, m the mass of the floating structure, I , is the moment of inertia in z-direction, and $a_{ij}(0)$ added masses in low frequency, and $\hat{x}$ is the state estimation vector.

The mass, moment of inertia, and restoring coefficient matrix due to turret location were investigated by using the frequency domain diffraction analysis program.

In the thrust allocation module, the penalty method that showed the best fuel consumption performance in Chapter II was used. The distance of the thrusters differed based on turret location. Therefore, those factors are considered in the required forces and moments constraint of the optimization problem.

Object to

$$\min\left(\frac{1}{2}x^{T}Hx+\frac{1}{2}u^{T}Ku+c\begin{pmatrix}\max\{0,\mathrm{u}-\mathrm{u}_{\max}\}^{2}+\max\{0,u_{\min}-u\}^{2}\\+\max\{0,\dfrac{u_{previous}-\mathrm{u}_{current}}{dt}-\dot{\mathrm{u}}_{\max}\}^{2}+\left(RF-Bu\right)^{2}\end{pmatrix}\right) \tag{4.2}$$

where,

H : *State weight matrix*
K : *Fuel consumption parameter weight matrix*
RF : *Required force & moment matrix* (3×1)
B : *Thrust allocation matrix* $(3\times n)$
u : *Thruster matrix* $(n\times1)$
$u_{\min}, u_{\max}$: *Thrust constraint*
$\dot{u}_{\max}$: *Thrust rate constraint*

$$RF=\begin{bmatrix}X\\Y\\N\end{bmatrix}=\begin{bmatrix}T_{x1}\cos\alpha_1+T_{x2}\cos\alpha_2+.....T_{xn}\cos\alpha_n\\T_{y1}\sin\alpha_1+T_{y2}\sin\alpha_2+.....T_{yn}\sin\alpha_n\\y_1T_{x1}\cos\alpha_1-x_1T_{y1}\sin\alpha_1+y_2T_{x2}\cos\alpha_2-x_2T_{y2}\sin\alpha_2+....+y_nT_{xn}\cos\alpha_n-x_nT_{yn}\sin\alpha_n\end{bmatrix}$$

Three environmental conditions are considered for the simulation in this chapter. At first, GOM 100-year, collinear wind, current, and wave conditions that simulated environmental load originating in the head sea of the FPSO were conducted to confirm the simulation's validity. Then, the GOM 100-year, noncollinear case was performed to show the difference in motion characteristics under harsh environmental conditions. Finally, the

GOM one-year storm condition was calculated in the simulation to evaluate motion performance under mild environmental conditions. The coordinate of the body and environmental load are presented in Figure 4.8 and 9.

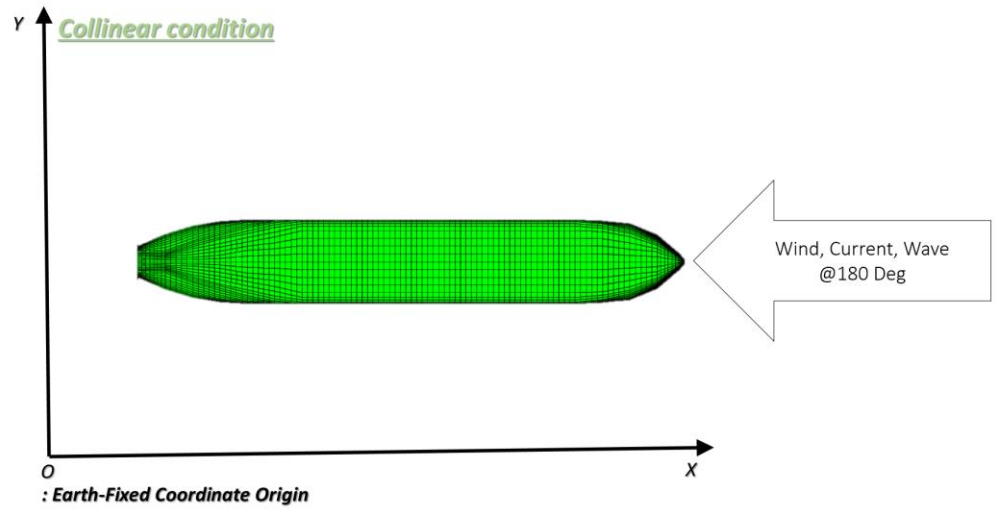

Figure 4.8 Collinear Environmental Loads Condition

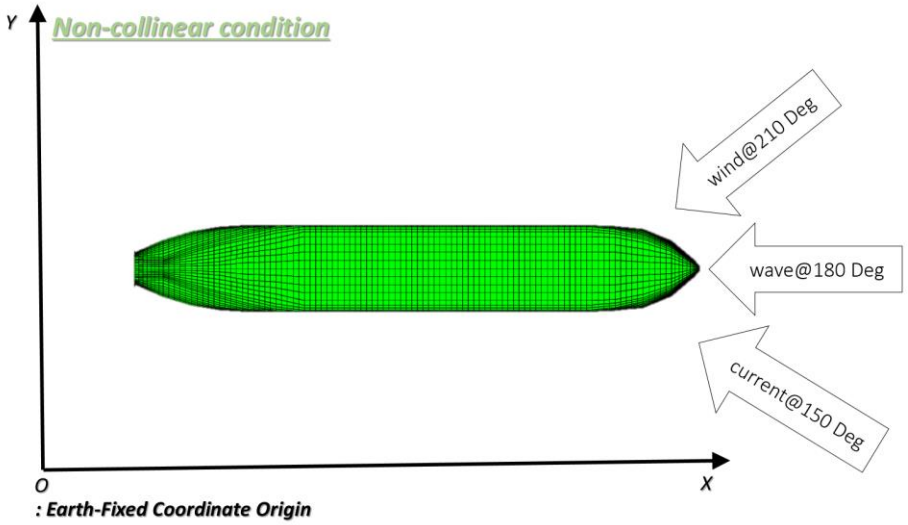

Figure 4.9 Noncollinear Environmental Loads Condition

Simulation conditions for chapter IV are summarized in Table 4.2.

Table 4.2 Simulation Environment Condition Matrix

		GOM 100-yr Co-linear	GOM 100-yr Noncollinear	GOM 100-yr Noncollinear		GOM 1-yr Noncollinear	
Positioning System		X	X	O		O	
Heading Control		X	X	X	O	X	O
Simulation Case		4.5.1	4.5.2	4.5.3	4.5.4	4.5.5	4.5.6
WAVE	Significant Wave Height H_s	12.19m	12.19m	12.19m		4.3m	
	Peak Period T_p	14sec	14sec	14sec		9sec	
	Overshoot Parameter γ	2.5	2.5	2.5		2	
WIND		41.1m/sec at 10m	41.1m/sec at 10m	41.1m/sec at 10m		14.3m/sec at 10m	
CURRENT		1.07 m/sec	1.07 m/sec	1.07 m/sec		0.33m/sec	

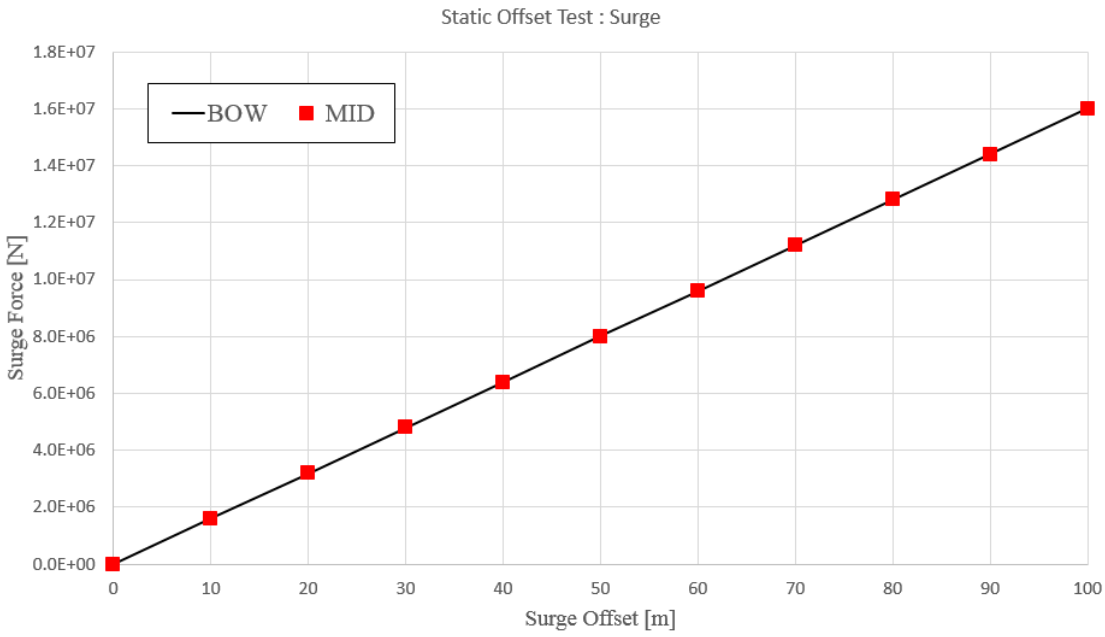

Figure 4.10 Static Offset Test

A static offset simulation was conducted to validate the simulation model. The static offset measured the change of the offset by imposing an artificial static force to the hull in a certain direction. In surge motion, it is not affected due to the turret position. Figure 4.10 shows the result of the surge static offset test. The mid-ship and bow turret locations show similar results because the mooring and riser configuration are identical. As a result, the stiffness of the floating positioning system is the same. The P gain of the dynamic positioning system is defined as 800kn based on these static test results.

4.5 Simulation Results

In the following, we compare the FPSO motions and mooring fairlead tensions for two different turret positions. The origin for the response for the two cases is located at the respective turret positions.

4.5.1 Collinear Case Simulation Results

The GOM 100-yr storm collinear condition was simulated first without DP system. As expected, the surge response, shown in Figure 4.11, is dominated by slowly-varying motions and the two turret positions produce almost the same surge time histories. This suggests that the turret location has negligible effect on surge motion.

The heave motion, however, shows big difference between the two cases. The heave amplitude of the mid-ship is significantly (70%) decreased because there is no pitch-induced heave motion. In the bow-turret case, the contribution from the pitch-induced heave is much greater than the pure heave, as can be seen in Figure 4.12.

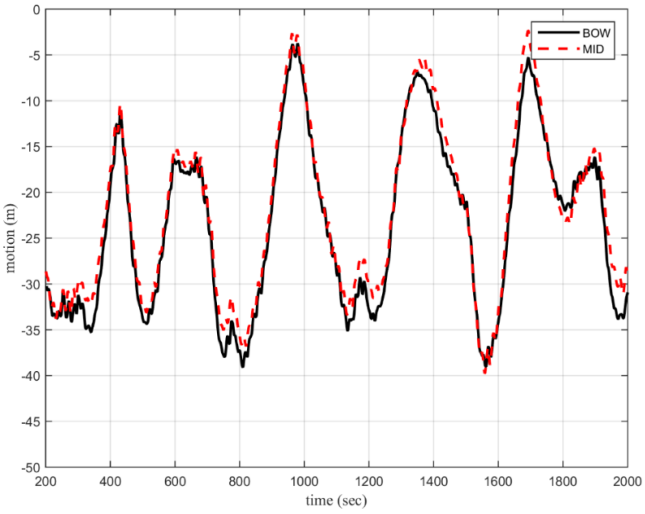

Figure 4.11 Surge Motion Time Series of Gulf of Mexico 100-Year Collinear Environment

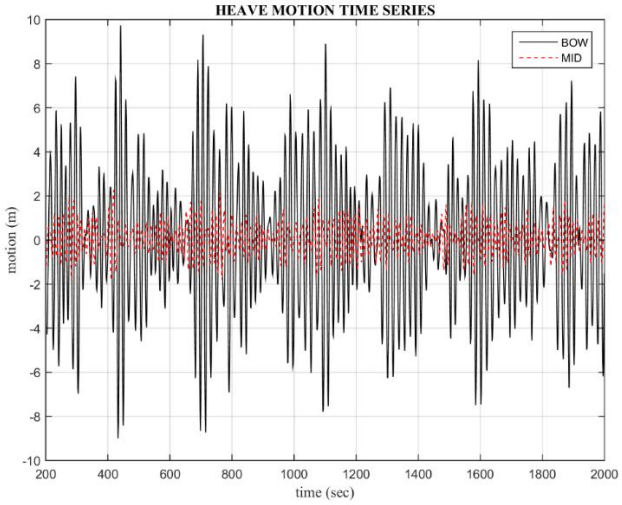

Figure 4.12 Heave Motion Time Series of Gulf of Mexico 100-Year Collinear Environment

In case of midship turret, heave is small since pitch-induced-heave is not included. The pure heave motion is also small in this case because the heave RAO itself calculated from WAMIT is small near the peak of the input wave spectrum. For double checking, the heave RAO is regenerated from the time series of the mid-turret case by using the square root of the ratio of the heave-response spectrum to the incident wave spectrum. It agrees very well with WAMIT-calculated RAO as shown in Figure 4.13.

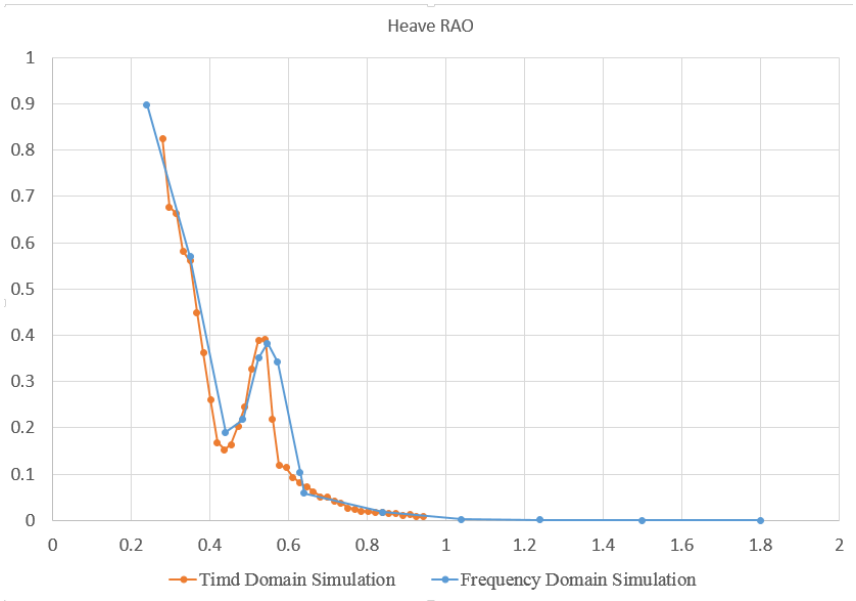

Figure 4.13 Heave RAO Comparison for Validation

The pitch-motion time series is presented in Figure 4.14. As expected, the pitch amplitude is not sensitive to the turret location. Although there exist small differences in the pattern of the time series, when their spectra are compared, they are almost the same.

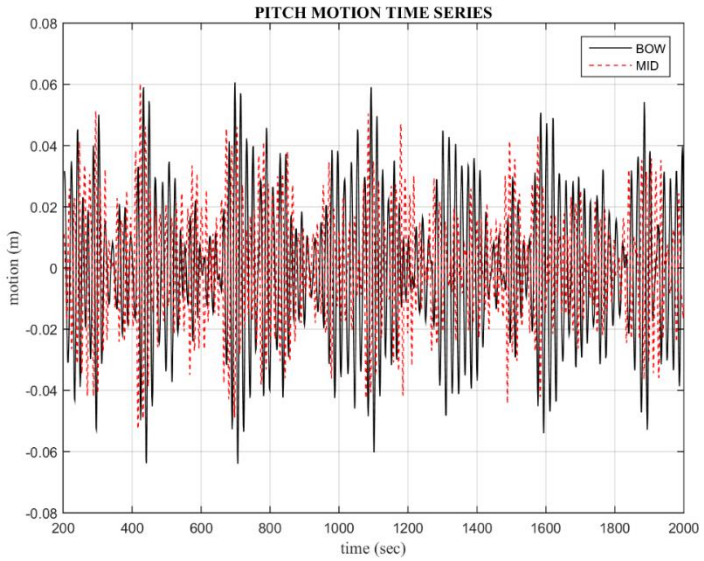

Figure 4.14 Pitch Motion Time Series of Gulf of Mexico 100-Year Collinear Environment

Figure 4.15 shows the pitch spectral densities of the mid-ship and the bow turret locations. Those are well matched and the substantial responses are the same in the frequency domain.

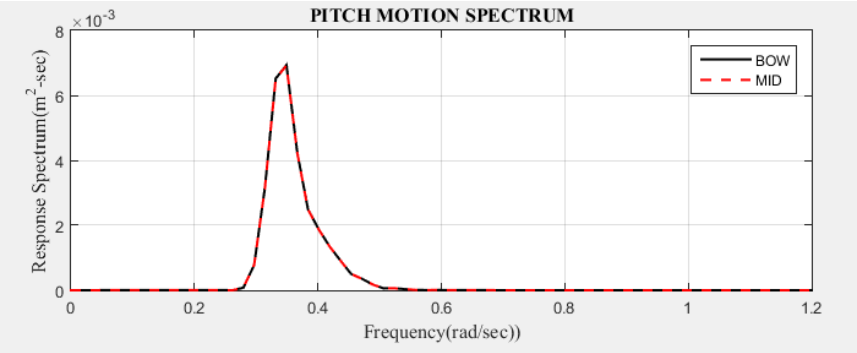

Figure 4.15 Pitch Motion Spectrum of Gulf of Mexico 100-Year Collinear Environment

Figure 4.16 presents the mooring top-tension time histories of the mid- and bow-turret cases. The mooring line considered is the #2 taut-side line. The maximum tensions of mooring the bow and mid-turret cases are 3210 KN and 3060 KN. In the mid-ship case, the heave induced high frequency force part was vanished compared to the bow turret case. In case riser which is the #22 water injection line, the maximum tensions of the bow- and mid-turret cases are 8800 KN and 4600KN in Figure 4.17. The maximum value of the mid-ship turret is about 52% of the bow-turret case. The vertical motion reduction is the main reason of this tendency. Large downward heave motions are very critical for the design of steel catenary risers since it can cause temporal local dynamic buckling near the touch-down point (Eom et al. 2014; Kim & Kim, 2015). So, from FEED engineers' point of view, with regard to the mooring and riser design, the mid-turret position looks very attractive, which was the main motivation of the Gryphon mid-turret design. Then, the next question is "Do we have the same advantage by using mid turret even in similarly harsh non-collinear environment?". We will investigate this in the next section.

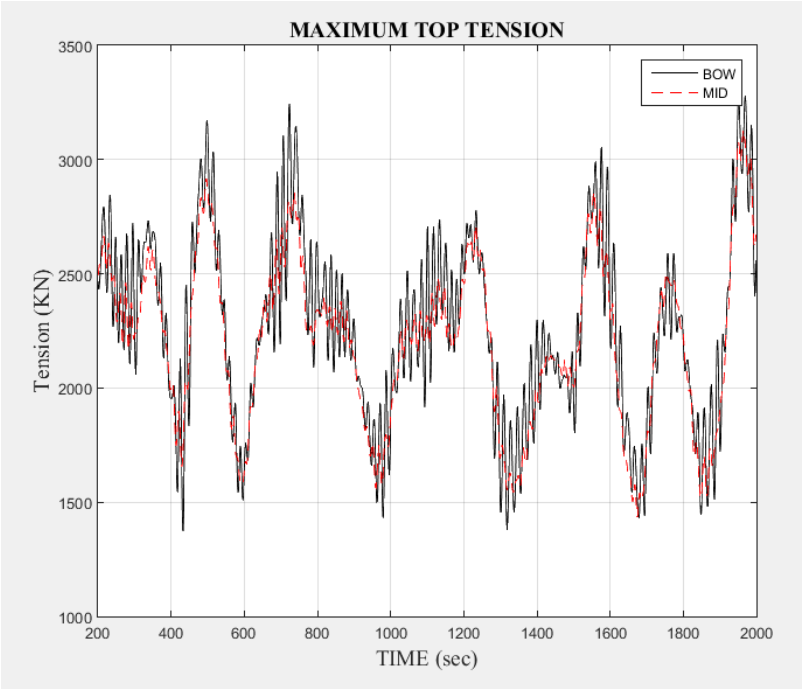

Figure 4.16 Maximum Top Tension of Moorings in GOM 100-yr Collinear Environment (mooring only case)

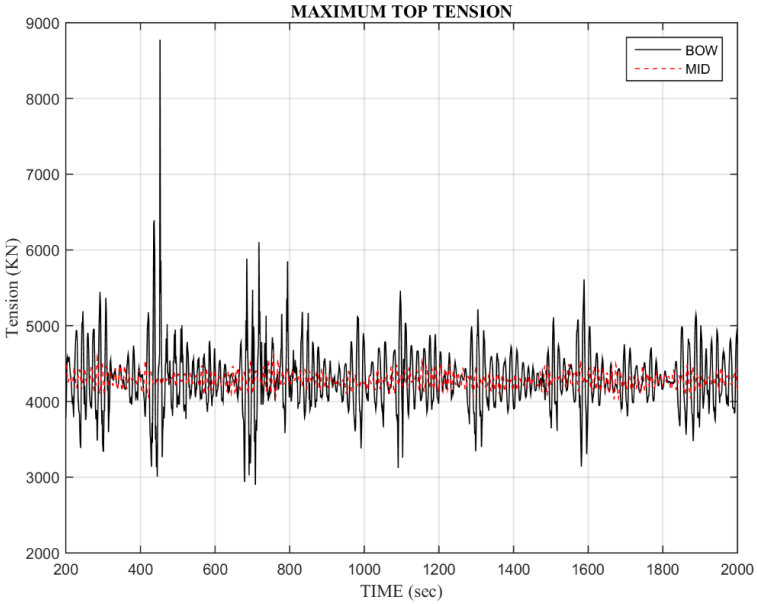

Figure 4.17 Maximum Top Tension of Gulf of Mexico 100-Year Collinear Environment

4.5.2 Gulf of Mexico 100-Year Mooring Only

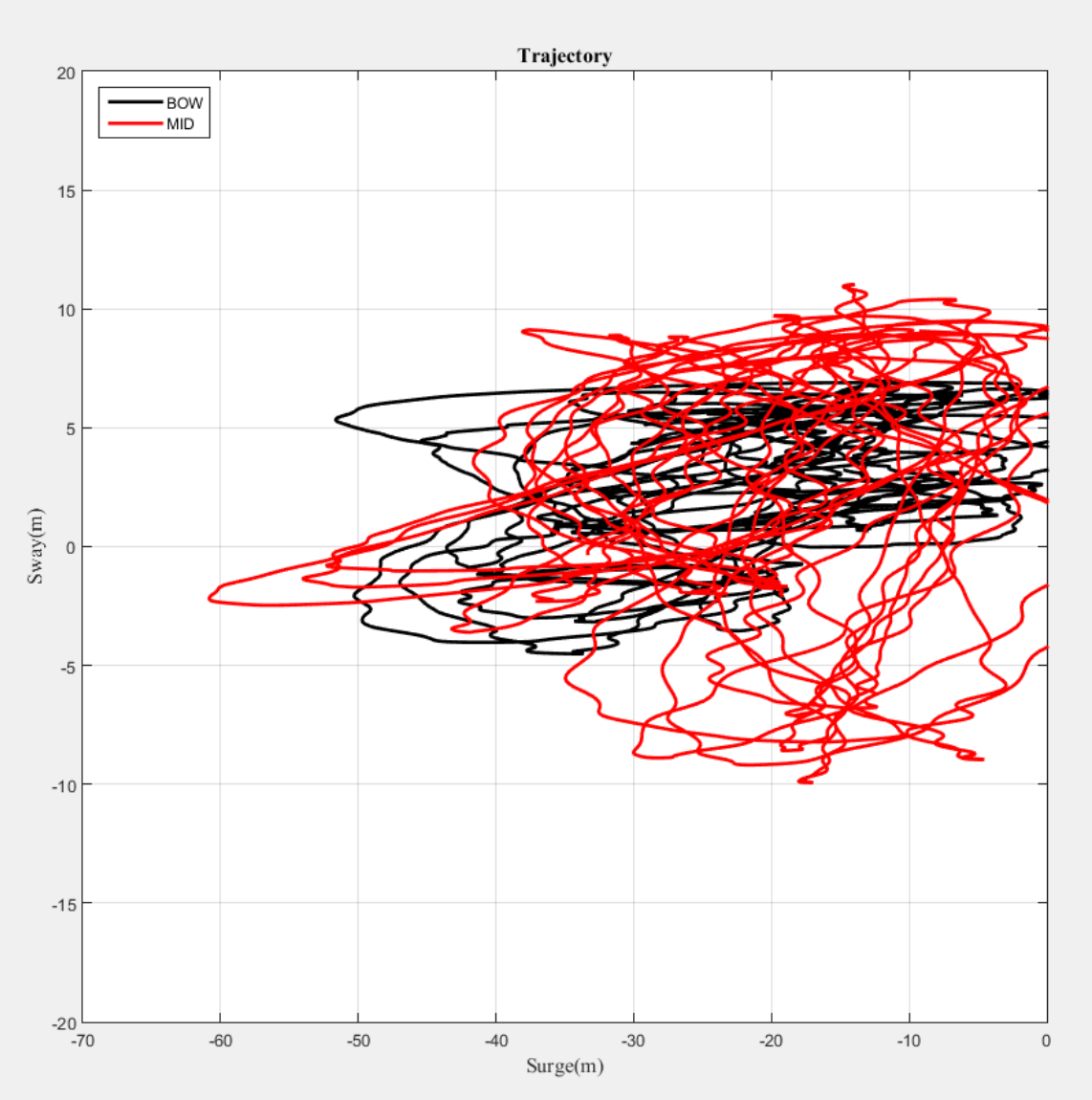

Figure 4.18 Surge-Sway Trajectory of the Bow and the Mid-Ship Turret in Gulf of Mexico 100-Year, Mooring-Only Simulation

In this section, we compare the global performance of the two turret positions in a particular non-collinear WWC condition. Figure 4.18 shows the surge-sway trajectory of FPSO without DP operation. Figure 4.19 presents FPSO 6DOF motions. The mid-turret

case shows larger excursions in both surge and sway directions compared to the bow-turret case. Particularly, the mid-turret case exhibits large dynamic yaw motions with largely deviated mean yaw angle. It means that the FPSO has to face waves coming with average-40-degree starboard angle. Considering additional slowly-varying yaw responses, the situation can be worse. This phenomenon can cause large variations of WWC loadings i.e. the advantage of weathervaning to minimize the environmental loadings becomes non-effective. So, despite the advantage of smaller vertical motions at the turret, this may be the reason why the mid-turret design is not popular mainly due to the reduced weathervane capability. This may be one of the reasons why the mooring system of the Gryphon FPSO failed even for storms less powerful than survival condition. On the other hand, the bow turret case is more likely to weathervane to the dominant environmental-loading direction.

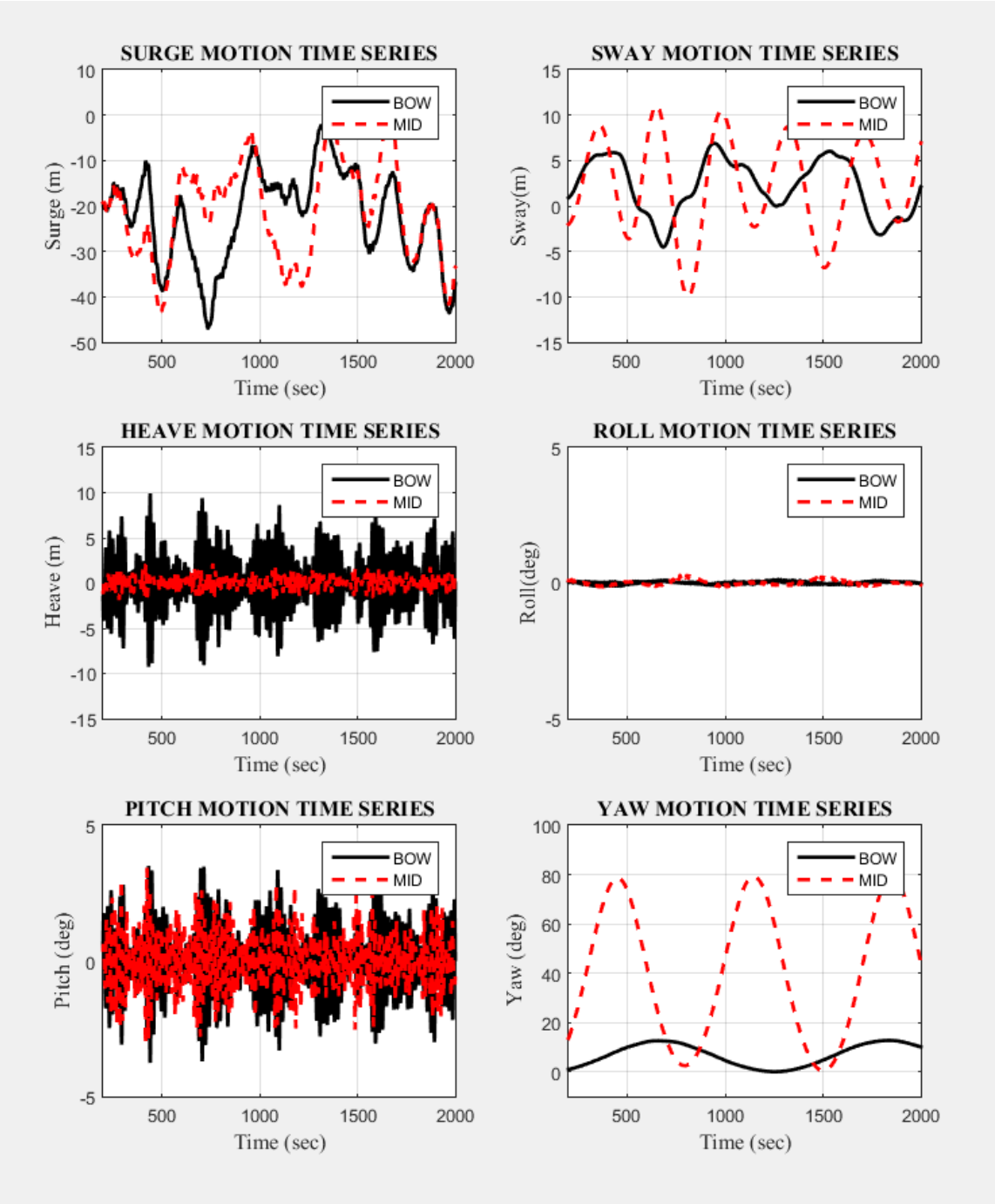

Figure 4.19 6DOF Motion of the Bow and the Mid-Ship Turret in Gulf of Mexico 100-Year, Mooring-Only Simulation

Figure 4.20 and 21 shows the time series of the fairlead mooring tension and riser tension of the bow and mid turret cases under GOM 100-yr non-collinear environment. The reduction of the maximum top tension in the mid-ship turret location is noticeable. Therefore, the advantage of mid-turret position in terms of mooring and riser design is still obvious even in the non-collinear environment except for the critical disadvantage of poorer weathervane capability. The poorer weathervane capability may be resolved by employing additional DP system, which is the subject of the next section.

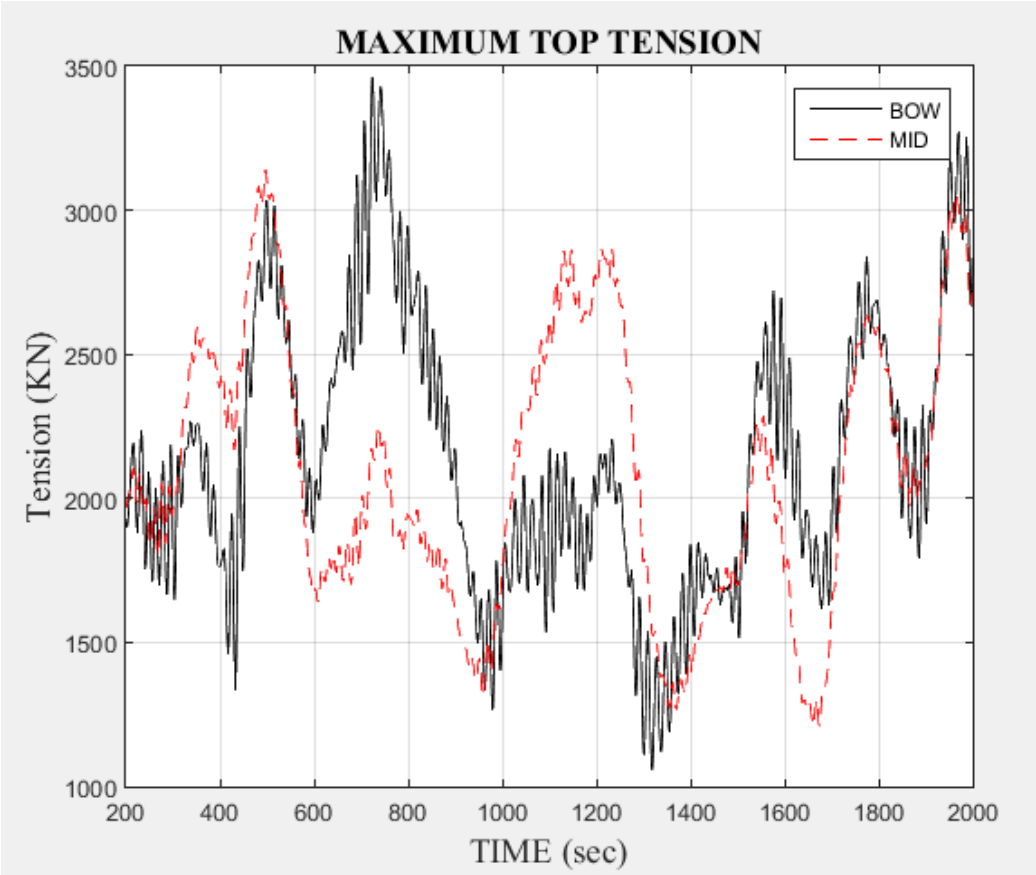

Figure 4.20 Maximum Top Tension of Moorings in Gulf of Mexico Noncollinear Environment (Mooring Only Case)

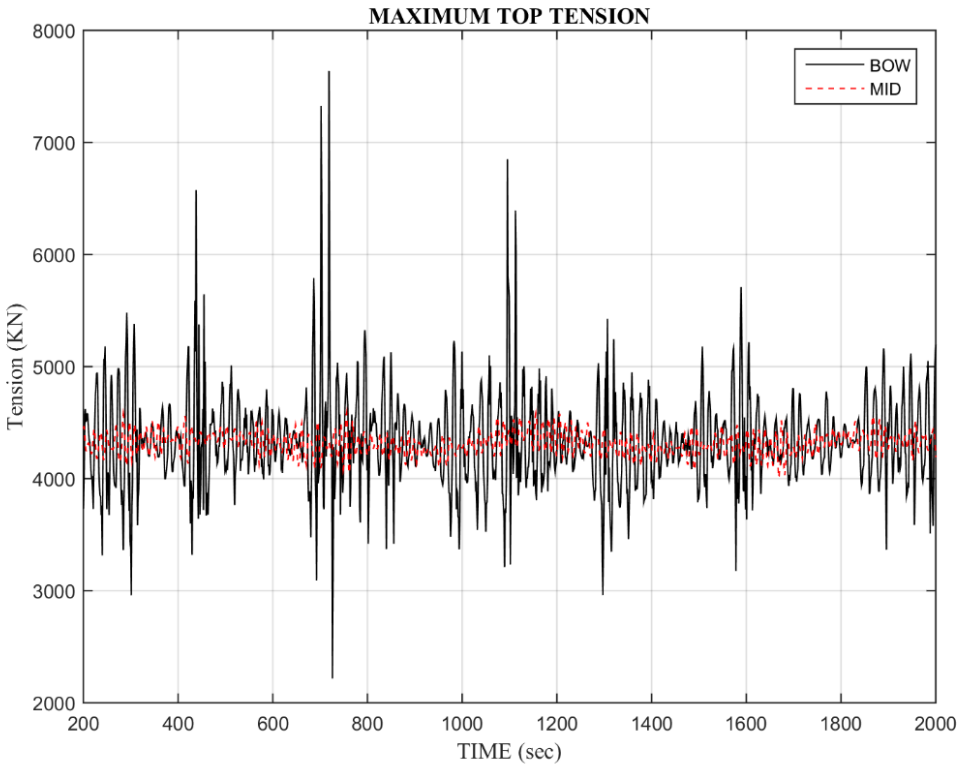

Figure 4.21 Maximum Top Tension of the Bow and the Mid-Ship Turret in Gulf of Mexico 100-Year, Mooring-Only Simulation

4.5.3 Gulf of Mexico 100-Year Scenario with DP and Without Heading Control

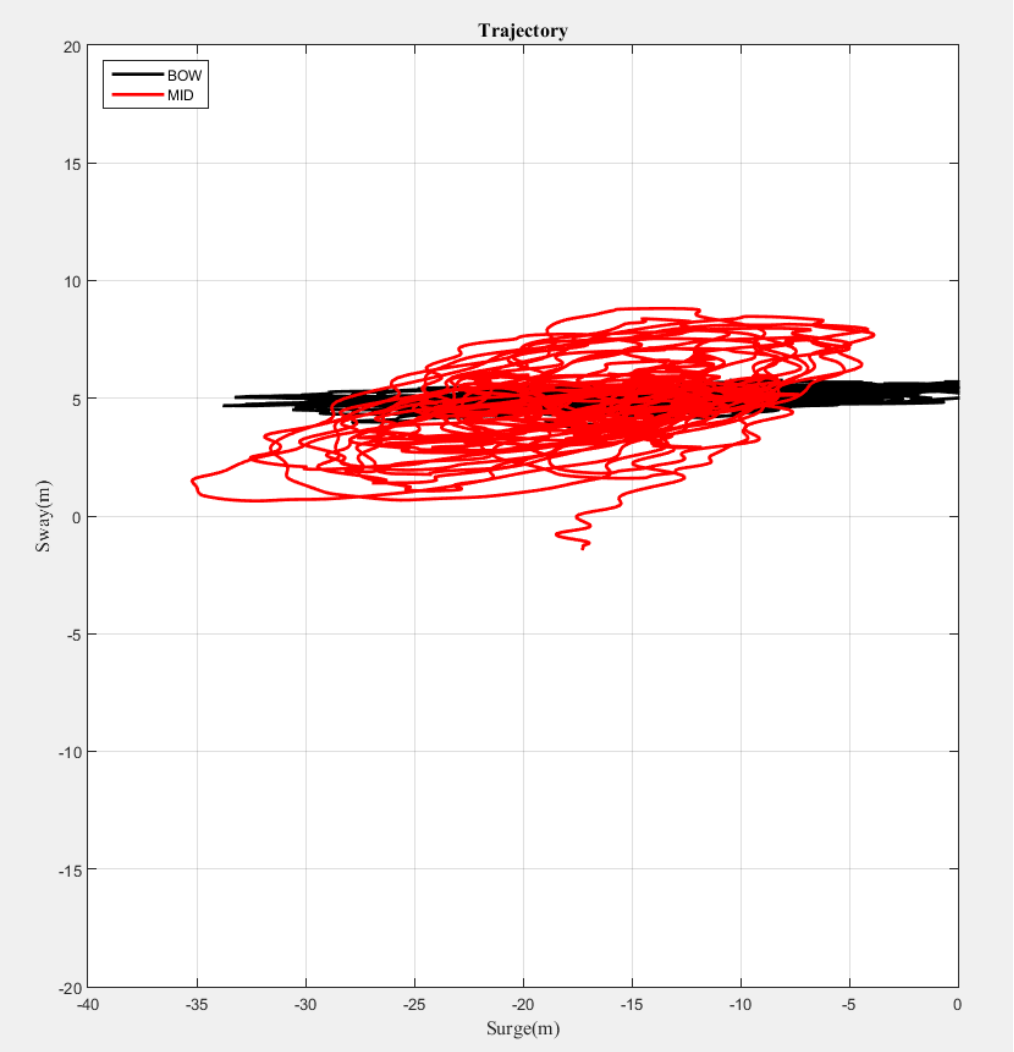

Figure 4.22 Surge-Sway Trajectory of the Bow and the Mid-Ship Turret in Gulf of Mexico 100-Year Simulation with DPS

Fig 4.22 shows the surge and sway trajectory of FPSO under the GOM 100-yr non-collinear environmental condition with the DPS. For this example, the position control is applied but heading control is not applied. The sway trajectory of the mid-ship turret case

is much reduced compared to Figure 4.18 but it is still larger than the bow-turret case. The main reason why the sway trajectory is reduced is that the DP counteracts the sway deviation. The dynamic yaw motions are also greatly reduced compared to Figure 4.19-yaw. This result implies that the mid-ship turret with DP is more practically applicable than w/o DP case. Despite the improvement by including the DP position control, the mean yaw angle is still around 40 degrees from the wave direction, which is not a desirable situation. Therefore, additional heading control by DP system is needed, as shown in the next section. Figure 4.23 shows the 6DOF motion time histories of the bow and mid-turret cases. The DPS makes the sway excursion smaller by 7 m.

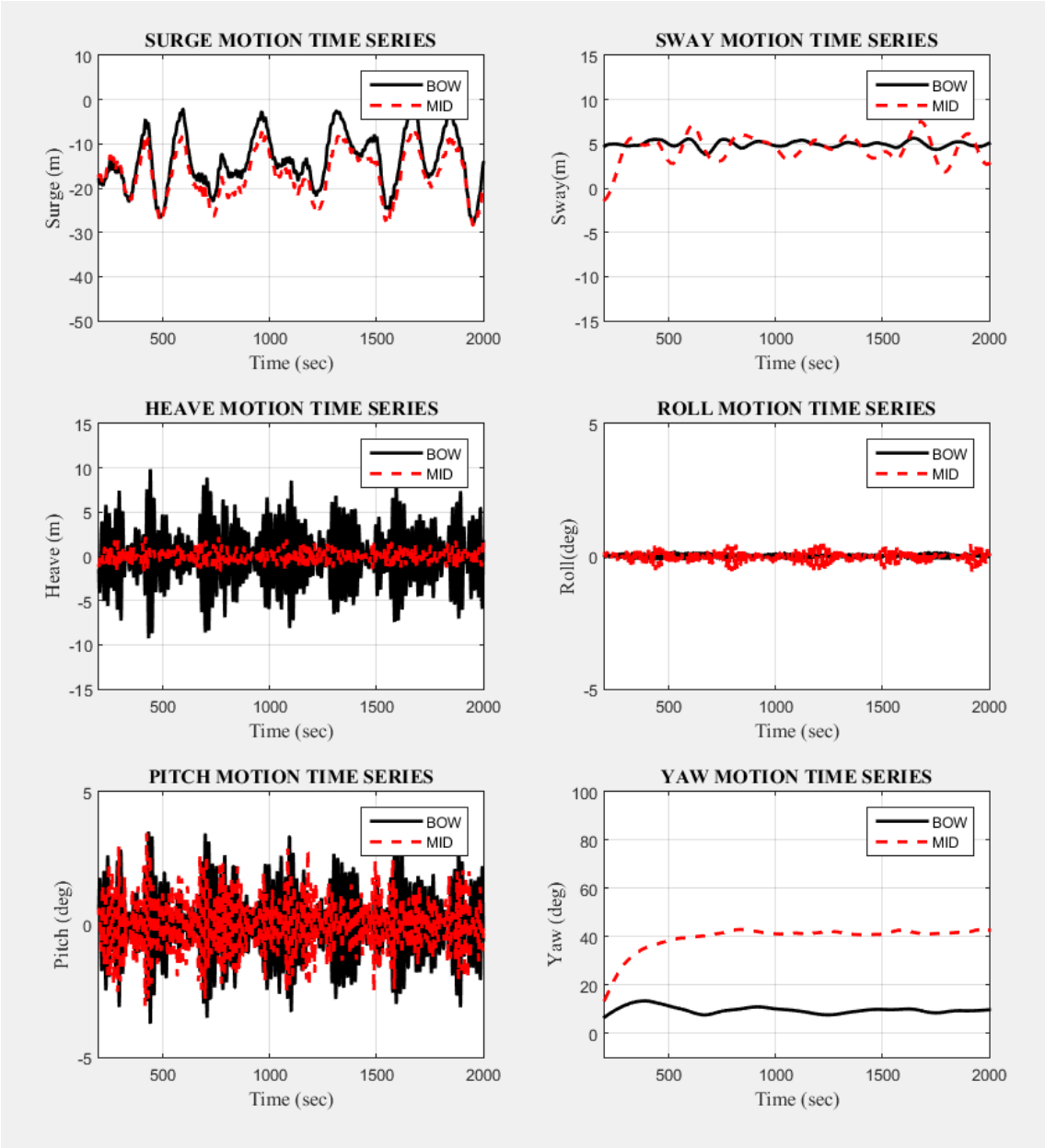

Figure 4.23 6DOF Motion Time Series of the Bow and the Mid-Ship Turret in Gulf of Mexico 100-Year Simulation with DPS

Figure 4.24 shows the fairlead mooring top tension of the bow and mid-turret cases. Compared to w/o DP system (Figure 4.20), the maximum top tension of the bow turret case was reduced from 3460 KN to 2940 KN. The maximum tension of the mid-turret case is also reduced from 3130 KN to 2960 KN with the DPS. According to the result, the sway induced force by large yaw angle makes the maximum tension of mid-turret approximately same amount of the bow turret. This results shows why the mooring failure occurred in the Gryphon incident because the heading control of mid-ship turret is critical.

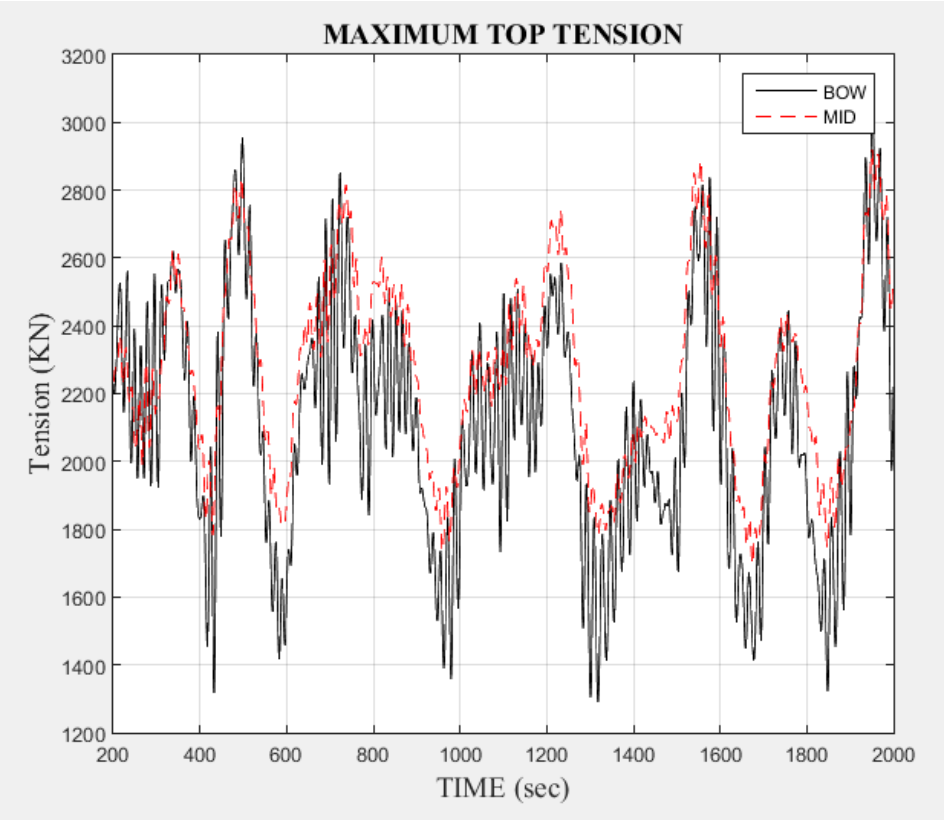

Figure 4.24 Maximum Top Tension of Mooring for the Bow and Mid-Turret Cases (with DP position control)

Figure 4.25 shows the fairlead riser top tension of the bow- and mid-turret cases. Compared to w/o DP system (Figure 4.21), the maximum top tension of the bow turret case was decreased from 8800 KN to 6200 KN. The maximum tension of the mid-turret case is also reduced from 4700 KN to 4500 KN with the DPS.

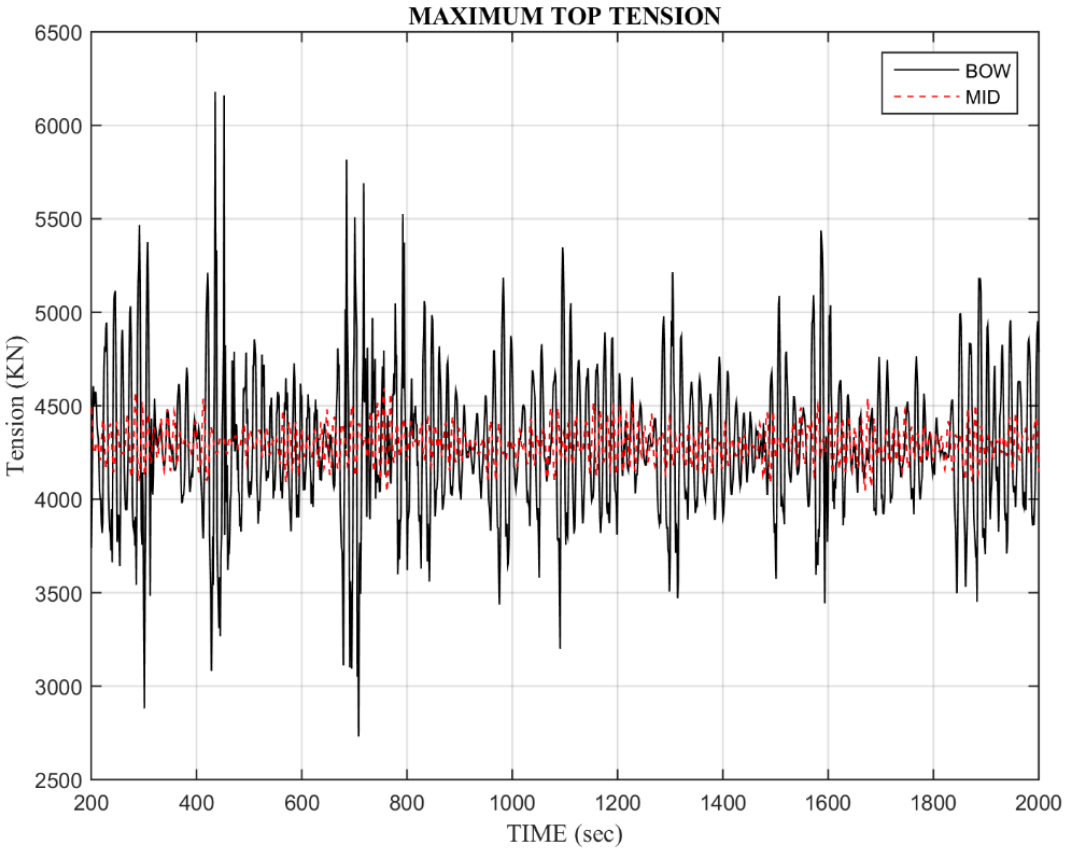

Figure 4.25 Maximum Top Tension of the Bow and the Mid-Ship Turret in Gulf of Mexico 100-Year Simulation with DPS

Figure 4.26 shows fuel-consumption time histories depending on turret locations. The fuel consumption formula as function of required power/thrust is given in Kim (2016).

According to the graph, the maximum fuel consumption of the mid-ship turret is appreciably (15%) larger than that of the bow-turret case. Finally, we next consider the same case with additional DP heading control.

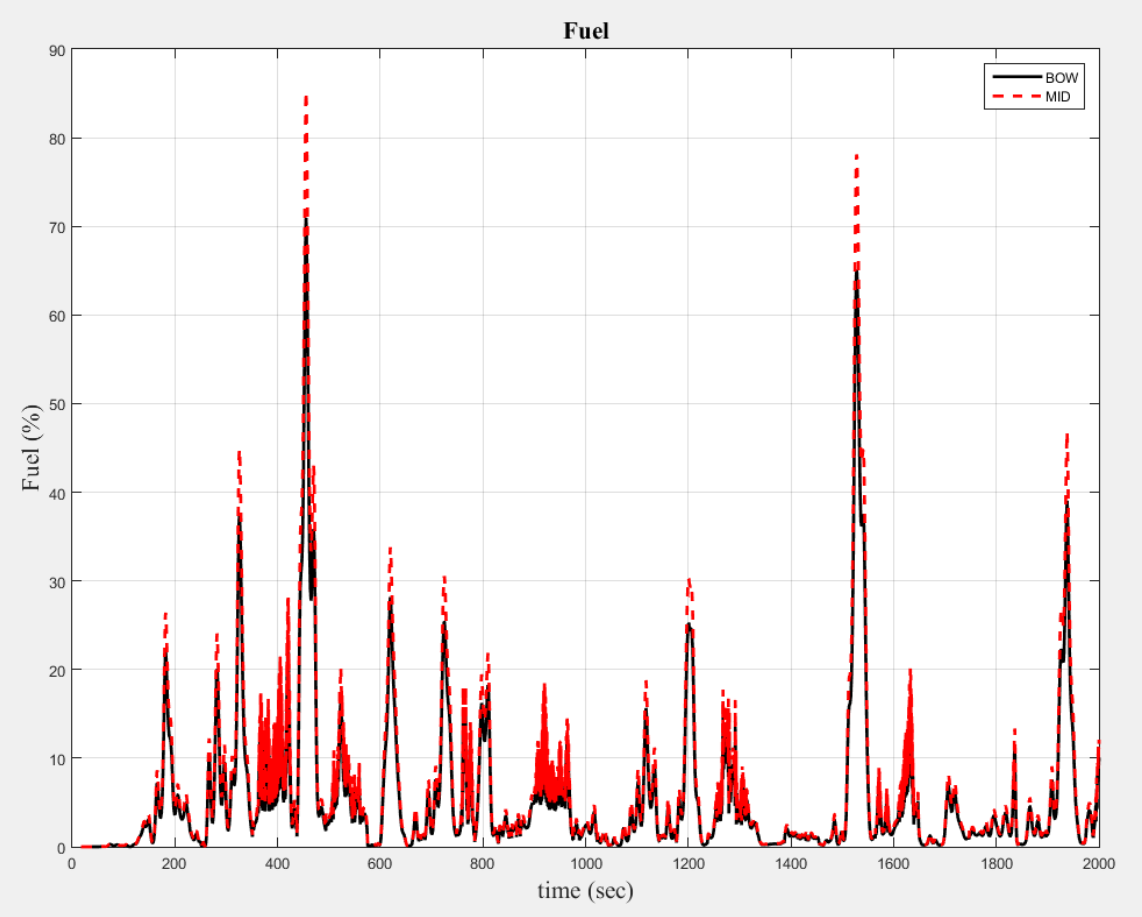

Figure 4.26 Fuel Consumption of Bow and Mid-Ship Turret in Gulf of Mexico 100-Year Simulation with DPS

Figure 4.27 shows the CO_2 amounts that were produced during the dynamic positioning operation. The peak of the bow turret location is lower than that of the mid-ship turret location by a maximum of 8%.

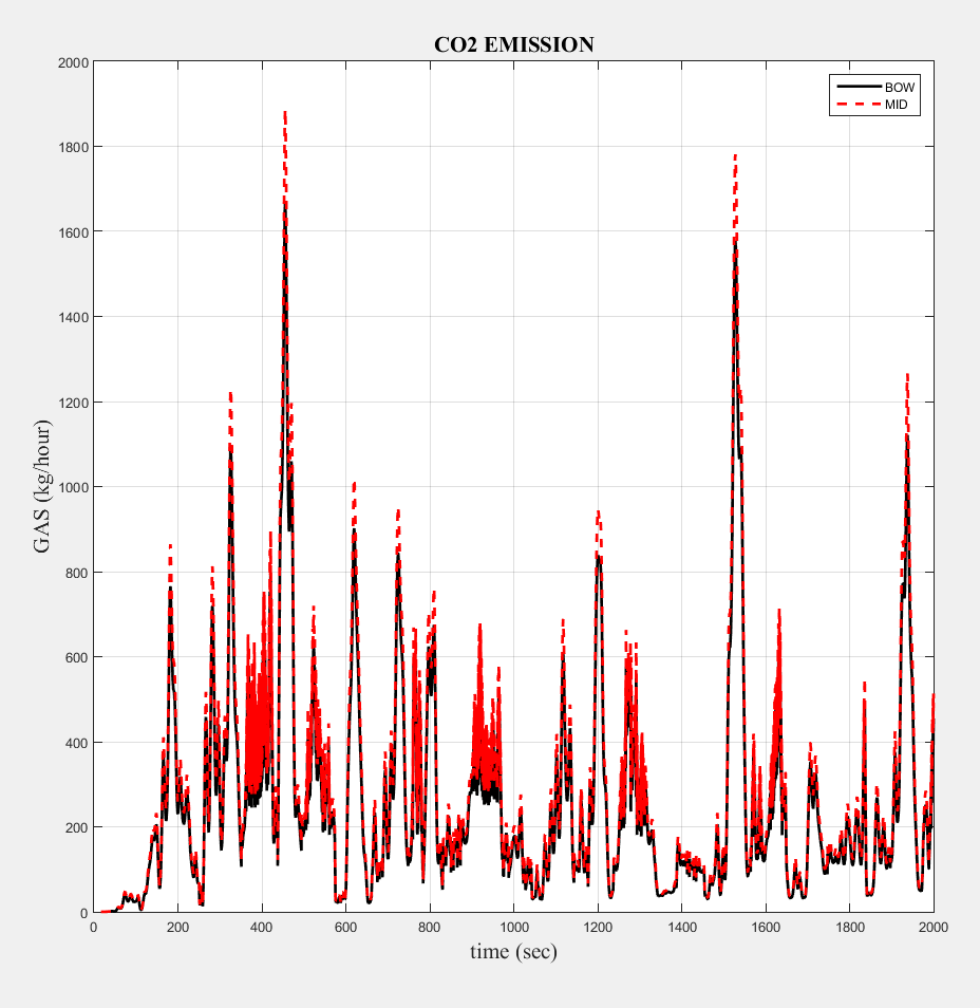

Figure 4.27 CO_2 Amount of Bow and Mid-Ship Turret in Gulf of Mexico 100-Year Simulation with DPS

4.5.4 Gulf of Mexico 100-Year with DP and Heading Control

Figure 4.28 shows the surge and sway trajectory of FPSO in the GOM 100-yr non-collinear environmental conditions when DPS is doing both position and heading controls. Figure 4.29 shows the 6DOF Motion Time Histories of the Bow and Mid-Turret Cases. The target heading direction in this case is zero-degree i.e. parallel to the wave direction. The sway deviations are much (by 5m) reduced compared to the previous cases. The main reason why the sway trajectory becomes smaller is that the DP maintains the heading close to the wave direction. The mean yaw angle of the mid-turret case is also greatly reduced from about 40 to 10 degrees compared to the DP position control only case. This implies that the mid-turret position can be advantageous to the mooring riser system when DP does both position and heading controls.

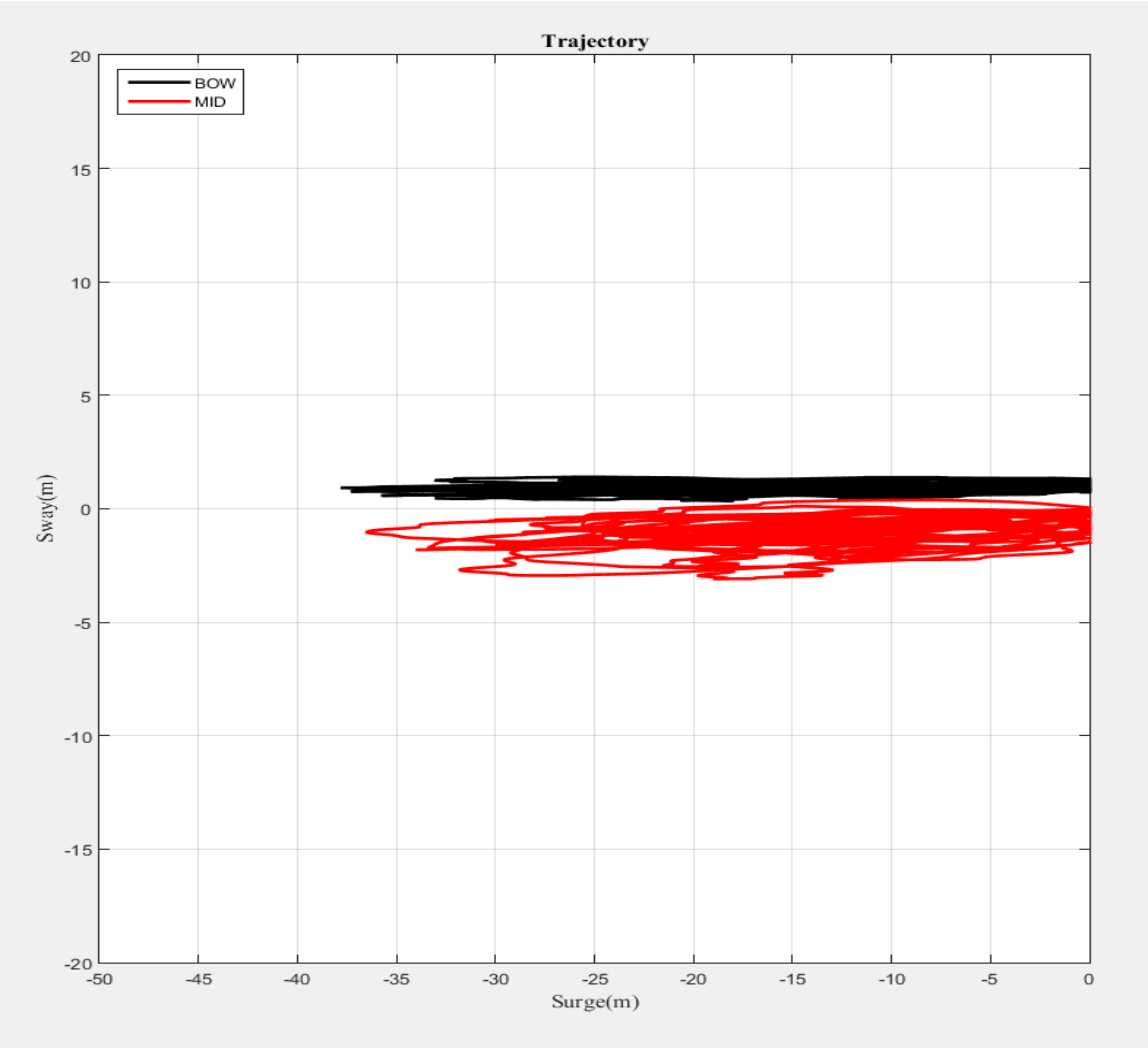

Figure 4.28 Surge-Sway in Gulf of Mexico 100-Year Conditions Simulation with DP Heading Control

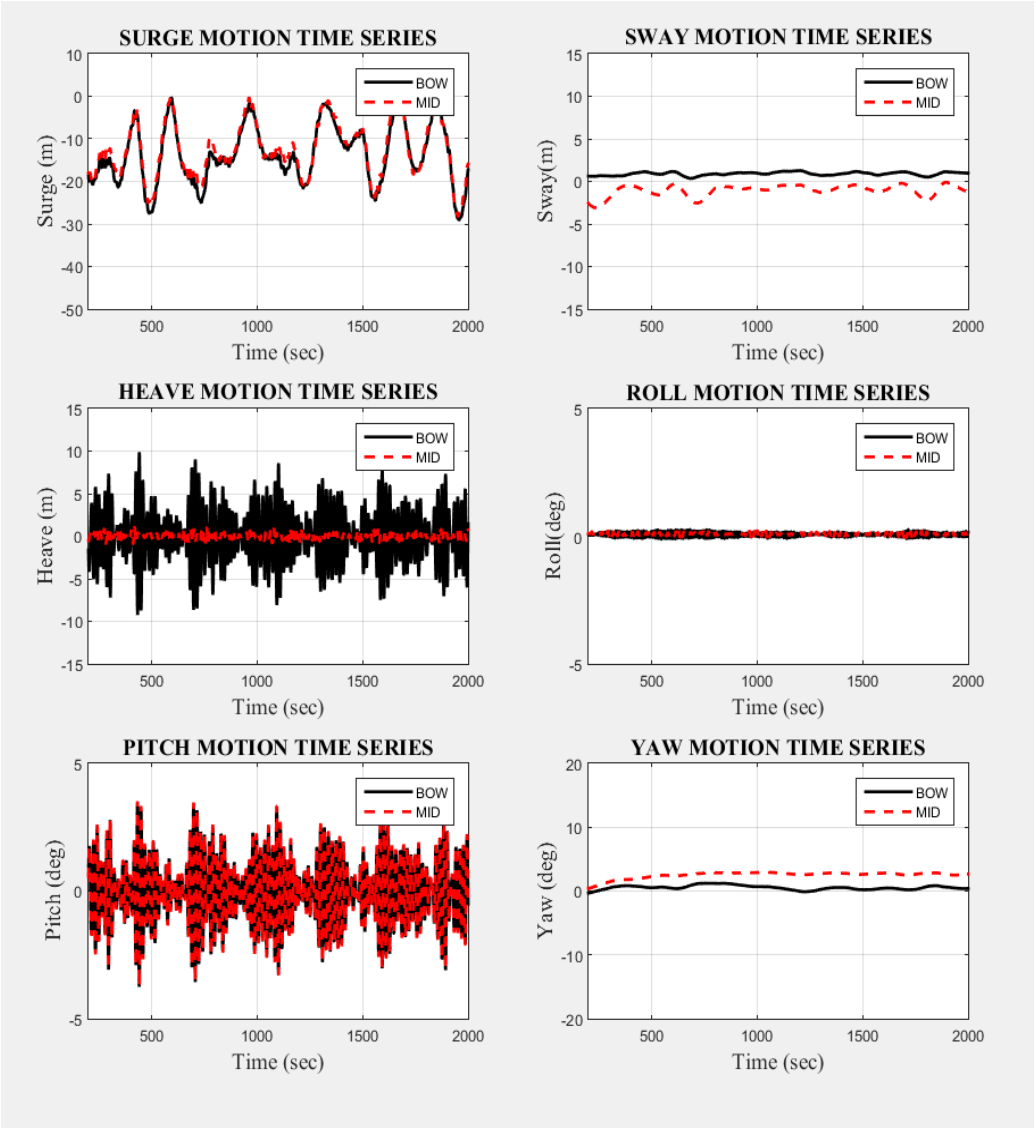

Figure 4.29 6DOF Time History under 100-Year Conditions with DP Heading Control

This Figure 4.30 shows the corresponding top-tension time histories. The maximum top tension of the bow turret case was reduced from 2940 KN to 2590 KN while that of mid-turret case is reduced from 2960 KN to 2370 KN with the additional DPS Heading Control. The mooring top tension was much enhanced by the DPS heading control.

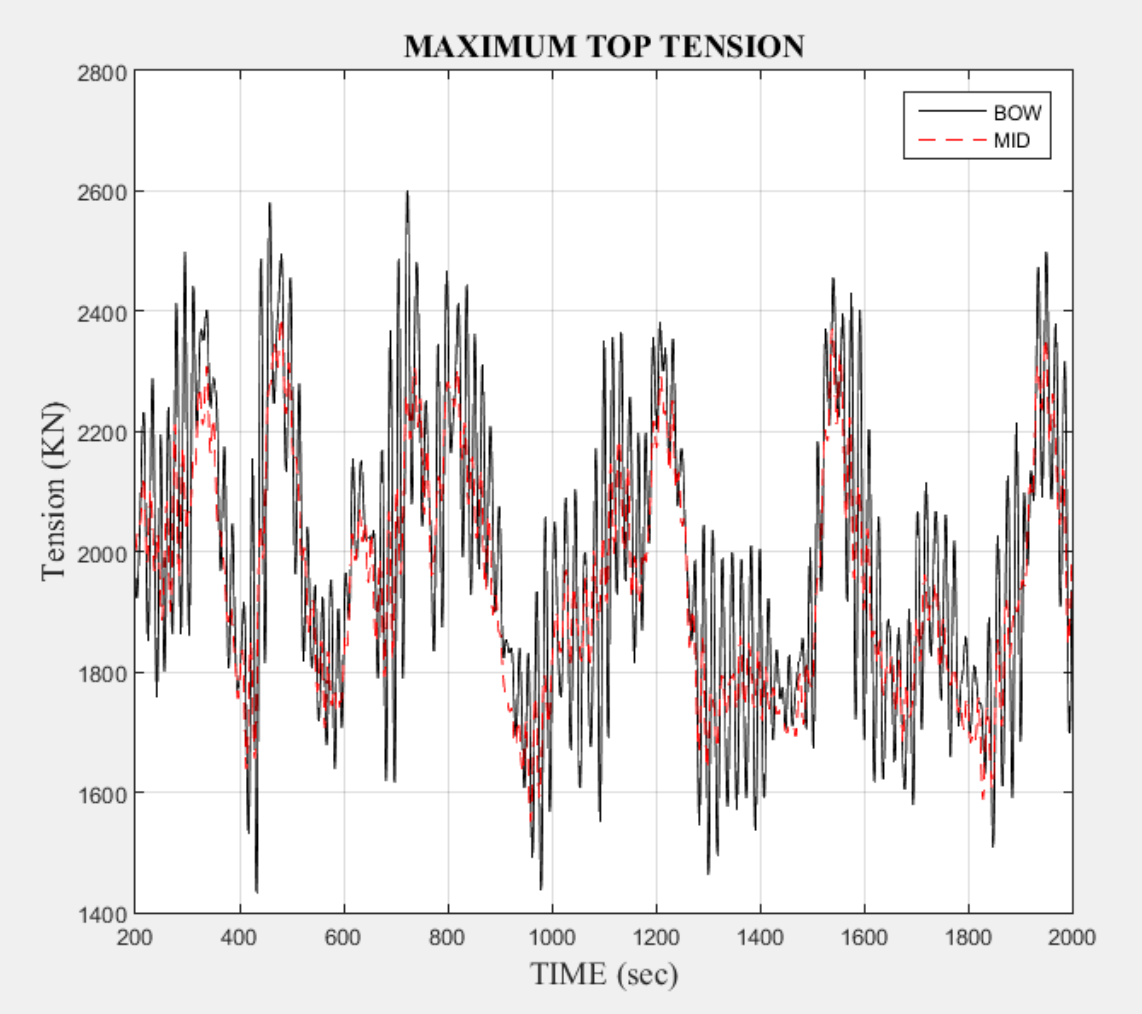

Figure 4.30 Maximum Mooring Top Tension of the Bow and Mid-Turret Cases in Gulf of Mexico 100-Year Noncollinear WWC with Additional DP Heading Control

This Figure 4.31shows the corresponding top-tension time histories. The maximum top tension of the bow turret case was reduced from 6200 KN to 6130 KN while that of mid-turret case is reduced from 4500 KN to 4410 KN with the additional DPS Heading Control.

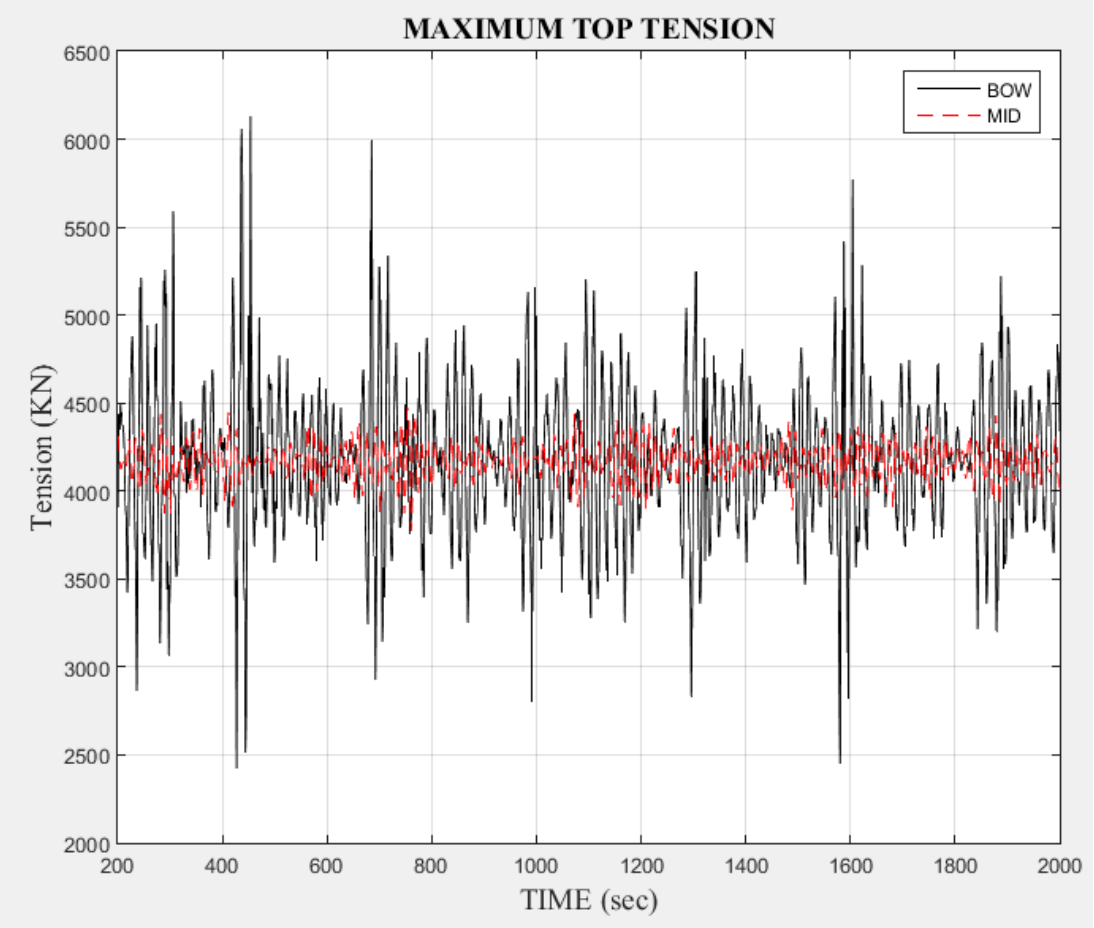

Figure 4.31 Maximum Riser Tension of the Bow and Mid-Turret Cases in Gulf of Mexico 100-Year Noncollinear WWC with Additional DP Heading Control

Figure 4.32 shows the fuel-consumption time history according to turret location. The red line is the mid-ship turret location. The black line is the bow turret location. Compared to the surge-sway-only control case, the fuel consumption was increased by 5%

accumulated value. This is because heading control requires more thrust than surge-sway control.

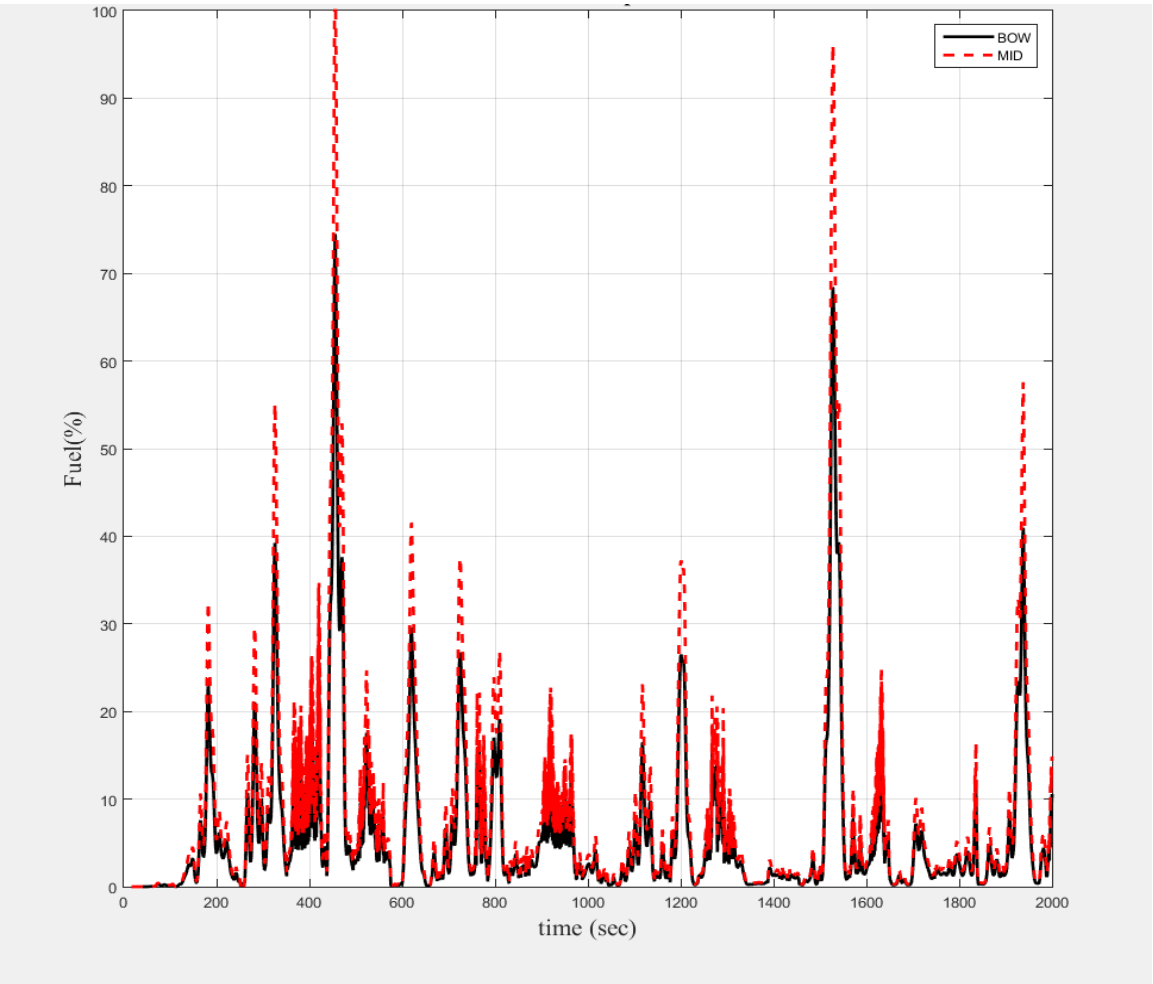

Figure 4.32 Fuel Consumption Index under 100-Year Conditions with DP Heading Control

Figure 4.33 presents the CO_2 time history according to turret location. The red line is the mid-ship turret location and the black line is the bow turret location. Compared to the surge-sway-only control case, CO_2 was increased by 3% accumulated value. This increase is because heading control requires more thrust than surge-sway control.

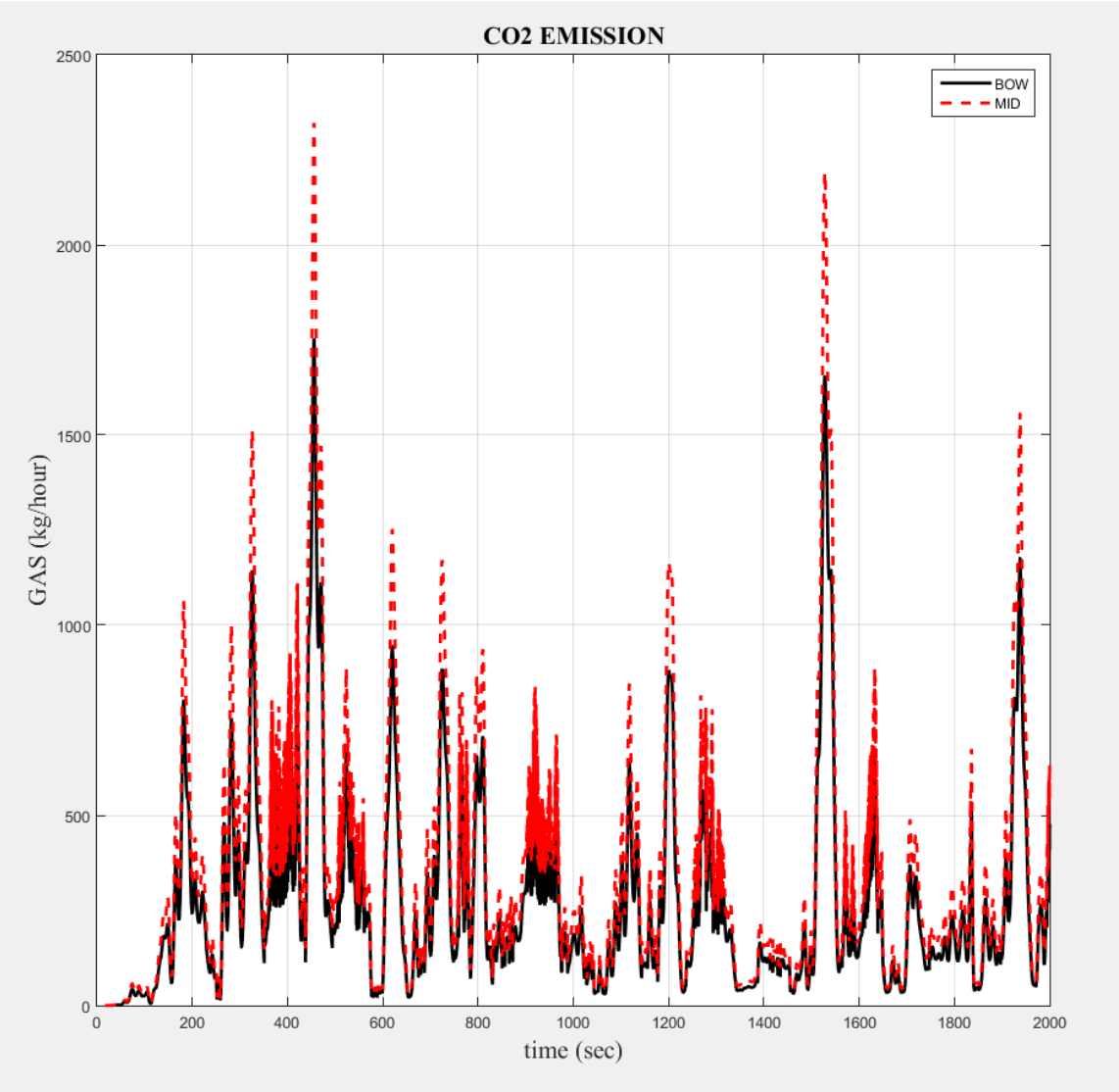

Figure 4.33 CO_2 under 100-Year Conditions with DP Heading Control

4.5.4 Gulf of Mexico One-Year Conditions with DP and without Heading Control

Next is an investigation of whether the previous conclusions are affected by different storm conditions. A simulation under GOM one-year storm conditions was conducted to analyze the change resulting from mild environmental conditions.

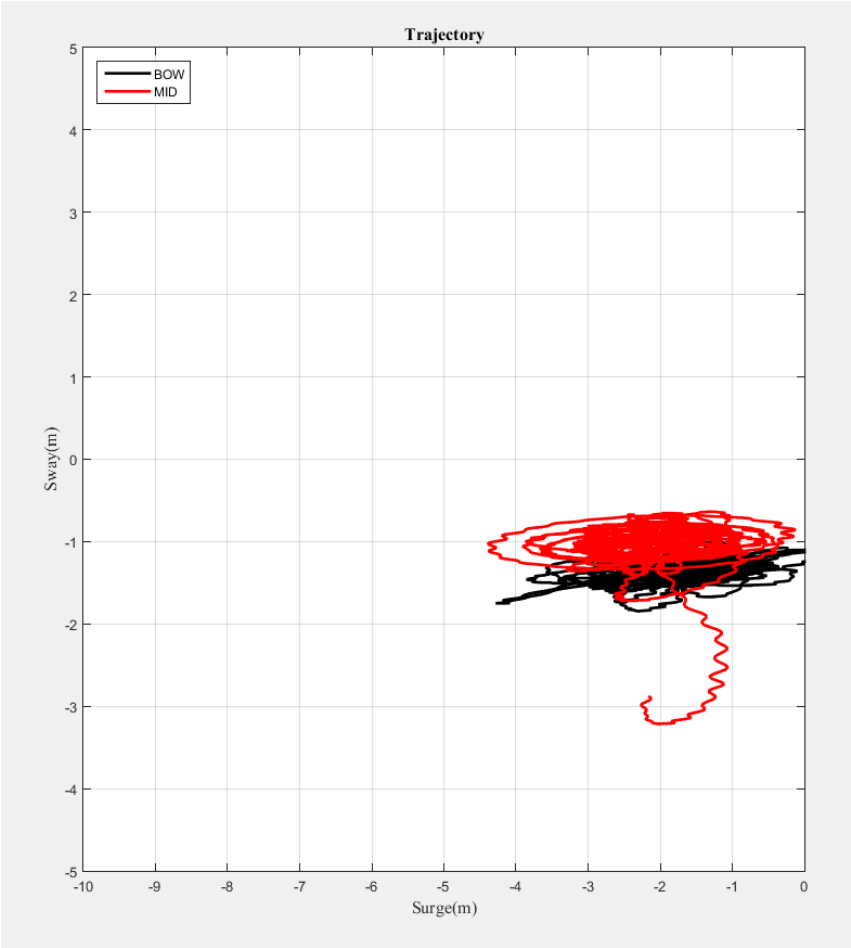

Figure 4.34 Surge-Sway Trajectory of Bow and Mid-Ship Turret in Gulf of Mexico One-Year Conditions with DPS

Figure 4.34 shows the surge and sway trajectory of the FPSO under GOM 100-year, noncollinear environmental conditions. The trajectory of the mid-ship turret location is much reduced in sway direction, even though it is still big compared to the bow turret location.

Trajectories by two different turret locations are presented in Figure 4.34. The watch circle is under 5m because the environmental force is much smaller compared to GOM 100-year conditions. The mid-ship turret location indicates horizontal instability.

Figure 4.35 shows 6DOF motion results of DP control due to turret location. The simulation results continue to show heave motion reduction in the mid-ship turret location, but in very small amounts.

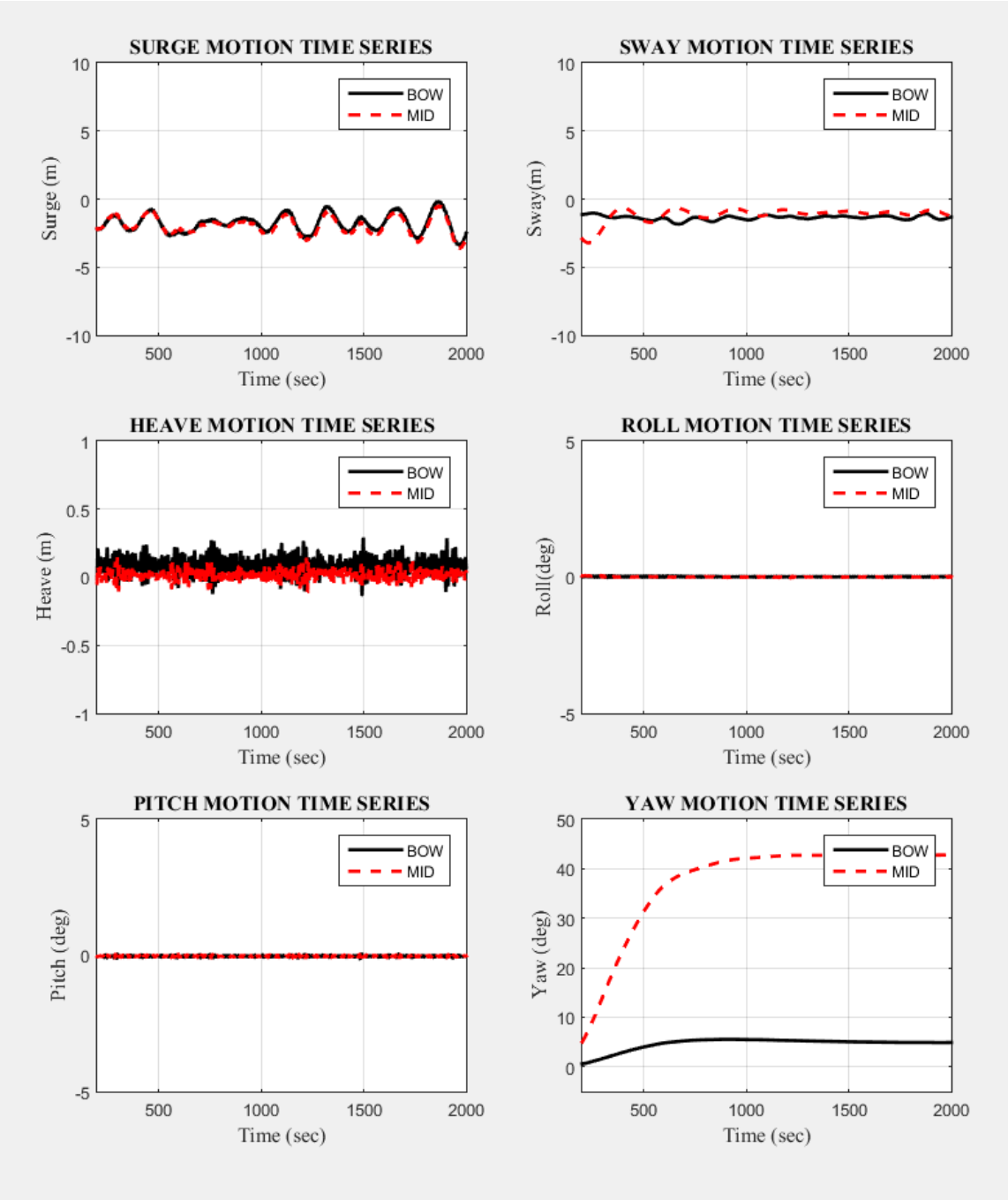

Figure 4.35 6DOF Time Series of Bow and Mid-Ship Turret in Gulf of Mexico One-Year Conditions with DPS

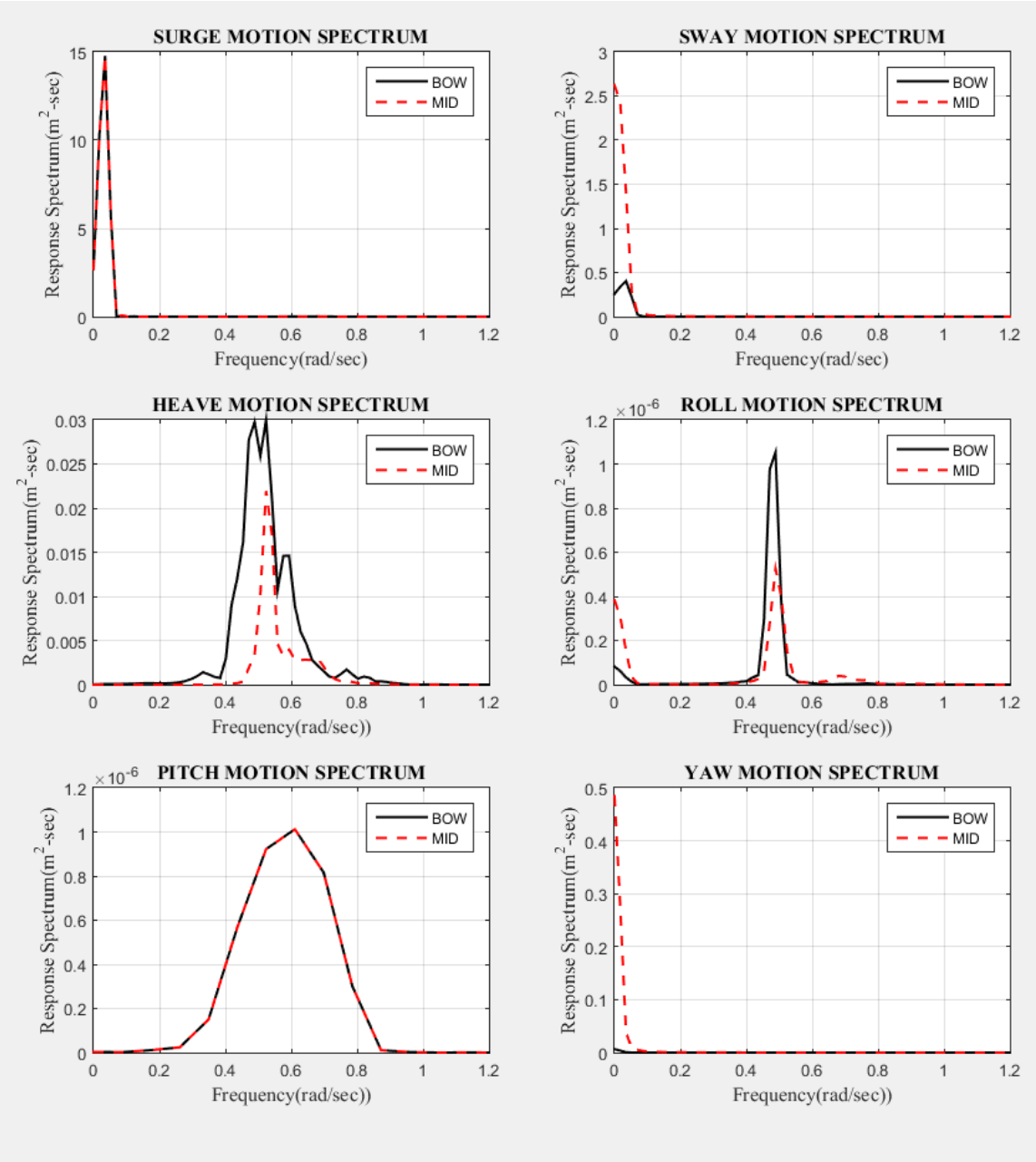

Figure 4.36 6DOF Motion Spectrum of Bow and Mid-Ship Turret in Gulf of Mexico One-Year Conditions with DPS

Figure 4.37 shows the maximum top tension due to turret location. The simulation results still show a heave motion reduction in the mid-ship turret location, but this became very small. The maximum tension of the mid-ship turret placement is about 4% smaller than that of the bow turret placement.

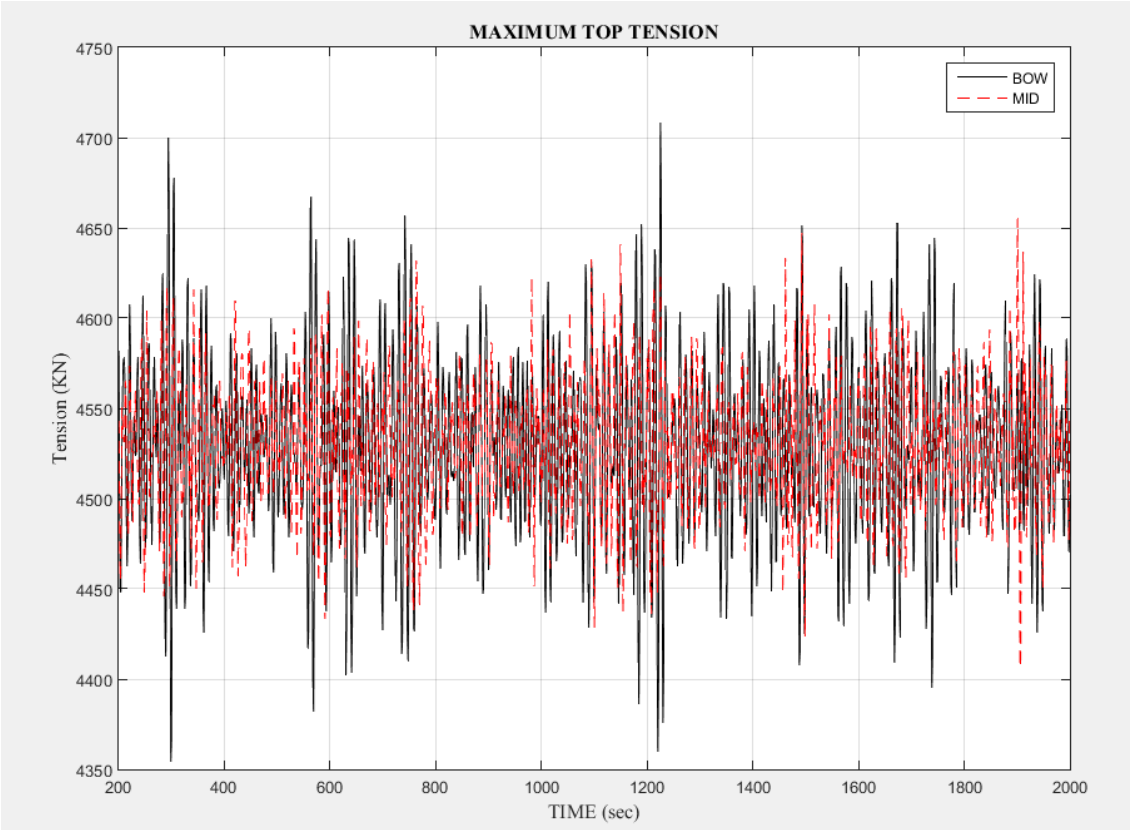

Figure 4.37 Maximum Top Tension of Bow and Mid-Ship Turret in Gulf of Mexico One-Year Conditions with DPS

Figure 4.38 shows fuel consumption amounts resulting from turret position in GOM one-year conditions. The peak of the bow turret is a maximum of 6% lower than that of the mid-turret location.

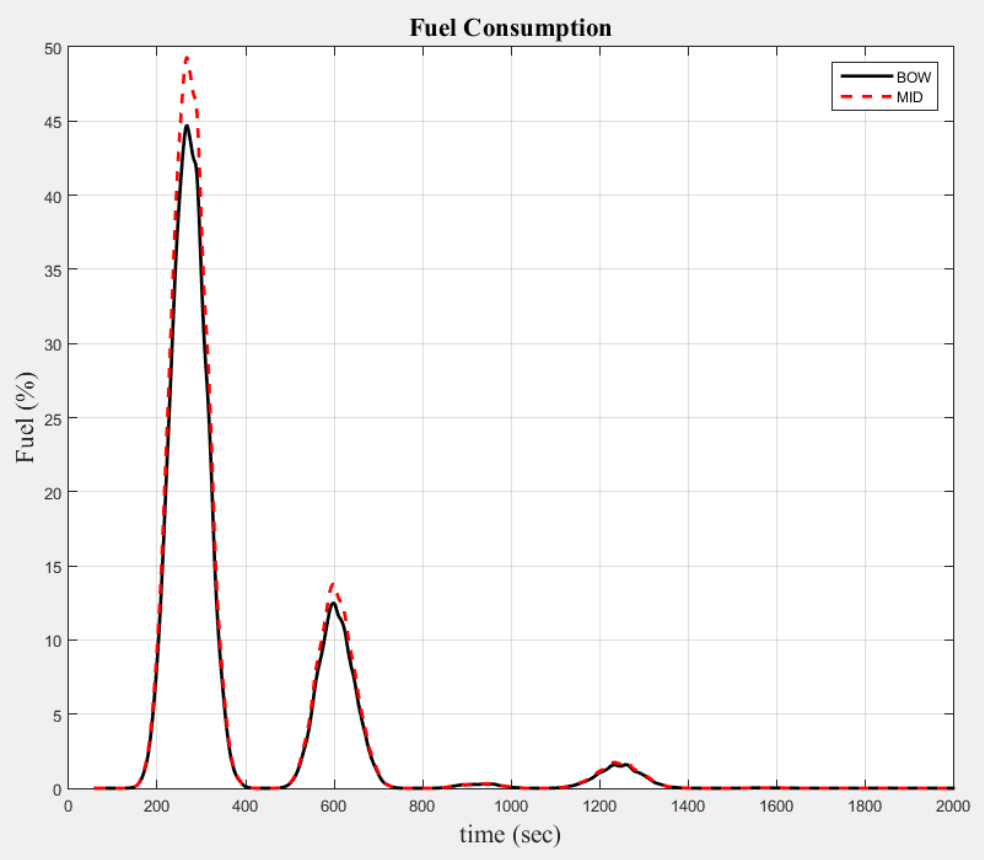

Figure 4.38 Fuel Consumption of Bow and Mid-Ship Turret in Gulf of Mexico One-Year Conditions with DPS

Figure 4.39 shows the CO_2 amounts produced during the dynamic positioning operation under GOM one-year conditions. The mid-ship turret location generated 3% more compared to the bow turret location.

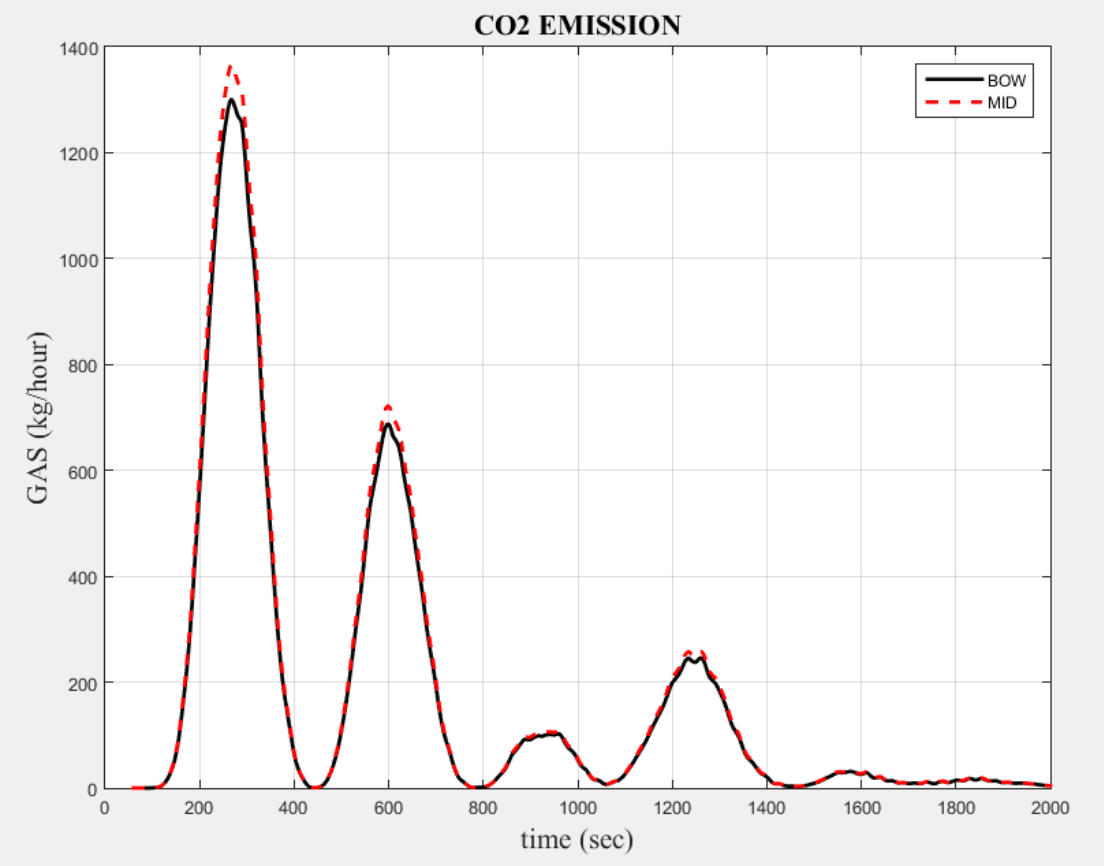

Figure 4.39 CO_2 Amount of Bow and Mid-Ship Turret in Gulf of Mexico One-Year Conditions with DPS

4.5.5 Gulf of Mexico One-Year Conditions with DP and Heading Control

Figure 4.40 shows the surge-sway trajectory of the bow and the mid-turret locations when those employ the DPS, including heading control. The mid-turret design surge-sway trajectory is quite comparable with the bow turret design with heading-control DPS.

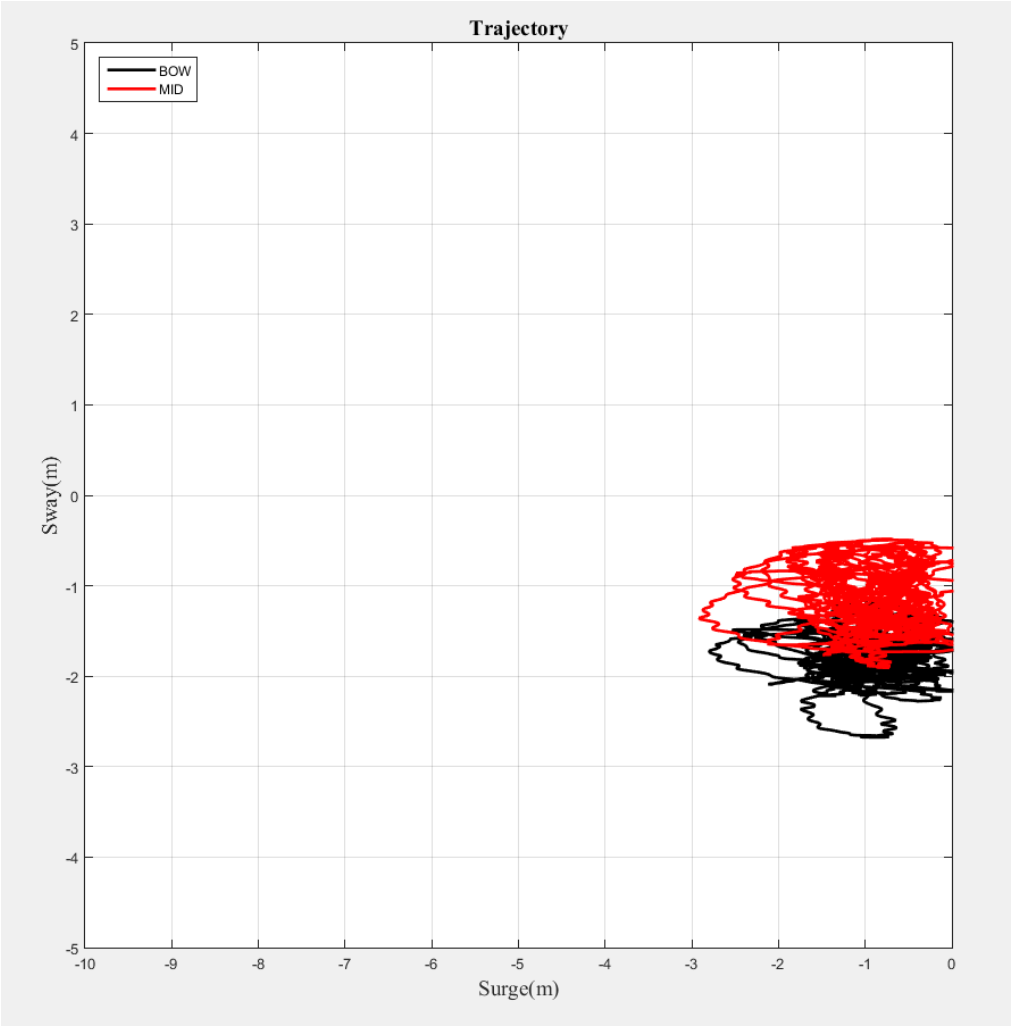

Figure 4.40 Horizontal Trajectories of the Bow and Mid-Turret with DP Heading Control

Figure 4.41 shows the 6DOF motion time history. The yaw motion of the mid-ship turret location with heading control was much reduced compared to surge-sway only control. It changes from 40 degrees in the surge-sway control to 1.5 degrees in the heading control case.

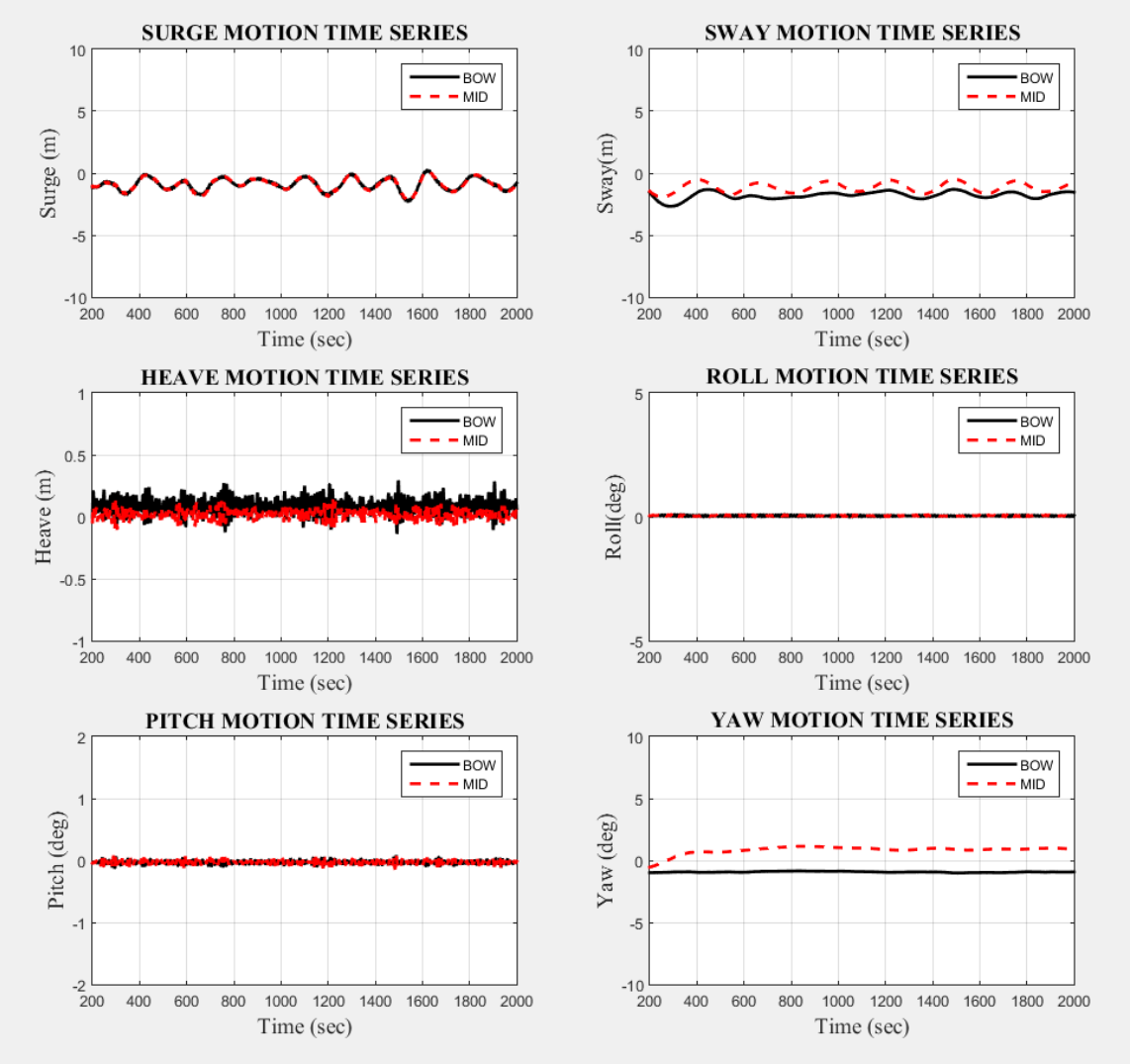

Figure 4.41 6DOF Horizontal Trajectories of Bow and Mid-Turret with DP Heading Control

Figure 4.42 presents the 6DOF spectra. The yaw motion spectrum was much reduced compare to the surge-sway control only.

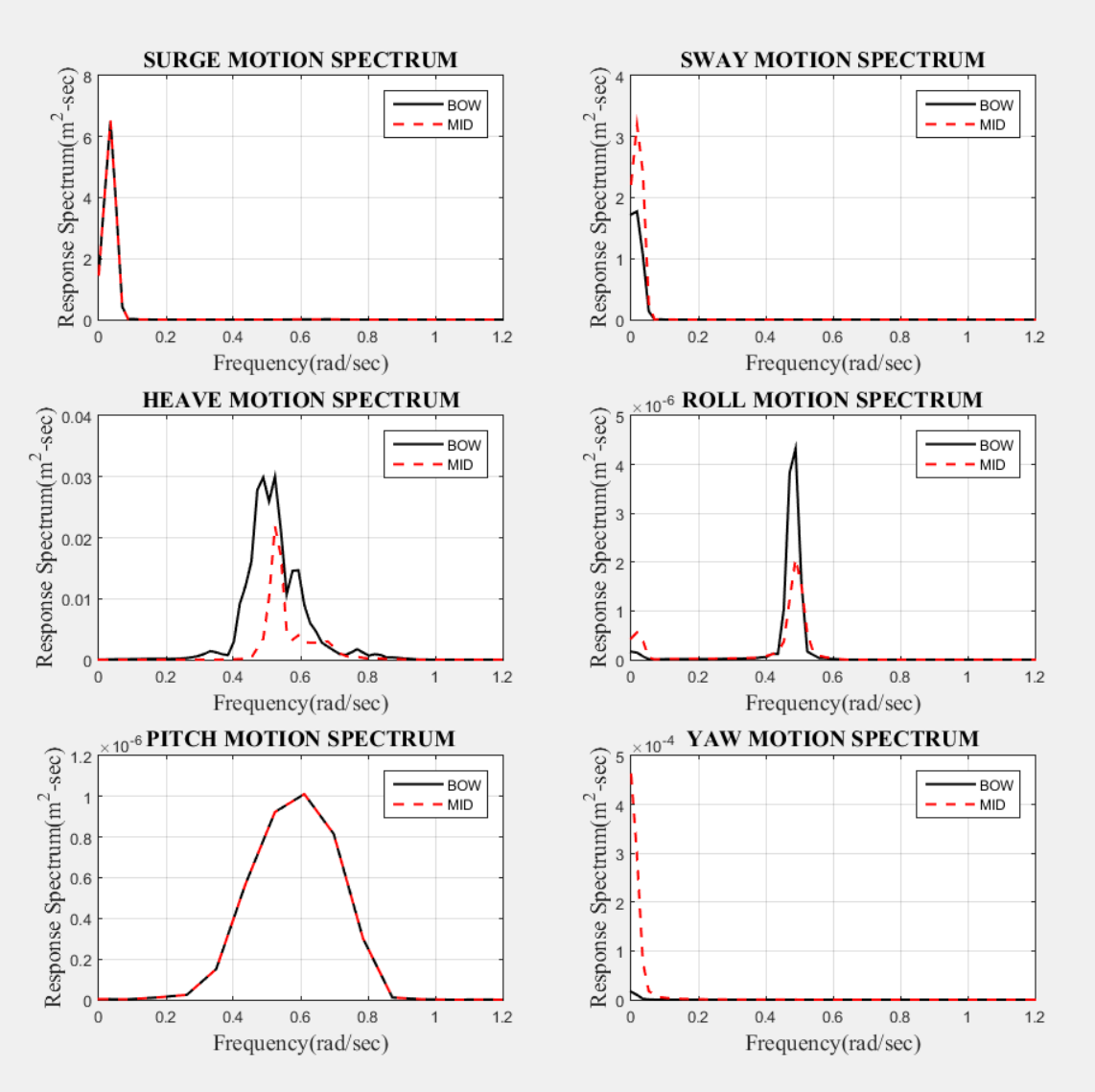

Figure 4.42 6DOF Spectra of Bow and Mid-Turret Simulation with DP Heading Control

Figure 4.43 presents fuel consumption under GOM one-year storm conditions with the heading control. The peak of the mid-ship turret is 12% larger than that of the bow turret. This phenomenon underscores the fact that the mid-ship turret design needs much thrust.

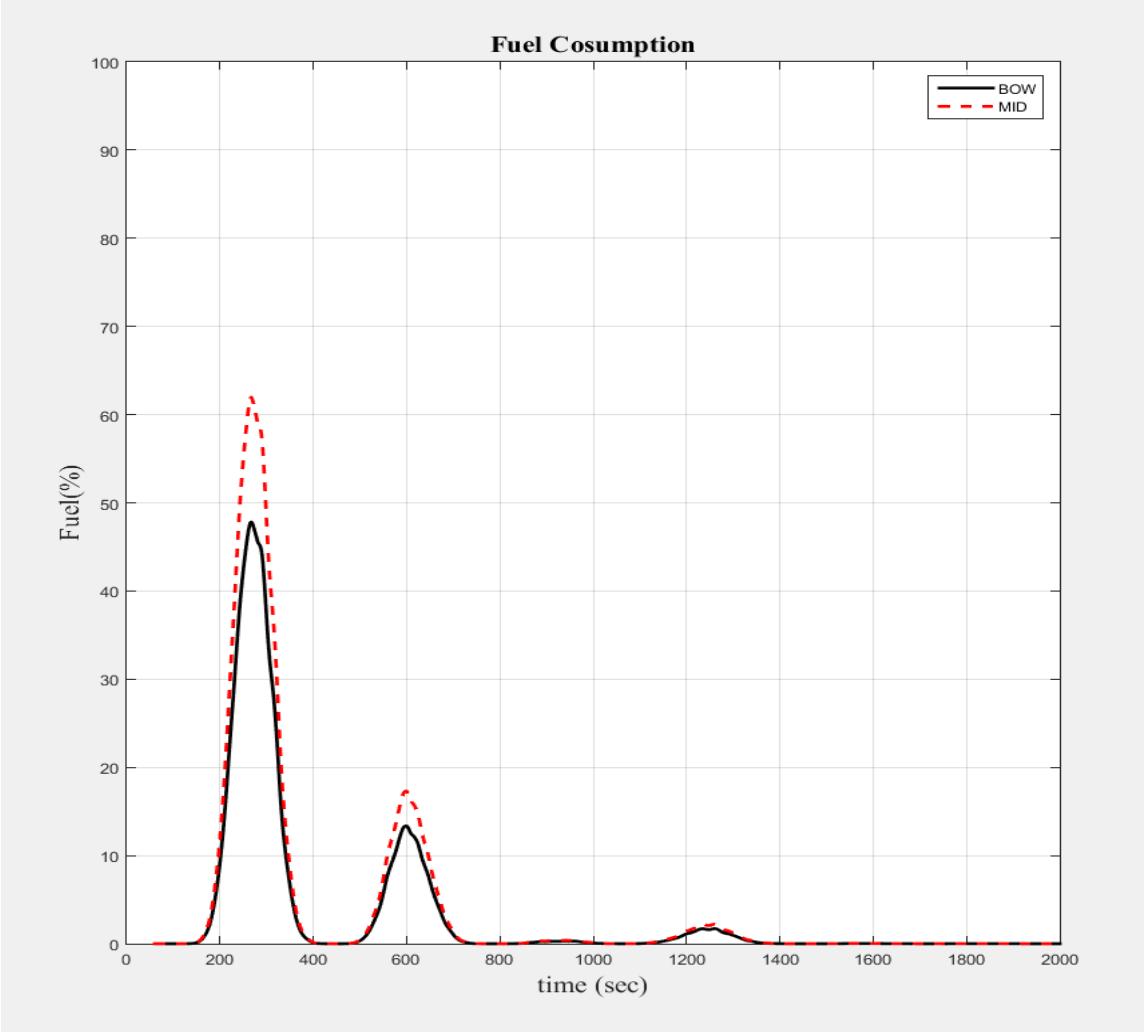

Figure 4.43 Fuel Consumption Index of Bow and Mid-Turret Simulation with DP Heading Control

Figure 4.44 shows the CO_2 amounts that were emitted using heading control DPS under GOM one-year conditions. The mid-ship turret location generates 7% greater CO_2 compared to the bow turret location.

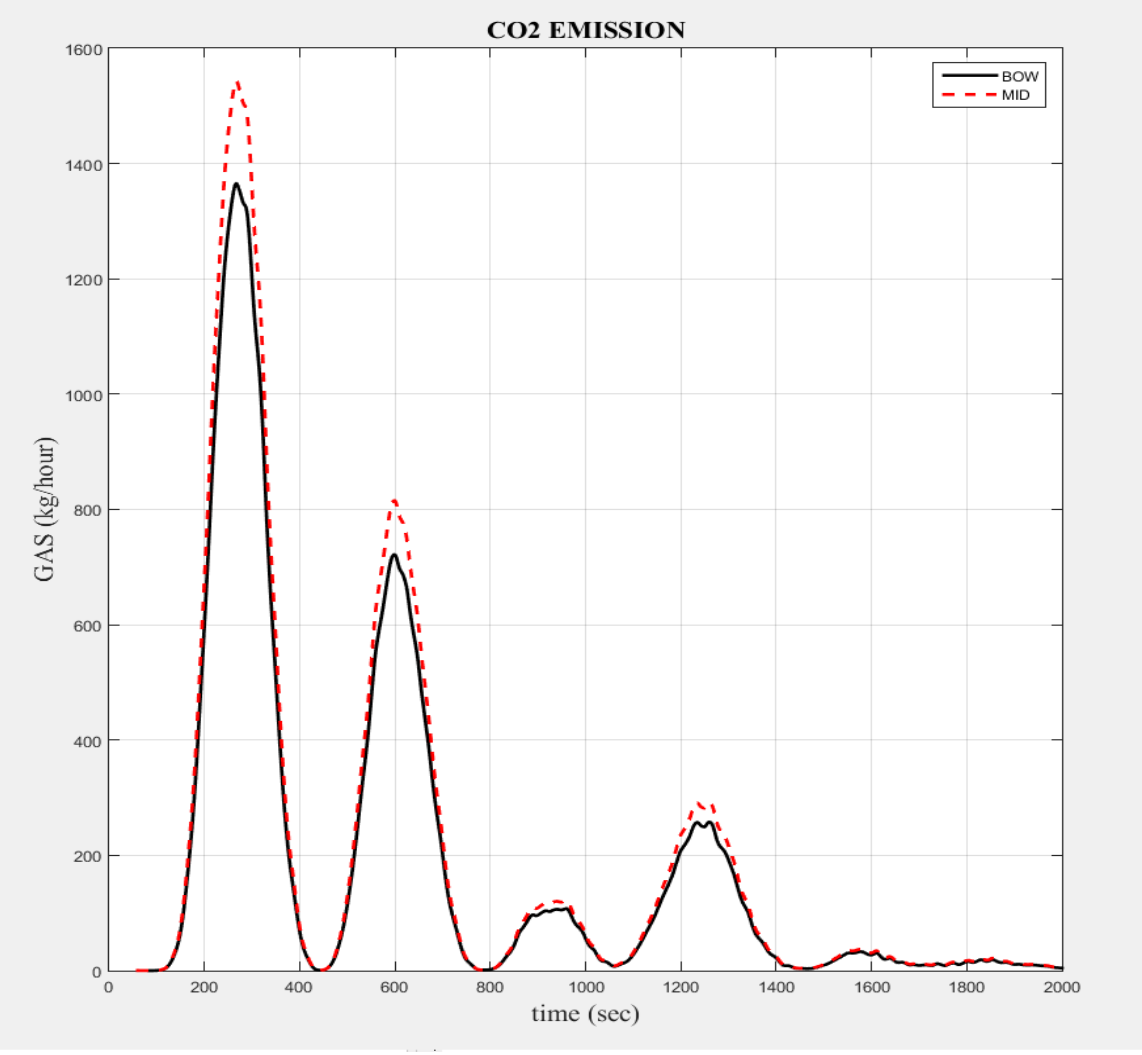

Figure 4.44 Fuel Consumption Index of Bow and Mid-Turret Simulation with DP Heading Control

4.6 Conclusion

The change of the global performance of a turret-moored FPSO with DP control was analyzed and compared for two internal turret positions; bow and midship. Both collinear and non-collinear 100-yr GOM storm environments were considered. Three cases (mooring-only, with DP position control, with DP position+heading control) were analyzed. The PID controller based on LQR theory and the thrust-allocation algorithm which is based on the penalty optimization theory were implemented in the time-domain hull-motion with DP control simulation program.

In collinear WWC environment, the advantage of mid-ship turret was demonstrated by the significant reduction in heave at the turret position due to the minimal coupling with pitch mode. However, in non-collinear WWC environment, the mid-turret case, despite the same advantage in heave reduction, case exhibited unfavorable position control and weathervaning characteristics. The disadvantage of the mid-turret case, however, can significantly be reduced by employing DP position and heading controls, as demonstrated in the present case studies, while keeping the advantage of much smaller vertical motions and maximum mooring tensions at turret position. The fuel consumption of the DPS is higher in the case of mid-turret.

In conclusion, the mid-turret case is better than the bow-turret case in terms of mooring and riser design but it has to work with proper DP position+heading control. Otherwise, it may have the risk of weathervaning malfunction in non-collinear environment, which actually happened in the failure of Gryphon FPSO.

CHAPTER V

TANDEM-OFFLOADING DYNAMIC POSITIONING SYSTEM APPLICATION

5.1 Introduction

The FPSO and shuttle tanker combination is the general concept for floating offshore oil production and transportation units. FPSO is moored in deep water. Periodically, shuttle tankers are linked to the FPSO in order to deliver their stored oil to shore. Tandem and side-by-side formations typically are used for this multi-body offloading configuration. Tandem offloading could be used under harsher environmental conditions than side-by-side offloading because its relative vertical motion is small. Nevertheless, the tandem configuration requires sufficient distance to avoid collision. The possibility of collision is present in both concepts; therefore, positioning devices are vital. Mooring and dynamic positioning systems are the basic equipment used for positioning operations. Typically, mooring is employed for FPSO. The DPS is applied to shuttle tankers because FPSO keeps a fixed position, but shuttle tankers periodically transport oil to shore, making the DPS more beneficial than the mooring system, which requires significant investments of time and funds to install.

In this dissertation, a six degrees of freedom, fully-coupled, hull-mooring-riser, multi-body, time-domain simulation was conducted using real-time, domain dynamic positioning control in a shuttle tanker. In addition, FPSO and the shuttle tanker were simulated together under West African environmental conditions and Gulf of Mexico one-year storm conditions.

5.2 Literature Review

Chen and Moan (2004) studied the occurrence of collisions under tandem configurations due to excessive horizontal motion. According to the International Maritime Contractor Association (IMCA) database, a total of 60 incidents of tandem offloading operations, related to position-keeping devices, occurred over a five-year period (Chen & Moan, 2004). Among them, four were turned to collisions between two bodies. Therefore, position-keeping analysis between bodies is one of the most significant issues for tandem operations.

Tahar and Kim (2003) performed a hull-mooring-riser coupled analysis in the time domain. Ryu and Kim (2005) added the dynamic positioning system application to Tahar and Kim's (2003) work. Ryu and Kim (2005) evaluated the effect of thruster-assisted system employment to the positioning performance of the FPSO and SPAR. The4y performed a coupled analysis of hull, mooring, riser, and thrusters. The discrete Kalman filter and PD controller based on LQR theory were implemented in the DPS. They found that thruster employment enhanced the positioning-keeping performance of the FPSO and spar.

Y.-B. Kim (2004) expanded Tahar and Kim's (2003) work to address the multiple floating body problem. He analyzed the two floating body models on the spar, FPSO, and shuttle tanker. He proposed the combined matrix method (CMM) for the hydrodynamic coefficient and motion matrix for multiple floating body coupled analyses. Kim's method to solve the full, combined matrixes includes mass, interaction, and hawser effect of the first and second body.

KOO and KIM (2005) proposed the separated matrix method (SMM) for reducing the calculation burden for the multiple-body calculation by excluding the off-diagonal term of the hydrodynamic interaction and mechanical coupling effects. They found that the SMM was well matched with Kim's (2004) combined matrix method in the tandem offloading simulation because the tandem offloading simulation had sufficient distance to reduce the interaction effect between the two bodies. Because of this, and also because calculations are lighter under the SMM than the CMM, the SMM will be employed in the tandem offloading simulation in this chapter.

A few studies also address multiple hulls, moorings, risers, and DP-coupled simulations. The tandem offloading simulation with dynamic positioning system will be simulated and analyzed in this chapter.

5.3 Aims

The aim of this chapter is to analyze the global motion change under the DP application conditions under tandem operation conditions for the FPSO and shuttle tanker. The simulation results could yield a practical guide for DP application under tandem operation conditions.

5.4 Mathematical Modeling

5.4.1 Hydrodynamic Coefficient Estimation for Multiple Bodies

The hydrodynamic coefficient, wave exciting force, and moment of floating platform can be obtained via the 3D diffraction theory. The total velocity potential is composed of incident wave potential, diffraction potential, and radiation potential. Total velocity potential should satisfy the Laplace equation, the Bottom boundary condition, the free surface boundary condition, and the Sommerfield radiation boundary condition (KOO & KIM, 2005). The diffraction problem of two bodies can be presented as follows:

$$\begin{aligned} &\frac{\partial \phi_j^{\ I}}{\partial n} = n^I{}_j \qquad on\ \ S_I \qquad (j = 1, 2...., 6) \\ &\frac{\partial \phi_j^{\ II}}{\partial n} = n^{II}{}_j \qquad on\ \ S_{II} \qquad (j = 1, 2...., 6) \end{aligned} \tag{5.1}$$

where ϕ_j^I, ϕ_j^{II} denotes the decomposed radiation potential for Bodies I and II. $n_j^{I,II}$ is a unit normal vector for the six degrees of freedom for Bodies I and II, respectively.

$$n^{I,II} = \begin{cases} (n_1, n_2, n_3)^{I,II} & for\ \ j = 1, 2, 3 \\ (n_4, n_5, n_6)^{I,II} = \tilde{r} \times n^{I,II} & for\ \ j = 4, 5, 6 \end{cases} \tag{5.2}$$

where $\tilde{r}$ denotes the relative distance between the origin of Body I and II

The boundary condition and boundary-value problem of two bodies for the interaction problem can be described in the form of the radiation and scatter potential as in Equation 5.3 (Y.-B. Kim, 2004):

Interaction – radiation/scatter from I near II

$$\begin{aligned} \frac{\partial \hat{\phi}_j^{I}}{\partial n} &= -\frac{\partial \phi_j^{I}}{\partial n} \qquad on\ S_I \qquad (j=1,2,....7) \\ \frac{\partial \hat{\phi}_j^{I}}{\partial n} &= 0 \qquad on\ S_{II} \qquad (j=1,2,....7) \end{aligned} \tag{5.3}$$

Interaction – radiation/scatter from Body II near Body I:

$$\begin{aligned} \frac{\partial \hat{\phi}_j^{II}}{\partial n} &= -\frac{\partial \phi_j^{II}}{\partial n} \qquad on\ S_{II} \qquad (j=1,2,....7) \\ \frac{\partial \hat{\phi}_j^{II}}{\partial n} &= 0 \qquad on\ S_I \qquad (j=1,2,....7) \end{aligned} \tag{5.3}$$

where, $\hat{\phi}_j^{I,II}$ denotes the interaction potential from Bodies I and II. The potential when j=7 means the diffraction.

The hydrodynamic coefficients of this study, such as added mass, mean, and difference frequency force, and radiation damping, were calculated from the 3-D diffraction/radiation frequency domain analysis program.

The Volterra series was employed to convert the hydrodynamic coefficient from frequency domain to time domain. In addition, frequency-dependent radiation damping is calculated in the convolution integral.

The equation of motion of two bodies can be expressed in the following matrix:

$$\begin{bmatrix} M_1 + m_{1,1}^a(\infty) + \int R_{1,1}(t-\tau)d\tau + K_{1,1} & m_{1,2}^a(\infty) + \int R_{1,2}(t-\tau)d\tau + K_{1,2} \\ m_{2,1}^a(\infty) + \int R_{2,1}(t-\tau)d\tau + K_{2,1} & M_2 + m_{2,2}^a(\infty) + \int R_{2,2}(t-\tau)d\tau + K_{2,2} \end{bmatrix} \begin{bmatrix} \ddot{x}_1 \\ \ddot{x}_2 \end{bmatrix} = \begin{bmatrix} \ddot{F}_1 \\ \ddot{F}_2 \end{bmatrix} \tag{5.4}$$

where, *M* is the 6x6 structure mass matrix, *m* is the added mass matrix at infinite frequency, *R* is the retardation function matrix, K is the hydrostatic restoring coefficient matrix, x is the motion vector, and F is the external force vector. The subscript represents the body number. Wave exciting force, wind force, current force, and wave drift force are included in the external force vector. Second-order wave exciting forces are calculated using the Newman approximation, which can be applied to systems with a very small natural frequency of the system and the marginal amount of the QTF near-diagonal term. According to Y.-B. Kim (2004), the Newman approximation method gives acceptable result compared to exact QTF calculation methods. Therefore, the Newman approximation was used for the second-order wave exciting force in this study.

5.4.2 Mechanical Coupling between Two Floating Bodies and Slender Members

The mooring and riser were assumed as the rod, which had no torque or applied external twisting moment. Using the slender finite element formulation, the linear momentum conservation can find a position vector of slender body: $\vec{r}(s,t)$

where, s is arc length and *t* is time.

$$
\begin{aligned}
&-\left(B\vec{r}\,''\right)''+\left(\lambda\vec{r}\,'\right)'+\vec{q}=m\ddot{\vec{r}}\\
&\lambda=T-Bx^2\\
&T=T_0+P_eA_e-P_iA_i
\end{aligned}
\tag{5.5}
$$

where, *prime* $(\ )'$ and *dot* $\dot{r}$ present spatial and time derivative, *B* is bending, *T* is the local effective tension, *x* is the local curvature, *m* is the mass per unit lenth, $\vec{q}$ is the distributed force on the rod per unit length, T_0 is the local tension, P_e is the external pressure, P_i is the internal pressure, A_e and A_i are external and internal cross-sectional area, respectively. The scalar λ is a Lagrange multiplier.

Using the Galerkins method and integration by parts, equation () can be simplified as in Equation (5.6) (Garrett, 1982).

$$\begin{aligned}&\int_0^L r\left[B\vec{r}\,''A_i''+\lambda\vec{r}\,'A_i'-\vec{q}A_i'+m\ddot{\vec{r}}A_i\right]ds\\&=B\vec{r}\,''A_i'\Big|_0^L+\lambda\vec{r}\,'-\left(B\vec{r}\,''\right)'A_i\Big|_0^L\end{aligned}\tag{5.6}$$

According to KOO and KIM (2005), the transmitted force from moorings and risers can be presented as :

$$F_p=K(Tu_p-u_I)+C\left(T\dot{u}_p-\dot{u}_I\right)\tag{5.7}$$

where ***K*** is the stiffness matrix, ***C*** is the damping matrix, ***T*** is the transformation matrix between the platform origin and confection, u_p *and* u_I are displacement vectors of the platform and connection point.

Finally, the equation of motion of two bodies can be defined as follows:

$$\left(M + M_a(\infty)\right)\ddot{u}_p + \int_0^\infty R(t-\tau)\dot{u}_p d\tau + K_H u_p = F_D + F^{(1)} + F^{(2)} + F_P \tag{5.8}$$

where, M, M_a are the structure mass and added mass, R is the retardation function, K_H is the hydrostatic restoring matrix, F_D is the drag force acting on the hull, $F^{(1)}$ and $F^{(2)}$ are the first- and the second-order wave force, and F_p is the transmitted force from mooring and riser.

For the assembling global matrix of two bodies, the Separated Matrix Method (SMM) (KOO & KIM, 2005) was employed. The benefit of SMM is its light calculation burden, although this method gives well-matched results compared to full-coupled global matrix formulation. In the SMM, the global matrix is separated by each body. In mechanical coupling between two bodies, the mechanical coupling is considered by the static tension force from hawser. The hawser is generally exposed in the air, so its inertia and drag are marginal compared to those of mooring and risers. Figure 5.1 presents the concept diagram of the SMM.

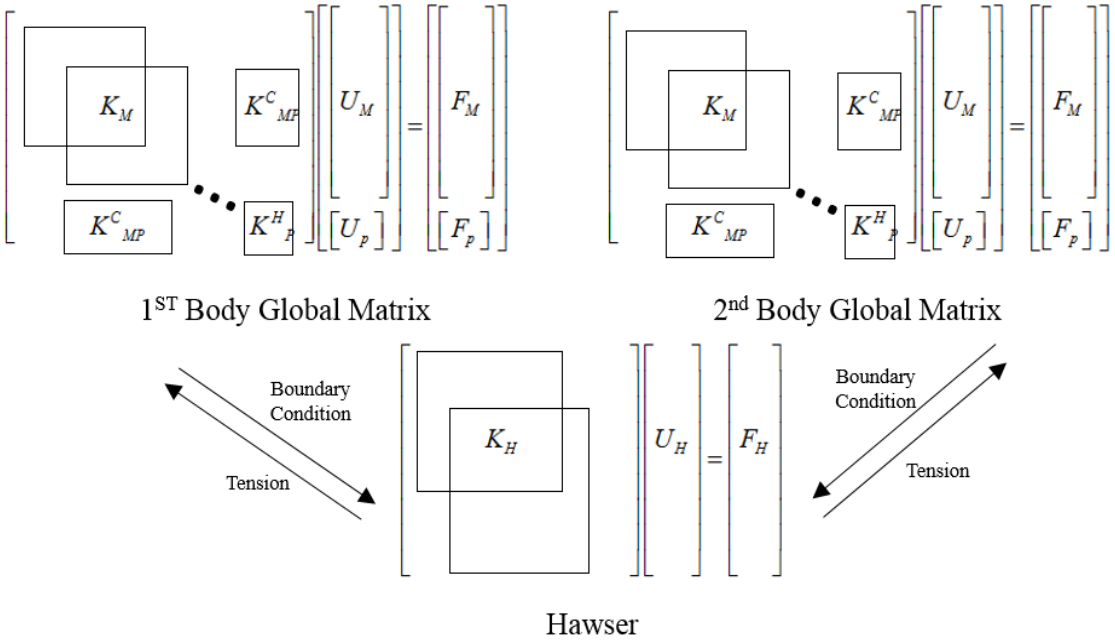

Figure 5.1 Separate Matrix Method (Koo & Kim, 2005)

where,

K_M : *The coeffcient of hull*

K_H : *The coefficient of hawser*

K_P : The *coeffcient of mooring and riser*

K_{MP}^C : *The coupled coefficient of hull, mooring, and riser*

U_M : *The dispacement vector of hull*

U_H : *The dispacement vector of hawser*

U_P : *The dispacement vector and riser*

F_M : *The force vector of hull*

F_H : *The force vector of hawser*

F_P : *The force vector and riser*

5.4.3 Shuttle Tanker Particulars

Table 5.1 Principal Dimensions of the Simulation Vessel

Designation	Symbol	Unit	Quantity
Length b/w perpendiculars	Lpp	m	310
Breadth	B	m	47.17
Draft	T	m	18.9
Length to beam ratio	L/B		6.57
Beam to draft ratio	B/T		2.5
Displacement	∆	ton	240869
Block coefficient	Cb		0.85
Center of buoyancy forward section 10	FB	m	6.6
Water plane area	A	m^2	13400
Water plane coefficient	Cw		0.9164
Center of water plane area forward section 10	FA	m	1.0
Trans. radius of gyration in air	Kxx	m	15.79
Long. radius of gyration in air	Kyy	m	115.03
Yaw radius of gyration	Kzz	m	116.13
Wind area front	Af	m^2	1012
Wind area side	Ab	m^2	3772

Table 5.2 Mooring Line Particulars

Designation	Unit	Quantity
Water depth	*m*	1829
Pre-tension	*kN*	1424
Number of lines		4×3
Degree between the 3 lines	*deg.*	5
Length of mooring line	*m*	2652
Radius of location of chain stoppers on turn table	*m*	7.0
Segment 1: Chain		
Length at anchor point	*m*	121.9
Diameter	*cm*	9.52
Dry weight	*N/m*	1856
Weight in water	*N/m*	1615
Stiffness AE	*kN*	912120
Segment 2: Polyester		
Length	*m*	2438
Diameter	*cm*	16.0
Dry weight	*N/m*	168.7
Weight in water	*N/m*	44.1
Stiffness AE	*kN*	186800
Segment 3: Chain		
Length at anchor point	*m*	91.4
Diameter	*cm*	9.53
Dry weight	*N/m*	1856
Weight in water	*N/m*	1615
Stiffness AE	*kN*	912120

Table 5.3 Riser and Hawser Particulars

	Pre Tension	Length	Dry Weight	Wet Weight	AE
	kN	*M*	*N/m*	*N/m*	*Kn/m*
Riser	1.1×10^5	N/A	2560	1310	1.69×10^8
Hawser	8.0×10^5	N/A	2890	N/A	1.87×10^6

FPSO, with four mooring lines and one riser, and is identical to that used by Koo and Kim ((KOO and KIM (2005)).

5.4.4 DP Controller for Shuttle Tanker

The system equation of DP shuttle tanker is as follows:

$$\begin{aligned}\dot{\mathbf{x}} &= \mathbf{Ax} + \mathbf{Bu}\\ \mathbf{y} &= \mathbf{Cx} + \mathbf{v}\end{aligned} \tag{5.9}$$

where, dot (·) denotes time derivative, and each vector written in lower case can be described by the following set of definitions:

State $\mathbf{x} = [u, x, v, y, \omega, \psi]^T$ Control Input $u = \left[\tau_x, \tau_y, \tau_\phi\right]^T$ Measurement $\mathbf{y} = [x, y, \psi]^T$

Measurement-Noise $\mathbf{v} = [v_x, v_y, v_\psi]^T$

where, $\mathbf{A} = \mathbf{M}^{-1}\begin{bmatrix}0&0&0&0&0&0\\1&0&0&0&0&0\\0&0&0&0&0&0\\0&0&1&0&0&0\\0&0&0&0&0&0\\0&0&0&0&1&0\end{bmatrix}$ $\mathbf{B} = \mathbf{E} = \mathbf{M}^{-1}\begin{bmatrix}1&0&0\\0&0&0\\0&1&0\\0&0&0\\0&0&1\\0&0&0\end{bmatrix}$ $\mathbf{C} = \begin{bmatrix}0&1&0&0&0&0\\0&0&0&1&0&0\\0&0&0&0&0&1\end{bmatrix}$

where,

$M_{11} = m + a_{11}(0), M_{22} = m + a_{22}(0), M_{26} = m + a_{26}(0), M_{62} = m + a_{62}(0), M_{66} = I + a_{66}(0)$,

and m the mass of the floating structure, I is the moment of inertia in z-direction, and $a_{ij}(0)$ added masses in low frequency, and $\hat{x}$ is the state estimation vector.

For calculating PID gains, the linear quadratic regulator (LQR) theory was applied. The LQR is conventionally used for finding optimal control gain matrix K that can minimize state error and thruster usage together in the following equation(Ryu, 2005):

$$J = \int_0^\infty \left\{ \mathbf{e}(t)^T \mathbf{Q}_o \mathbf{e}(t) + \mathbf{u}(t)^T \mathbf{R}_o \mathbf{u}(t) \right\} dt \tag{5.10}$$

5.4.5 Hawser Modeling

The hawser for connecting the two bodies was modeled as a linear spring. For implementation purposes, the linear spring constant was considered a restoring coefficient in the surge direction inside the time domain simulation code. The initial length of the hawser is 30m, and is measured and updated at every time step. The hawser connects each body with and 1/10 of the mooring pre-tension. The mechanical coupling was solved through the hawser matrix.

5.4.6 Tandem Offloading Configuration

Figure 5.2 shows a bird-eye view of the tandem configuration of the moored FPSO and DP shuttle tanker.

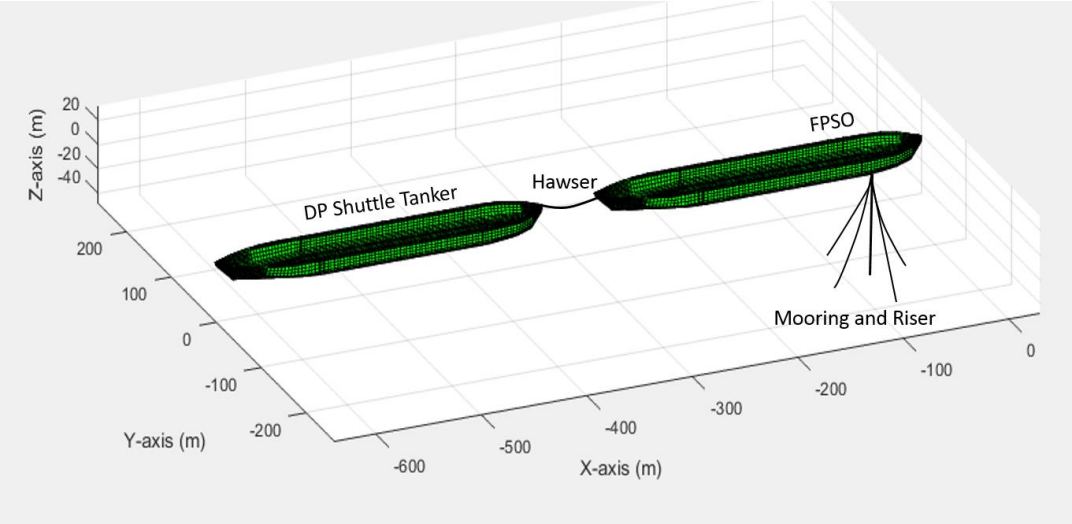

Figure 5.2 FPSO – Shuttle Tanker Configuration

Figure 5.3 presents the bottom view of the tandem configuration of the moored FPSO and the DP shuttle tanker. Six azimuth thrusters were installed in the DP shuttle tanker simulation model. The moored FPSO has an internal bow turret mooring.

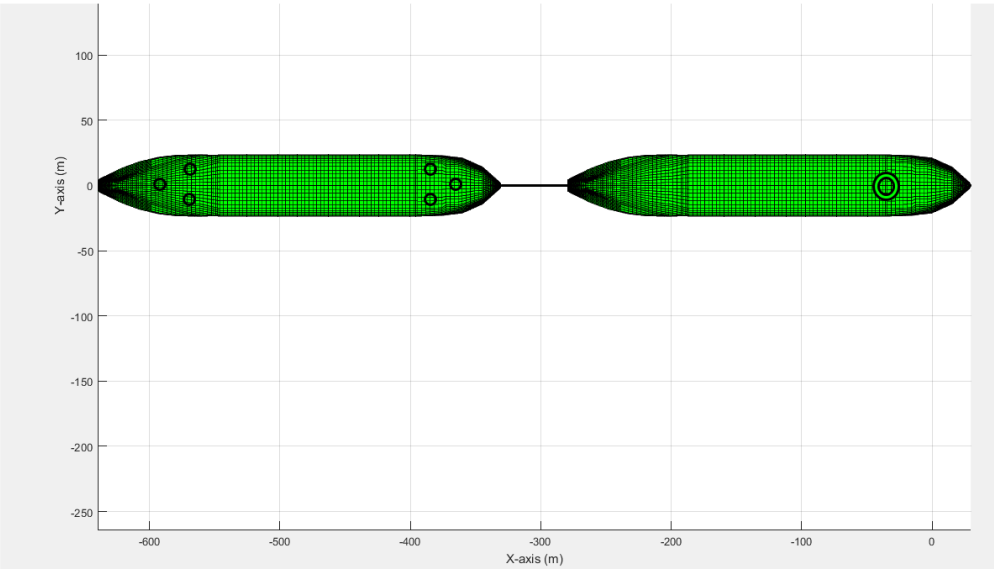

Figure 5.3 Bottom View of Tandem Configuration

Thruster constraints and particulars are presented below.

Table 5.4 Thruster Information

Thruster Maximum Capacity	300KN
Thruster Maximum Change Rate	60 KN /sec
Thruster Angle Change Rate	10deg / sec
Thruster Position (A.P=0, C.L=0)	T1(290m,0m), T2(275 m,-15m), T3(275m,15m) T4(35m,-15m) T5(35m,15m) T6(20m,0m)

5.5 Simulation Conditions

5.5.1 Environmental Conditions

Two environmental cases are simulated in this chapter. The first is under mild, noncollinear West Africa conditions, which are the general target operation conditions for tandem application. The second is under Gulf of Mexico one-year, noncollinear conditions, which are simulated to assess the possibility of tandem offloading operations with a DP shuttle tanker.

Table 5.5 Environmental Conditions

		West Africa	GOM 1-Year Storm
WAVE (Direction: 180 DEG)	Significant Wave Height H_s	2.7m	4.3m
	Peak Period T_p	16.50sec	9sec
	Overshoot Parameter γ	6	2
WIND (Direction: 210 DEG)		5 m/sec at 10m	14.3m/sec at 10m
CURRENT (Direction: 150 DEG)		0.15m/sec	0.33m/sec

5.6 Simulation Results

5.6.1 West African Conditions

Figure 5.4 represents the FPSO surge-sway trajectory for the shuttle tanker with DPS, and without DP. The blue circle is the FPSO trajectory. The red dotted line represents the horizontal trajectory when DPS was applied to the shuttle tanker. The typical fish-tailing motion was seen in the simulation without DP. The movement in sway direction of the shuttle tanker without DPS is 8.5m, which is reduced when DPS is implemented in the shuttle tanker. The DPS application deviates the sway position from 7.5m to 2m. The sway

motion of the shuttle tanker with DPS also was not biased, and fluctuated from -1m in sway to 1m.

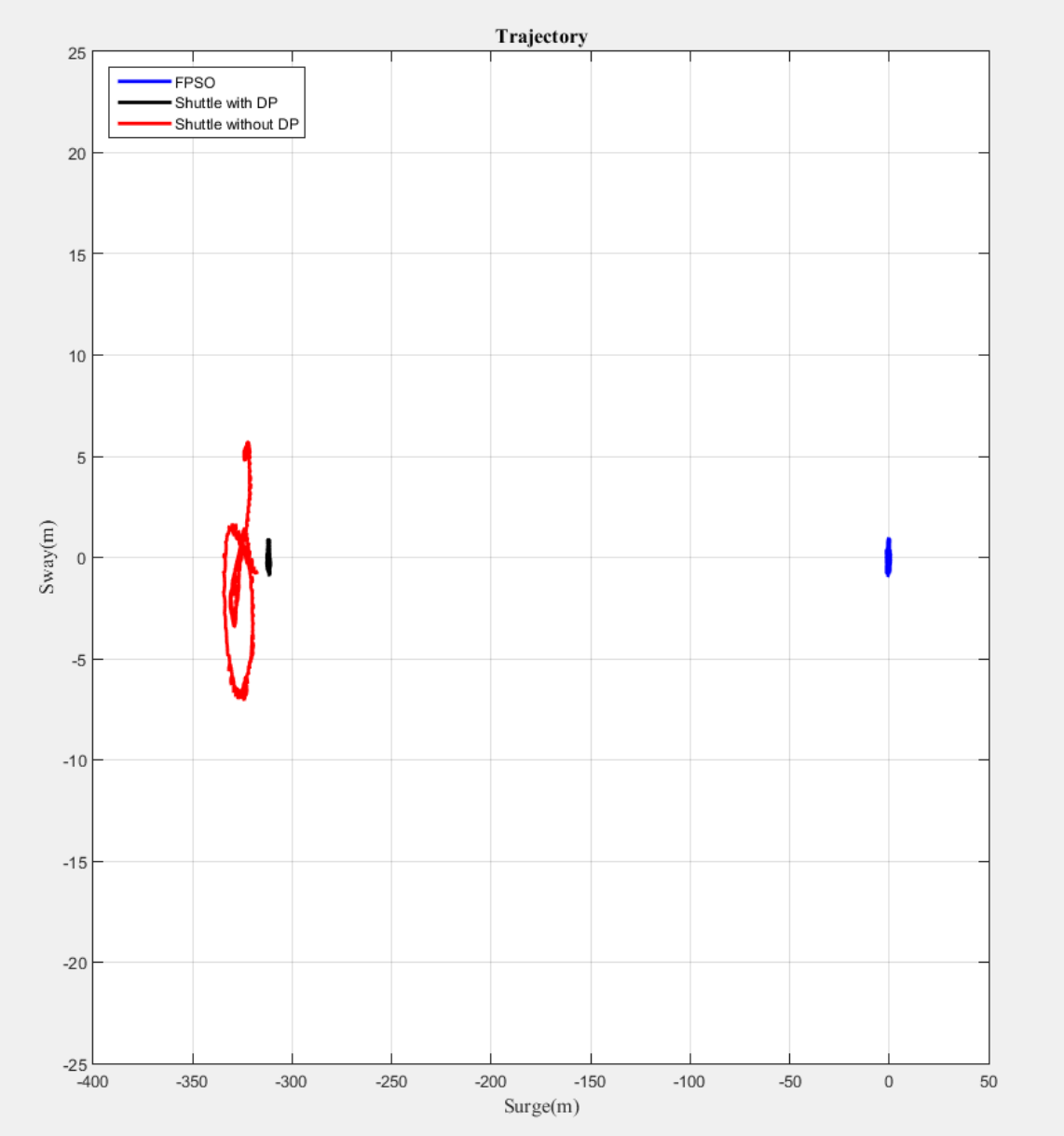

Figure 5.4 Trajectory of the Shuttle Tanker and FPSO in West African Conditions

Figure 5.5 presents the time histories of the 6DOF motion. The black line illustrates the shuttle tanker equipped DPS, and the red-dotted line without DP. The vertical motions

of the shuttle tanker with DPS and without DPS are almost similar. According to the position deviation history, the DPS application apparently enhanced the position-keeping performance.

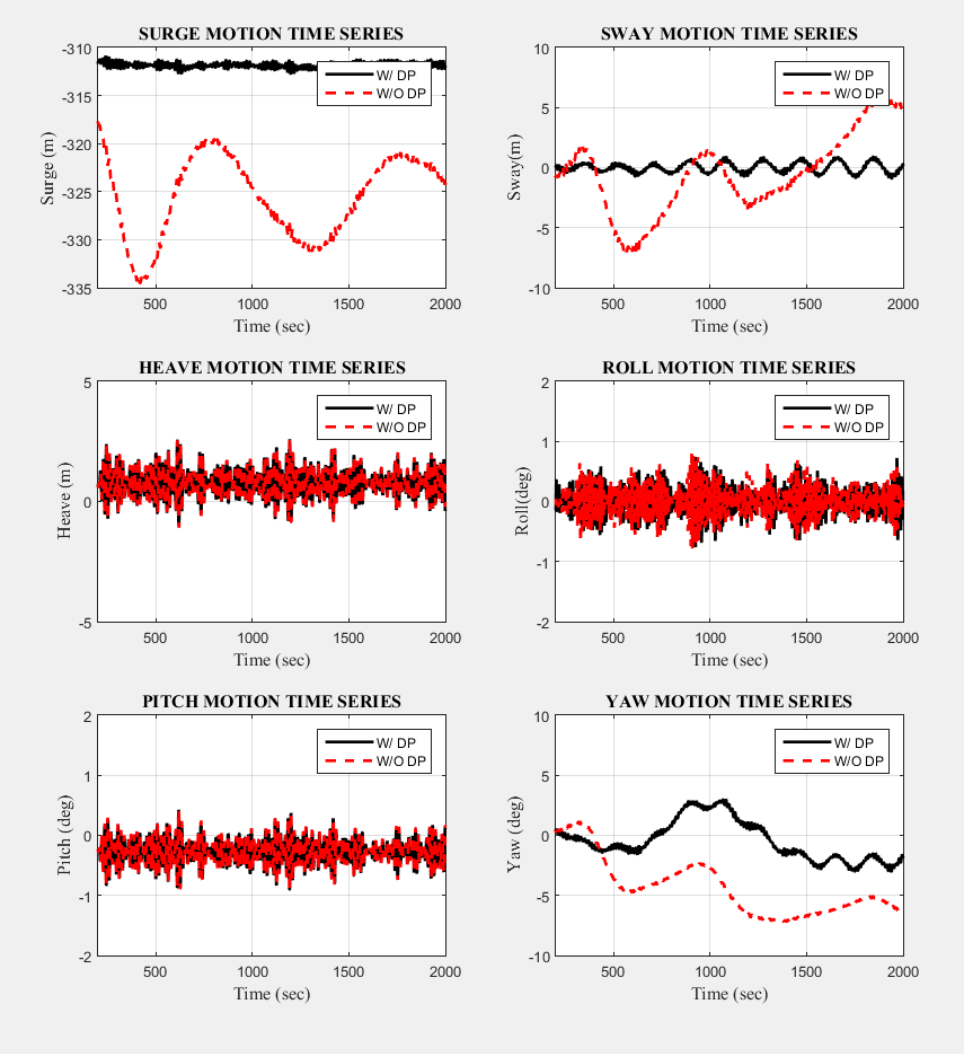

Figure 5.5 Motion Time History in West African Conditions

Figure 5.6 presents the spectra of the 6DOF motion. The surge and sway motion spectra with the DPS application is significantly smaller than that of the shuttle tanker

without DPS. Based on these results, DPS appears to be a promising solution for attenuating horizontal excursion due to fish-tailing motion.

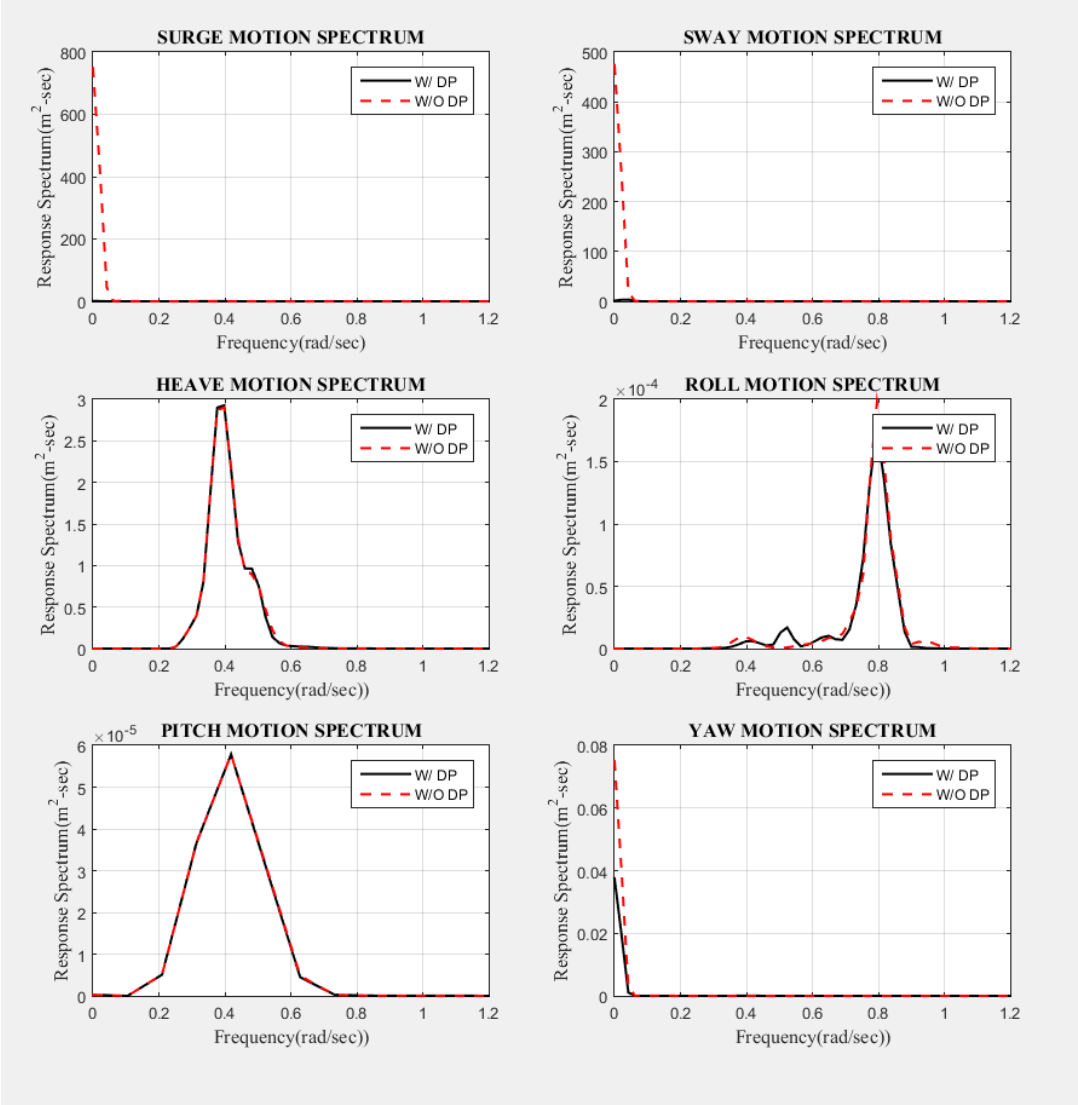

Figure 5.6 Motion Spectra in West African Conditions

5.6.2 Gulf of Mexico One-Year Conditions

Figure 5.7 illustrates the trajectory of the shuttle tanker and FPSO in GOM one-year conditions. The GOM one-year storm conditions are harsher than West African conditions. Generally, tandem offloading is impossible during these conditions without DPS because the position excursion exceeds the limitations of hawser-possible elongation length. Figure 5.7 depicts this phenomenon. The trajectories of the FPSO, and the shuttle tankers with and without DPS, are the blue, black, and red lines, respectively. The hawser maximum breaking elongation is 150m. The shuttle tanker without DPS drifted in the sway direction more than 150m. This results shows that it is impossible under GOM 1-yr storm condition without DPS. For the GOM 1-yr case, two control gains were employed. Those are high gain and moderate gain for controller to evaluate its performance. High gain requires sufficient thruster capacity. Figure 5.8 presents the comparison when hired the moderate and high gain for shuttle tanker. It shows excellent position keeping performance with high gain meanwhile, there is position excursion when the moderate gain was considered but it is still operable.

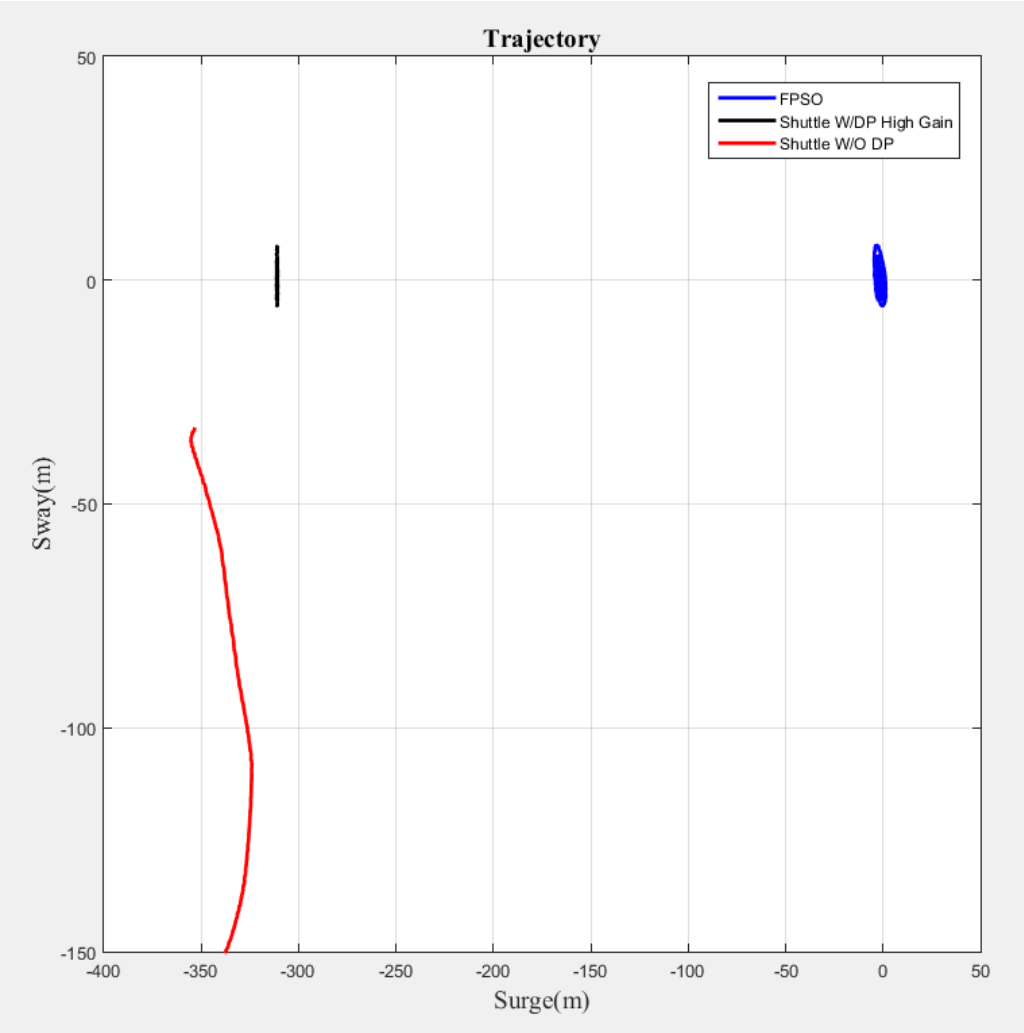

Figure 5.7 Trajectory of the Shuttle Tanker and FPSO in Gulf of Mexico One-Year Conditions

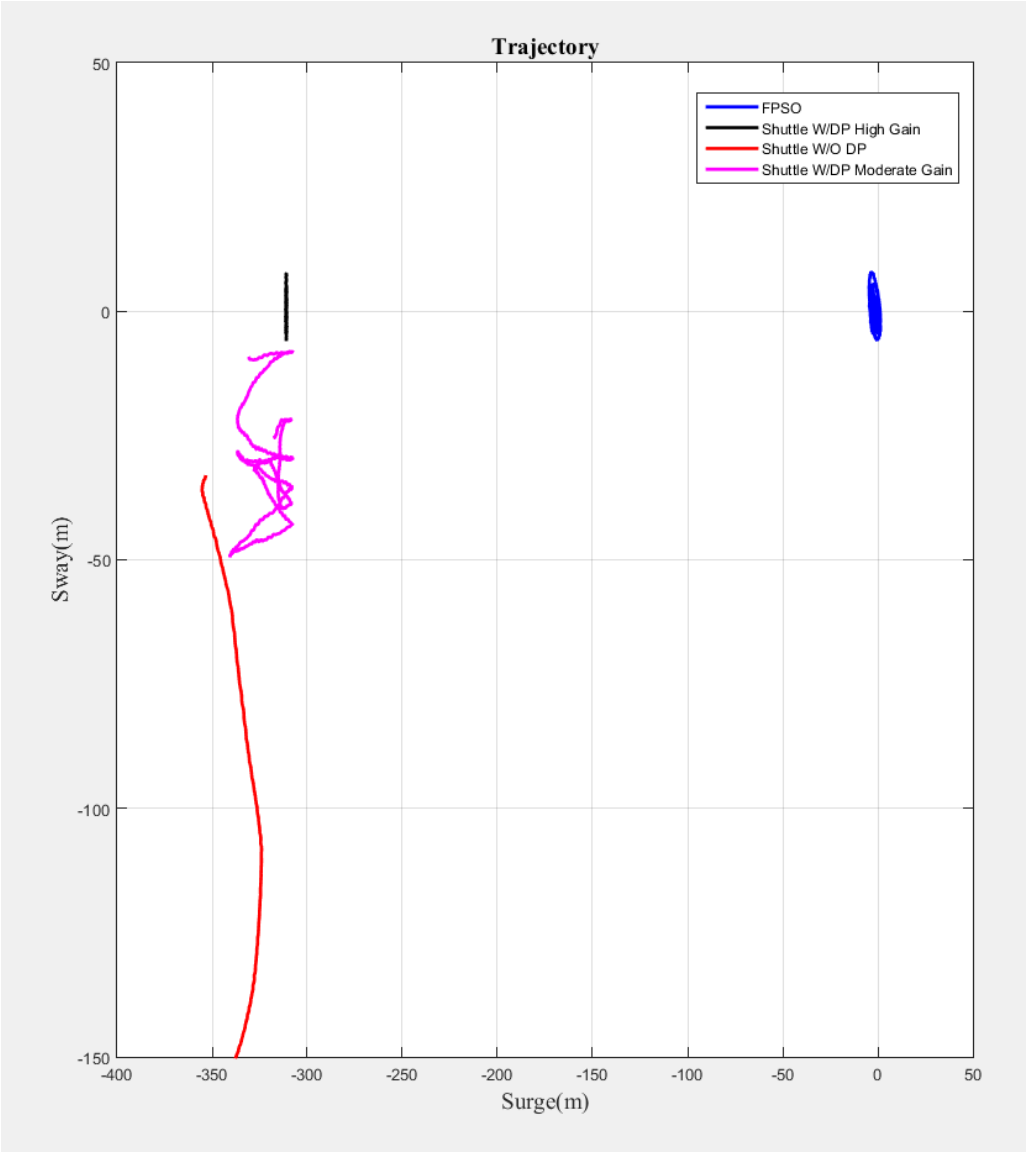

Figure 5.8 Comparison of Trajectories of the Shuttle Tanker and FPSO in Gulf of Mexico One-Year Conditions with DP Moderate Gain Hired

Figure 5.9 presents the 6DOF motion time series according to the DP application. The horizontal motions of the shuttle tanker with DP were well controlled compared to the shuttle tanker without DP. The yaw angle of the shuttle tanker fluctuated between 5 degrees to -5 degrees. This phenomenon resulted from the interaction between the FPSO. The sway motion of the shuttle tanker without DPS drifted away. The surge motion of the shuttle tanker fluctuated between -350m to -330m. It is highly probable that a collision between the shuttle tanker and FPSO would result with DP.

Figure 5.10 illustrates the 6DOF motion spectra of the shuttle tanker with DPS and without DP. The surge, sway, and yaw motion spectra with the DP application were significantly lower than without. In addition, as environment conditions grew, even the vertical motion of the shuttle tanker with DPS was reduced compared to the shuttle tanker without DPS. The reason for this phenomenon is that the horizontal motion amplitudes were significantly reduced and its coupling effect to the vertical motion also was reduced.

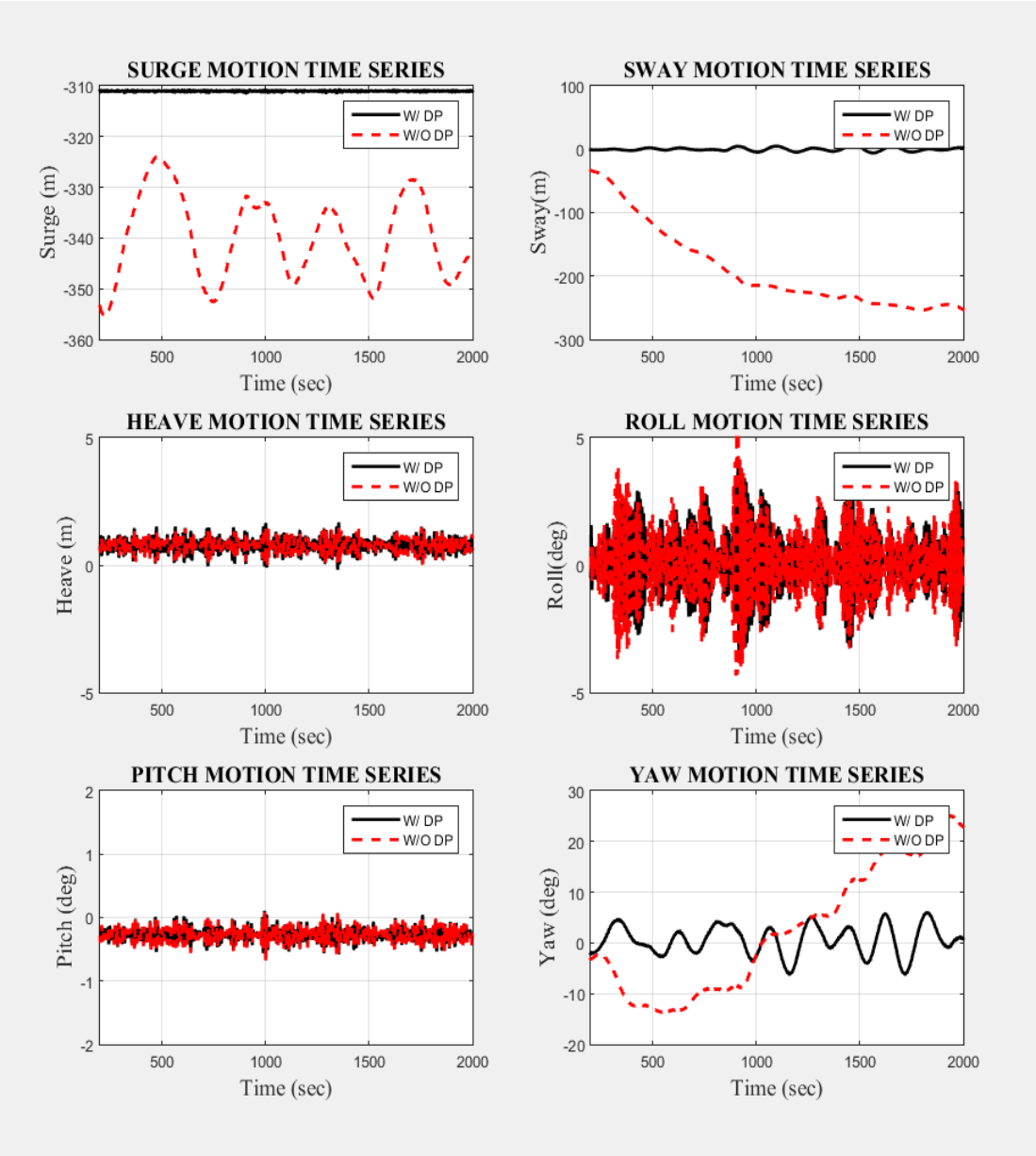

Figure 5.9 6DOF Motion Time History in Gulf of Mexico One-Year Conditions

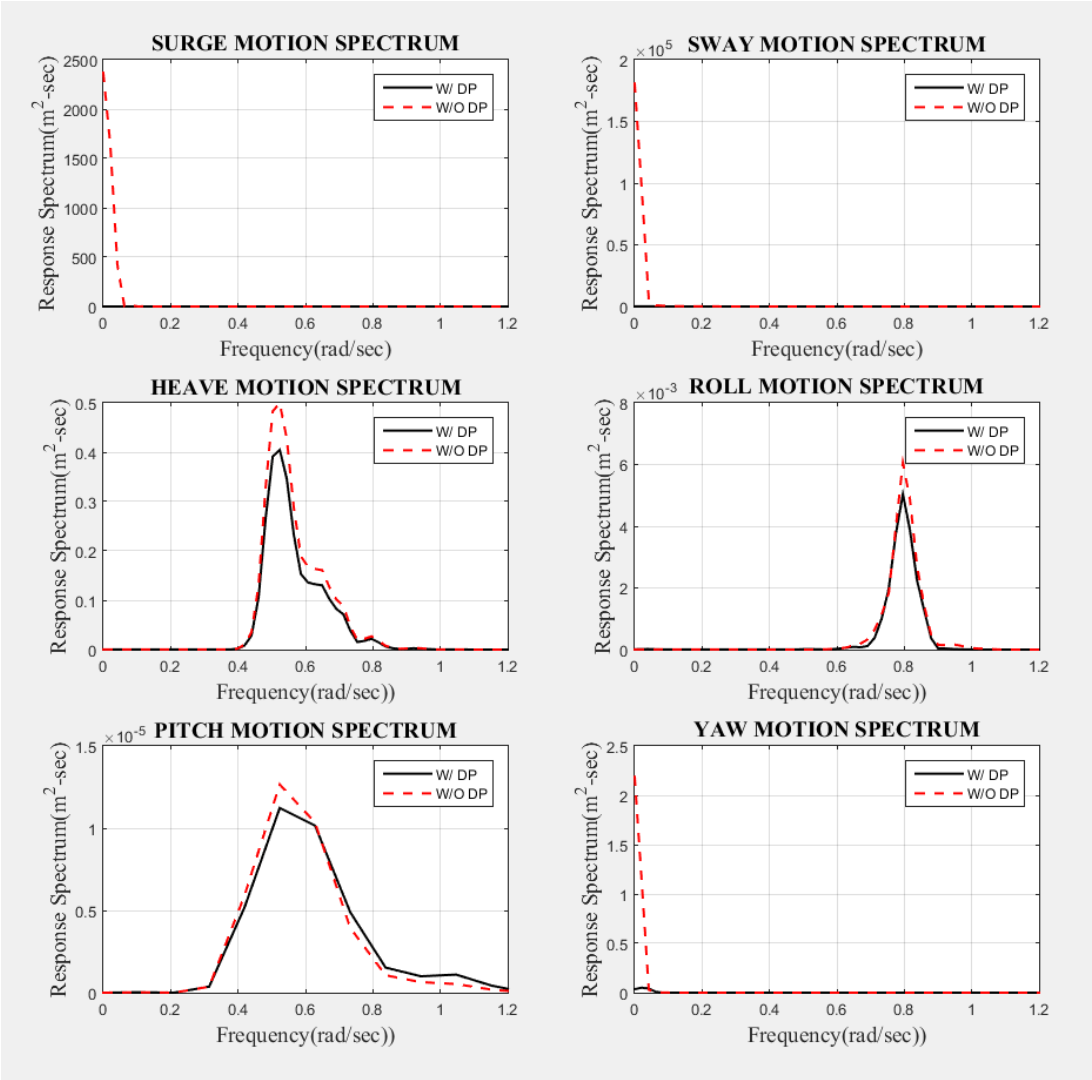

Figure 5.10 Motion Spectra in Gulf of Mexico One-Year Conditions

5.7 Conclusion

The DPS application effect on the shuttle tanker was analyzed in the multi-body tandem offloading simulation. The hydrodynamic coefficients and the interaction effect were obtained by the SMM. The West African and GOM one-year storm conditions were simulated. The FPSO was moored by the internal bow turret and DPS was installed in the shuttle tanker. The FPSO and shuttle tanker were connected by flexible hawser. The shuttle tanker DPS was designed to keep a specified distance from the FPSO and to control surge, sway, and yaw motion. The sway motion of the shuttle tanker with DPS was reduced, compared to the one without, from 8.5m to 3m under West African conditions. The DPS position-keeping performance enhancement was apparently powerful under these harsh environmental conditions in tandem configuration. The sway excursion without DPS is over the limitation of the hawser maximum elongation length which means it is impossible to operate. However, the DP with high gain and moderate gain condition made shuttle tanker could be operated under GOM one-year storm condition.

CHAPTER VI

CONCLUSION

The eco-friendly dynamic positioning control algorithm that minimizes both fuel consumption and gas emissions was developed based on the penalty method optimization theory. Six degrees of freedom, hull-mooring-riser-thrusters, coupled time domain simulations were employed to compare this with conventional optimization methods, such as the pseudo-inverse method, quadratic programming, and genetic algorithm. The penalty method-based dynamic positioning algorithm indicated improved fuel consumption efficiency and CO_2 emission performance in both Gulf of Mexico one-year and 100-year storm conditions, compared to the conventional optimization methods.

Feed-forward control was used to enhance position-keeping performance, mooring top tension due to surge slow varying motion, fuel consumption, and CO_2 emissions. Second-wave order force, which is a target load component for the dynamic positioning system, was directly integrated and first applied to feed-forward control that was designed to reduce fuel consumption and gas pollution. Feed-forward control improved fuel consumption, gas emissions, and positioning performance when compared to a simulation that used feedback control only. The enhancement of feed-forward control was proportional to the intensity of environmental conditions.

Differences in global motion were found as a result of turret location. Bow and mid-ship internal turret designs were investigated with a dynamic positioning system. A bow internal turret design is a general concept of the FPSO mooring system because a bow

turret permits free rotation by the weathervaning mechanism, which naturally minimizes environmental loads. The mid-ship turret design reduces vertical motion under harsh environmental conditions, but it cannot control heading naturally. Hull-mooring-riser-thruster, fully coupled simulations were conducted for the bow and mid-ship turret design were demonstrated in time domain simulation under both Gulf of Mexico one-year and 100-year storm conditions. The results showed that the dynamic positioning heading control enhanced the mid-ship turret design position-keeping performance. Furthermore, the mid-ship turret design makes controlling the position of FPSO without dynamic positioning system very difficult.

The developed dynamic positioning system was applied to reduce excessive horizontal motion due to the fish-tailing motion of shuttle tankers at FPSO-shuttle tanker tandem off-loading configuration. A single-matrix method was adopted to analyze hydrodynamic coefficients of multiple bodies. Multi-body coupled simulations were conducted under West African and Gulf of Mexico one-year storm conditions. The simulation found that the dynamic positioning application for shuttle tankers in the tandem position expands its operational environment limit.

REFERENCES

Aalbers, A., Tap, R., & Pinkster, J. (2001). An application of dynamic positioning control using wave feed forward. *International Journal of Robust and Nonlinear Control, 11*(13), 1207-1237.

Balchen, J. G., Jenssen, N. A., Mathisen, E., & Sælid, S. (1980). A dynamic positioning system based on Kalman filtering and optimal control. *Modeling, Identification and Control, 1*(3), 135-163

Chen, H., & Moan, T. (2004). Probabilistic modeling and evaluation of collision between shuttle tanker and FPSO in tandem offloading. *Reliability Engineering & System Safety, 84*(2), 169-186.

De Wit, C. (2009). *Optimal thrust allocation methods for dynamic positioning of ships.* Delft University of Technology.

Duggal, A. S., Heyl, C. N., & Vance, G. P. (2000). *Global Analysis of the Terra Nova FPSO Turret Mooring System.* Paper presented at the Offshore Technology Conference.

Finucane, M. (2012). Details of Gryphon Incident - Lessons Learned *Aberdeen International Organization Safety and Healith Conference*.

Garrett, D. (1982). Dynamic analysis of slender rods. *Journal of Energy Resources Technology, 104*(4), 302-306.

Isherwood, R. (1973). Wind resistance of merchant ships. *RINA Supplementary Papers, 115*.

Jayaram, V. (2010). Analytical Framework to Evaluate Emission Control Systems for Marine Engines. *University of California Riverside PhD Dissertation.*

Johansen, T. A., & Fossen, T. I. (2013). Control allocation—a survey. *Automatica, 49*(5), 1087-1103.

Johansen, T. A., Fossen, T. I., & Berge, S. P. (2004). Constrained nonlinear control allocation with singularity avoidance using sequential quadratic programming. *IEEE transactions on control systems technology, 12*(1), 211-216.

Kang, H., & Kim, M. (2014). Safety assessment of caisson transport on a floating dock by frequency-and time-domain calculations. *Ocean Systems Engineering, 4*(2), 99-115.

Kannah, T. R., & Natarajan, R. (2006). Effect of turret location on the dynamic behaviour of an internal turret moored FPSO system. *Journal of Naval Architecture and Marine Engineering, 3*(1), 23-37.

Kim, C.-h., Kim, Y.-s., Jung, H.-W., Ryu, S.-n., & Yoon, K.-k. (2012). Electric power system design and analysis for drilling rigs. *Journal of the Korean Society of Marine Engineering, 36*(7), 942-947.

Kim, M., Koo, B., Mercier, R., & Ward, E. (2005). Vessel/mooring/riser coupled dynamic analysis of a turret-moored FPSO compared with OTRC experiment. *Ocean Engineering, 32*(14), 1780-1802.

Kim, Y.-B. (2004). *Dynamic analysis of multiple-body floating platforms coupled with mooring lines and risers.* Texas A&M University.

Koo, B.-J., & KIM, M.-H. (2005). Motion Analysis of Two Floating Platforms with Mooring and Hawser Lines in Tandem Moored Operation by Combined Matrix Method and Separated Matrix Method. *Journal of Ocean Engineering and Technology, 19*(5), 1-15.

OCIMF. (1996). Prediction of wind loads and current loads on VLCCs. *Oil Companies International Marine Forum*

Pinkster, J. (1978). *Wave feed-forward as a means to improve dynamic positioning.* Paper presented at the Offshore Technology Conference.

Pinkster, J. (1981). *Mean and low frequency wave forces on semi-submersibles.* Paper presented at the Offshore Technology Conference.

Quadvlieg, F., Hallmann, R., Hughes, G., & Harris, R. (2011). *Improved Dynamic Positioning Using Wave Feed Forward.* Paper presented at the ASME 2011 30th International Conference on Ocean, Offshore and Arctic Engineering.

Ran, Z., & Kim, M. (1997). Nonlinear coupled responses of a tethered spar platform in waves. *International Journal of Offshore and Polar Engineering, 7*(02).

Rao, S. S., & Rao, S. (2009). *Engineering optimization: theory and practice*: John Wiley & Sons.

Rindarøy, M., & Johansen, T. A. (2013). Fuel optimal thrust allocation in dynamic positioning. *IFAC Proceedings Volumes, 46*(33), 43-48.

Ryu, S. (2005). *Hull/Mooring/Riser coupled motion simulations of thruster-assisted moored platforms.* Texas A&M University.

Ryu, S., & Kim, M.-H. (2005). *Hull/Mooring/Riser coupled motion simulations of thruster-assisted moored platforms.*

Sincock.P. (1989). *Nonlinear Compliant Systems in Irregular Seas*. University College London.

Sørensen, A. J. (1999). Thruster Assisted Positioning Mooring System for Turret-Anchored FPSO. *IEEE International Conference on Control Application*.

Sørensen, A. J. (2011). A survey of dynamic positioning control systems. *Annual reviews in control, 35*(1), 123-136.

Steven.N. (2007). DP in offshore drilling increase importance *Dynamic Positioning Conference 2007 Key Note Speech*.

Tahar, A., & Kim, M. (2003). Hull/mooring/riser coupled dynamic analysis and sensitivity study of a tanker-based FPSO. *Applied Ocean Research, 25*(6), 367-382.

Thiagarajan, K., & Finch, S. (1999). An Investigation Into the Effect of Turret Mooring Location on the Vertical Motions of an FPSO Vessel. *Journal of Offshore Mechanics and Arctic Engineering, 121*(2), 71-76.

Waals, O. J., Aalbers, A., & Pinkster, J. (2002). *Maximum likelihood method as a means to estimate the directional wave spectrum and the mean wave drift force on a dynamically positioned vessel.* Paper presented at the ASME 2002 21st International Conference on Offshore Mechanics and Arctic Engineering.

Yang, C. K., & Kim, M. (2011). The structural safety assessment of a tie-down system on a tension leg platform during hurricane events. *Ocean Systems Engineering, 1*(4), 263-283.

You, Y., Choi, J. W., Kim, D. S., & Lee, Y. B. (2014). *A Prediction Method of the Crabbing Capability Using Penalty Method.* Paper presented at the The Twenty-fourth International Ocean and Polar Engineering Conference.

Zhao, L., & Roh, M.-I. (2015). A Thrust Allocation Method for Efficient Dynamic Positioning of a Semisubmersible Drilling Rig Based on the Hybrid Optimization Algorithm. *Mathematical Problems in Engineering, 2015*.